Computer Simulation Studies of Dynamics and Self-Assembly Behaviour of Charged Polymer Systems

Chris Davies

A thesis submitted for the degree of
Doctor of Philosophy

University of Reading

Department of Mathematics
University of Reading
April 2019

Abstract

Understanding charged polymer behaviour is fundamental in advancing our knowledge of biological and synthetic polymers, including associating polymers. We first study single-chain diblock polyampholytes (PA) that are asymmetric in either charge densities of the two blocks, or in block lengths but with equal charge densities on both sides. In the former case, the increase in length requires higher energy to fold the longer block. For strongly associating systems, near symmetric chains are globular, whereas high asymmetric chains adopt bottle brush conformations.

In the latter case, we study chains that have an overall fixed charge fraction but carry a net charge due to the difference in block lengths. At very low asymmetry the conformations of the PA chains follow the dense packing of electrostatic blobs, however increasing the asymmetry leads to a net-charged oblong or a stretched PE core with the opposite block wrapping around in a single helix, depending on charge strength. Above a universal threshold around, wherein the longer block is 1.5 times the length of the shorter block, the conformation transitions into a cigar-like, or PE helix wrapped around an oppositely charged PE core (helix/PE core) head plus a polyelectrolyte tail carrying excess charge.

Secondly, we study the aggregation of asymmetric diblock PA chains each carrying a

net charge, and observe a repulsive behaviour over a wide range of chain lengths, chain asymmetry and charge strengths. Using umbrella sampling we show that symmetric polyampholytes favour association, however even slightly asymmetric chains exhibit repulsion. We study the stability of pre-assembled aggregates consisting of number of chains $N_{poly} = 16$. The aggregates eventually break up due to the electrostatic repulsion. If we introduce a certain amount of polyelectrolyte stabilisers, the aggregates are much more stable.

Furthermore, we study ionomer systems composed of unentangled polyelectrolyte chains with counterions and find the nature of Coulombic interactions leads to the formation of large clusters with complex geometries. For increasing charge strength, we observe a transition from dipoles, to head to tail aggregation, to double network. The dynamics and rheological behaviour of the reversible double network systems are investigated and understood from the microstructures of the systems.

Declaration

I confirm that this is my own work and the use of all material from other sources has been properly and fully acknowledged.

Chris Davies

Acknowledgements

I would like to thank Dr. Zuowei Wang for his invaluable help throughout the entirety of this research. Without his insight and knowledge, none of this would be possible.

I would also like to thank Prof. Ian Hamley, as well as the Reading Theoretical Polymer Physics Group, namely Patrick, Dipesh, Jack K, Jian, Changqiong and Chris W, for their guidance and useful discussions. A special thanks goes out to Pawel, his help with the cluster and computer programming was incredibly important to this research. I would also like to thank Prof. Alexei E. Likhtman, who sadly passed away near the beginning of my research, however his knowledge was widely and personally influential. I'd like to acknowledge personal discussions between Michael Rubinstein and Zuowei Wang as greatly influential on the diblock polyampholyte work.

Finally, I would like to thank my friends and family for their patience and encouragement throughout the years. In particular Yuhan, who has provided much comfort and support, and Jack A for providing a fresh set of eyes.

Contents

List of Figures

xiii

List of Symbols

N	Degree of polymerisation
N_+, N_-	Degree of polymerisation of positively/ negatively charged blocks
N_poly	Number of polymers
N_part	Number of particles
f_+, f_-	Charge fraction
D	Diffusion coefficient
ζ	Friction Cofficient
T	Temperature
k_B	Boltzmann constant
$\mathbf{r}_i$	Position of particle i
$\mathbf{v}_i$	Velocity of particle i
$\mathbf{a}_i$	Acceleration of particle i
r_{ij}	Distance between particles i and j
R_e	Root mean squared end to end distance
R_g	Roor mean squared radius of gyration
$\mathbf{r}_\text{cm}$	Chain centre of mass
$g_{1,i}(t)$	Mean squared displacement
$\sigma_{\alpha\beta}$	Stress tensor

a	Area
$\mathbf{F}_i$	Force on particle i
$\mathbf{U}_i$	Potential for particle i
P	Pressure
$G(t)$	Stress relaxation
ξ_e	Electrostatic blob size
g_e	Number of monomers in a blob
ℓ_B	Bjerrum length
ξ	Reaction coordinate
ξ_{ref}	Reference coordinate
$A(\xi)$	Potential of mean force
$Q(\xi)$	Canonical partition function
K	Spring constant
m_i	Mass of particle i
p_i	Weights for average
S_{mn}	Gyration tensor
λ	Eigenvalues
ψ_s	Asphericity
ψ_c	Acylindricity
κ^2	Relative shape anisotropy
Z_{net}	Net valence
ΔN	$|N_- - N_+|$

Z_head	Net valence of the head
Z_unimer	Crossover from association to dissassociation
$R_\text{core}/R_\text{corona}$	Size of core/ corona
N_c	Number of counterions
σ	Size of monomer
c	concentration
ρ	Density
b	Kuhn length
τ	relaxation time
t	Time
q_i	Valence of particle i
e	Elementary charge
ϵ_0, ϵ_r	Permittivity of vaccuum/solvent
$\mathbf{p}_i$	Monomentum of particle i
$H(\mathbf{p}, \mathbf{r})$	Hamiltonian
$K(\mathbf{p})$	Average kinetic energy
L	Box length
L_e	Entanglement length
L_s	Length between Stickers
N_s	Number of stickers

Chapter 1

Theoretical Background

1.1 Motivation

A polymer is a large molecule consisting of many subunits (monomers) that are covalently bonded. The degree of polymerisation N defines the number of monomers on a polymer chain and is generally a very large number. For example, a single strand of DNA can be 2-3 metres long, yet only around 10^{-9} metres wide. A polymer is a homopolymer if it consists of a single repeated unit, whereas a polymer with differing monomers is a heteropolymer. The architecture of the polymers can be varied, from linear, ring, stars to more complex formations such as dendrimers and Caley trees. In this work we focus on linear polymers.

Polymers are abundant in nature, such as DNA and proteins, but can also be synthetic. One special class of polymers are those with associative groups, as these exhibit interesting features such as self healing, shape memory or stimuli sensitivity [1]. These bonds are formed by these associative groups are physical, not chemical, and are reversible. Some examples include $\pi - \pi$ stacking [2, 3], hydrogen bonding [4, 5, 6, 7]

metal-ligand [8, 9, 10] and ionic interactions [11, 12, 13, 14]. In this work we focus on charged polymers.

Charged polymers have ionizable groups. In certain conditions, for instance polar solvents, these groups dissociate leaving charged monomers on the macromolecules and counterions in the solvent [15, 16, 17, 18]. These polymers can be categorised into two classes: polyelectrolytes (PEs) and polyampholytes (PAs). PEs strictly have either positive or negative charges on the chains, whereas PAs contain both. These charges can be distributed randomly along the polymer backbone, or be separated into sections or blocks. Two examples of PEs are polystyrene sulfonate and DNA. PEs have a wide range of applications, including rheology modifiers, absorbents, coatings, biomedicine [19], colloidal stabilising agents and suspending agents for pharmaceutical delivery systems [20]. An example of a polyampholyte is protein, in which both positive and negative charges are present on a single polymer chain [15]. By varying the pH value of the media, it is possible to synthesize polymers to be either weakly or strongly charged, defined by the fraction f of charged monomers. At a particular pH, known as the isoelectric point, polyampholytes have zero net charge [15]. It is possible to both tune the density of charges along the backbone and the net valence of charged groups. PAs can have differing architectures, such as charges being randomly or alternatively distributed along the chain, or grouped into blocks of similarly charged monomers. The individual blocks can be thought of as polyelectrolytes that are covalently bonded to form block PAs.

Ionomers are flexible polymers with ionic groups distributed along the chain backbone, usually less than 10 mole percent. On the other hand, PEs typically have much higher molar density of ionic groups. Representative examples of ionomers are Nafion

2

and polystyrene sulfonate. Their ionic groups can form ionic clusters in low dielectric solvents [21], which leads to retarded stress relaxation when compared with neutral polymers of similar architectures [22, 23, 24]. The reversibility of ionic bonds allows for the formation of self healing or shape memory materials [1]. There are numerous applications for ionomers, such as rheology modifiers [25], batteries [26] and suspending agents for drug delivery [27, 28].

Systems with very weak electrostatic interactions show no preference for ionic bonding and thus behave as their neutral counterparts [17]. Chain charged groups and counterions undergo pairwise bonding to form dipoles when the electrostatic attraction energy overcomes the entropic penalty [12]. Further increasing of the electrostatic interaction strength leads to the formation of multiplets [12], and it is in this regime that ionic clusters form in the charged polymer systems [21].

Polymeric solutions are created by dissolving polymers in solvent, and range from dilute, semi-dilute to concentrate solutions. In the dilute regime, intrachain behaviour dominates the chain dynamics and the effects of inter-chain interactions can be considered negligible. In semi-dilute solutions, the interchain behaviour begins to play an important role. Beyond this regime, we have concentrate polymer solution or even melt in which inter-chain behaviour dominates. Supramolecular polymer networks can form in both solutions and melts of associative polymers [29, 11, 30].

Depending on the concentration of polymer chains, the distribution of charged monomers along the backbones, and the dielectric constant of the solvent, electrostatic interactions can lead charged polymers to exhibit interesting behaviour such as aggregation, phase separation or formation of percolated networks [29, 31, 32]. The long range electro-

static interactions, coupled with neutral chain relaxation, leads to rich structural and dynamical behaviour of charged polymer systems [14, 30, 33].

1.2 Overview

In the remainder of this chapter we provide an overview of polymer physics with a particular focus on chains with electrostatic interactions. In the next chapter we introduce the simulation model and methodology, including some advanced simulation techniques such as replica exchange molecular dynamics (REMD) and umbrella sampling used in our study.

In Chapter 3 we study the effect that electrostatic interaction strength and structural asymmetry have on the conformational behaviour of single-chain asymmetric diblock polyampholytes. The chapter is split into two parts. Firstly, we study diblock chains with a fixed positively charged block of length N_+, with fraction of charged monomers f_+. Different charge fractions and chain lengths of the negatively charged block are evaluated. We ensure that the chain is electro-neutral by ensuring $N_- f_- = N_+ f_+$. In the second part of Chapter 3, we study chains that have same block charge fractions $f_- = f_+$ but still vary the number of monomers N_-. Thus, the chains are capable of carrying a net charge, and counterions are present to satisfy electro-neutrality. In Chapter 4 we increase the density and study the aggregation behaviour of multi chain asymmetric diblock polyampholytes, each carrying a net charge. We also study the stability of many chain systems of pre assembled aggregates. In chapter 5 we study the static, dynamic and rheological properties of Ionomers in melts. We focus on two systems. Firstly we study so called telechelic chains, which have charges confined on each end monomer. Secondly we study mixture systems consisting of half telechelic

chains and the other half have a single charge on the central monomer, both of same lengths.

1.3   Neutral Polymer Behaviour

The behaviour of charged polymers are determined by two contributing factors, the neutral parent chain behaviour and the Coulombic interactions between charged objects. These two separate contributions are often interfering with each other and lead to difficulty in quantifying the behaviour of charged polymers. In this section we introduce some important concepts relating to neutral polymer systems.

1.3.1   Brownian Motion

Brownian motion describes the behaviour of a molecule interacting with surrounding particles, such as the relationship between a monomer and the solvent. Seemingly random dynamical behaviour of pollen floating in water was first observed by Robert Brown in 1827 [34]. In his 1905 paper, Einstein showed that this seemingly random behaviour was due to the collision of surrounding water molecules with the pollen particle. The diffusion process is governed by Fick's law [35]

$$j(x,t) = -D\frac{\partial c}{\partial x} \tag{1.1}$$

where $j(x,t)$ is the flux and D is the diffusion coefficient. Einstein derived the relationship between the diffusion coefficient D and friction constant ζ for particles undergoing Brownian motion.

$$D = \frac{k_B T}{\zeta}, \tag{1.2}$$

where k_B is the Boltzmann constant and T is the absolute temperature.
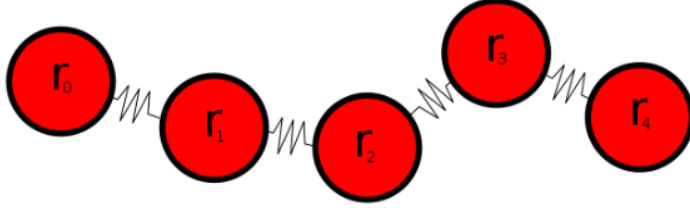
Figure 1.1: Visualisation of the Rouse model.

1.3.2 The Langevin Equation

The motion of a particle in a solvent can be described by the Langevin equation [36]

$$m\frac{d^2\mathbf{r}_i}{dt^2} = -\nabla U(\mathbf{r}_i) - \zeta\frac{d\mathbf{r}_i}{dt} + \Gamma_i(t), \tag{1.3}$$

where $-\nabla U(\mathbf{r}_i)$ are the pairwise interaction forces acting on the particle at position $\mathbf{r}_i$ by other particles, $-\zeta\frac{d\mathbf{r}_i}{dt}$ is the friction force it experienced, and $\Gamma_i(t)$ is the noise term associated with the collision of the solvent molecules. ζ is the friction coefficient, m is the particle mass and t is time.

1.3.3 Ideal Chain

The Rouse model [35] treats the polymer as a chain of N beads, and the covalent bonding is modelled by a harmonic potential

$$U(\mathbf{r}_{i+1,i}) = \frac{3k_BT}{2\hat{b}^2}(\mathbf{r}_{i+1} - \mathbf{r}_i)^2, \tag{1.4}$$

where $\hat{b}^2$ the mean square bond length. In the Rouse model, the inertia term on the left hand side of equation 1.3 will be averaged out over time, and as such is set to zero. The Rouse model is the following set of stochastic differential equations for describing

the motion of the beads

$$\zeta d\mathbf{r}_0 = \frac{3k_BT}{\hat{b}^2}\left(\mathbf{r}_1 - \mathbf{r}_0\right)dt + \sqrt{2k_BT\zeta}d\mathbf{W}_{t0}, \tag{1.5}$$

$$\zeta d\mathbf{r}_i = \frac{3k_BT}{\hat{b}^2}\left(\mathbf{r}_{i+1} + \mathbf{r}_{i-1} - 2\mathbf{r}_i\right)dt + \sqrt{2k_BT\zeta}d\mathbf{W}_{ti}, \tag{1.6}$$

$$\zeta d\mathbf{r}_N = \frac{3k_BT}{\hat{b}^2}\left(\mathbf{r}_{N-1} - \mathbf{r}_N\right)dt + \sqrt{2k_BT\zeta}d\mathbf{W}_{tN}, \tag{1.7}$$

where $\mathbf{W}_{ti}$ is a Wiener process for bead $\mathbf{r}_i(t)$

$$\langle \mathbf{W}_{ti} \rangle = \mathbf{0}$$

$$\langle W_{ti\alpha}W_{t'j\beta} \rangle = \delta_{ij}\delta_{\alpha\beta}\min(t,t')$$

$$\langle \mathbf{W}_{ti} \cdot \mathbf{W}_{t'j} \rangle = 3\delta_{ij}\min(t,t')$$

Rouse chains can be considered ideal because excluded volume effects are neglected from the model.

1.3.4 Real Chain

In reality, monomers have excluded volume (hard cores) and the behaviour of the polymer depends on the solvent it is in. The solvent can be characterised as athermal, good, θ or poor. At high temperatures, the excluded volume becomes independent of temperature, defined as athermal solvent. In good solvents, monomers favour contact with solvent than amongst themselves and the chain swells. In poor solvents, the monomers prefer to stay together and the chain adopts a globular conformation that corresponds to the dense packing of thermal blobs as discussed in the work by DeGennes [37]. The intermediate regime is called θ-solvent, in which the chain statistics follow ideal chain behaviour as the attraction between monomers balances the hard core repulsion.

1.3.5 Static Properties

Mean Squared End to End Distance

The mean squared end-to-end distance R_e^2 of an ideal chain is given by

$$R_e^2 = Nb^2,$$

where N is the degree of polymerization of polymer, and b is the Kuhn length [38]. A real chain scales as follows, $R_e \sim bN^\nu$, where the exponent $\nu = \{0.588, 0.5, 0.333\}$ for good, θ and poor solvents respectively [38].

Mean Squared Radius of Gyration

The squared radius of gyration of a polymer is defined as the average squared distance between monomers in a given conformation, $\{\mathbf{r}_i\}$, and the centre of mass of the chain $\mathbf{r}_{cm}$ [38].

$$r_g^2 = \frac{1}{N} \sum_{i=1}^{N} (\mathbf{r}_i - \mathbf{r}_{cm})^2 \tag{1.8}$$

Rubinstein and Colby [38] show that the average radius of gyration of an ideal linear chain can be related to the average end to end distance via

$$R_G^2 = \langle r_g^2 \rangle = \frac{R_e^2}{6}. \tag{1.9}$$

In a poor solvent it is often more convenient and informative to discuss the radius of gyration, whereas in a good solvent the end to end distance is often a good indicator of the behaviour.

Gyration Tensor

The gyration tensor $\mathbf{S}$ is a 3x3 symmetric matrix that describes the second moments of position of a collection of particles

$$S_{mn} \equiv \frac{1}{2N^2} \sum_{i=1}^{N} \sum_{j=1}^{N} (r_i^m - r_j^m)(r_i^n - r_j^n)$$

where m, n are the relevant Cartesian coordinates of the ith monomer.

1.3.6   Dynamic Properties

The mean squared displacement of monomer i is given by [39]

$$g_{1,i}(t) = \left\langle (\mathbf{r}_i(t) - \mathbf{r}_i(0))^2 \right\rangle. \tag{1.10}$$

Initially $t < \tau^*$, the behaviour is ballistic, in which $g_{1,i}(t) \sim t^2$. For short time $\tau^* < t < \tau_0$ the monomers are seemingly unaware they belong to a chain and freely diffuse $g_{1,i}(t) \sim t^1$. Above this initial lifetime $\tau_0 < t < \tau_R$ the influence of additional friction from tethered monomers plays a role and chain monomers are sub-diffusive in this regime; the end monomers diffuse faster than the middle monomers due to the increased friction imposed on the middle monomers. The chain centre of mass diffuses according to the Rouse power law $g_{1,i}(t) \sim t^{1/2}$.

1.3.7   Rheological Properties

Consider a viscoelastic material in three dimensional coordinate system along axes α, β (replace α, β with x, y, z where appropriate). A volume V can be divided by a plane perpendicular to the β axis. The stress tensor component $\sigma_{\alpha\beta}$ is the force per unit area

on this plane, in the α direction, expressed as

$$\sigma_{\alpha\beta} = \frac{\langle S^\alpha \rangle}{a},$$

where $\langle S^\alpha \rangle$ is the ensemble average of the force in the α-direction and a is the area of the plane. In a charged polymer solution, the force S_α consists of two parts: the force exerted by the solvent S_α^s and the force acted on by other monomers or beads S_α^p. The latter term includes the Coulomb interactions. The stress tensor can then be expressed as

$$\sigma_{\alpha\beta} = \eta_s(\kappa_{\alpha\beta} + \kappa_{\beta\alpha}) + \langle P_r \rangle \delta_{\alpha\beta} - \frac{1}{V} \sum_i \langle F_i^\alpha r_i^\beta \rangle \tag{1.11}$$

where η_s is viscosity of the solvent, P_r is the pressure and $\kappa_{\alpha\beta}$ is the velocity gradient tensor [35]. $\mathbf{F}_i = \{F_i^x, F_i^y, F_i^z\}$ is the total force on particle i. In dilute systems the first term of equation 1.11 dominates, whereas in dense systems the stress can be expressed simply by the last term [35]

$$\sigma_{\alpha\beta} = -\frac{1}{V} \sum_i \langle F_i^\alpha r_i^\beta \rangle.$$

Stress Relaxation

The stress relaxation modulus $G(t)$ is defined as the ratio of stress remaining at time t, after a step strain γ, $\sigma_{\alpha\beta}(t) = \gamma G(t)$, t_0 being the initial observation time. In an equilibrium system, $G(t)$ is calculated from the stress auto-correlation function

$$G(t) = \frac{V}{k_B T} \langle \sigma_{\alpha\beta}(t + t_0)\sigma_{\alpha\beta}(t_0) \rangle \tag{1.12}$$

where α and β are any two orthogonal directions, t_0 is the initial time. For viscoelastic solids, $G(t)$ relaxes to a finite value; whereas $G(t)$ tends to zero for viscoelastic liquids

10

[40].

1.4 Charged Polymer Behaviour

For systems experiencing significant electrostatic interaction strengths, if the net charge on all polymers in the system is zero, solutions that contain oppositely charged polyelectrolytes phase separate into a dense sediment and dilute solution [12]. If a net charge is present, the polyelectrolytes form soluble asymmetrically charged aggregates known as polyelectrolyte complexes [41]. Random polyampholytes with zero net valence per chain phase separate for very small concentrations and the supernatant is dominated by neutral single chains, or unimers, that take spherical globular conformations [42]. For random polyampholyte chains that contain a net charge, the dilute phase has PA chains of elongated necklace conformations [43]. By contrast, block polyampholytes exhibit much more interesting properties. The interaction between oppositely charged blocks is much stronger due to the localisation of similar charges. As such, at the isoelectric point, charge neutral block PAs form much larger precipitates than the random PAs. Stable micelles are theoretically predicted to form when there is a net charge on the block PAs [13].

The theory of neutral polymers is well established [35, 38, 37], however charged systems are far more complex because of the addition of long range Coulombic interactions [44]. Adding salt can effectively screen the long range interactions, depending on the salt concentration [45, 46].

Scaling theories for diblock polyampholytes were developed by Castelnovo and Joanny [47] for solutions with high ionic strength, and by Shusharina et. al. [13] for systems

without the presence of salt. Shusharina et. al. predicted that a single diblock PA chain with zero net valence collapses into a globule, whereas a diblock PA with a net charge forms takes a tadpole shape with globular head and a PE tail. If the surface energy gain for two globular heads to merge is greater than the electrostatic repulsion between them, these PAs aggregate into micelles. Shusharina et al predicted two regimes of a micelle, a dense core of oppositely charged monomers and a more diffusive corona regime made of PE tails that are not part of the core.

Computer simulation provides an invaluable tool in understanding the behaviour of charged polymer systems [36]. Early simulations of diblock polyampholytes were performed for relatively short chains [48] due to the limitations of computer power. As technology progressed, longer chains were able to be studied computationally [12]. Wang and Rubinstein [12] investigated the conformational properties of flexible symmetric diblock PAs over a wide range of electrostatic interaction strengths for various chain lengths and found different regimes upon the change of ionic strength.

Charged polymer systems can be split into two categories, weakly associating and strongly associating, depending on the charge density and strength of electrostatic interaction. Their physical properties are described by different theoretical approaches.

1.4.1   Weakly Associating Charged Polymers

One fundamental theoretical technique in studying charged polymers is the concept of electrostatic blobs [37, 14, 49, 13, 12]. Chain statistics are mostly unperturbed at length scales shorter than the electrostatic blob size ξ_e. The blob size, and number of monomers g_e in a blob, are defined by balancing the thermal and electrostatic parts of

the free energy [12]

$$k_B T \approx \frac{\ell_B k_B T (f g_e)^2}{\xi_e},$$ (1.13)

where k_B is the Boltzmann constant, T is the temperature, f the fraction of charged monomers and the strength of the electrostatic interaction is represented by the Bjerrum length ℓ_B, defined as the distance at which electrostatic interaction energy between two elementary charges equals the thermal energy.

$$\ell_B = \frac{e^2}{4\pi\epsilon_0\epsilon_r k_B T}.$$ (1.14)

where e is the elementary charge and ϵ_0, ϵ_r are the permittivity of vacuum and solvent respectively. see definition in Section 2.1.1. The blob size is related to the number of monomers in the blob

$$\xi_e \approx g_e^\nu \sigma,$$ (1.15)

where σ is the size of a monomer and ν is the scaling exponent related to the solvent (0.33 for poor solvent, 0.5 in a θ solvent and 0.588 in a good solvent). Thus we obtain the following scaling dependencies

$$\xi_e = \sigma \left(\frac{\ell_B f^2}{\sigma} \right)^{-\frac{\nu}{(2-\nu)}}$$ (1.16)

$$g_e = \left(\frac{\ell_B f^2}{\sigma} \right)^{-\frac{1}{(2-\nu)}}$$ (1.17)

If the total number of monomers N in a chain is less than g_e then the chain is almost unperturbed and the chain size follows neutral chain scaling behaviour $R_e \sim N^\nu \sigma$. On the other hand, if there are many blobs per chain then the behaviour is dominated by electrostatic interaction. Charged polymers that satisfy the condition $g_e >> 1$ are weakly association, otherwise if $g_e \sim 1$ they are strongly associating.
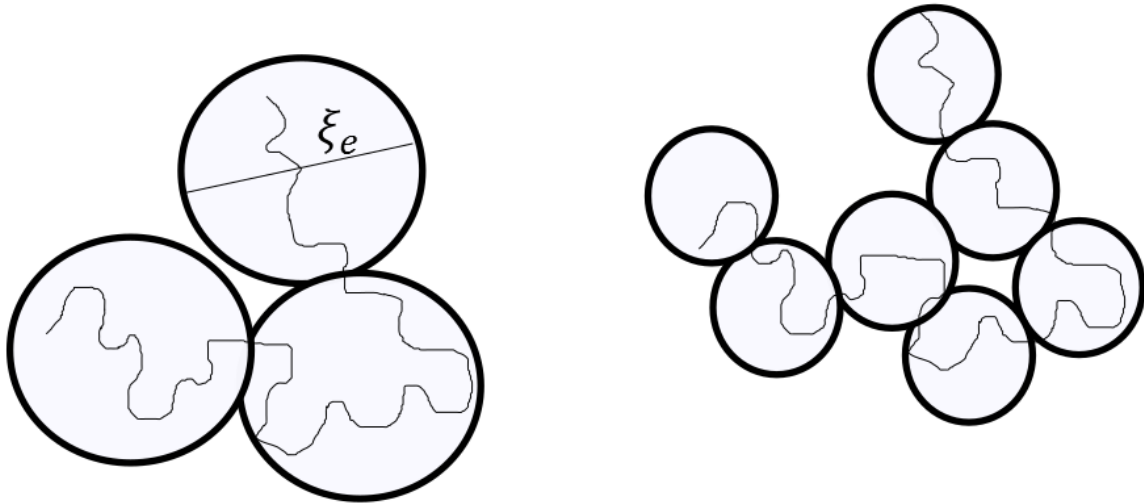
Figure 1.2: Visualisation of different electrostatic blob sizes.

Polyelectrolyte

PE chains in a dilute solution behave similarly to single chains due to the extreme distance, thus the interchain interactions can be considered negligible [17]. For extremely weak electrostatic interactions, the behaviour of the neutral parent chain dominates. On the other hand, for strong enough interactions, the charged behaviour dominates and the PE chain stretches [50] [17]. The size of a weakly charged polyelectrolyte in good and θ solvents can be estimated by

$$R_e \approx \frac{N}{g_e} \xi_e,$$

where the number of electrostatic blobs per chain N/g_e is multiplied by the blob size ξ_e [14] [51], corresponding to a linear array of blobs.

In poor solvents, the neutral polymer would collapse into a globule, however the elec-

trostatic repulsion between likely charged monomers make the chain want to stretch [52]. This leads to necklace-like conformation of the polyelectrolyte chain [14].

Polyampholyte

The conformational behaviour of polyampholytes is largely driven by the charge distribution along the chains, in addition to the neutral parent chain behaviour and ionic strength. Polyampholytes with zero-net valence and random distribution of charges collapse into compact globules [53] [32], whereas random PA chains with a net non-zero charge initially reduce their sizes, then become stretched with increasing electrostatic interaction strength [43]. Polyampholytes with alternating charge arrangement are more soluble than those with random charge distribution [32].

Symmetric diblock polyampholytes collapse into globules due to charge density fluctuation induced attraction [13] and several regimes have been identified depending on charge density [12] and electrostatic interaction strength. As the interaction strength increases beyond the unperturbed regime, the polyampholyte begins to fold [12]. The two blocks can be represented by two oppositely charged large spheres, whose centres of mass are connected via a harmonic spring. At higher interaction strengths the polymers enter a weak association regime and the size of a diblock PA can be described by the dense packing of oppositely charged electrostatic blobs [13],

$$R_{\mathrm{gl}} \approx \xi_e \left(\frac{N}{g_e} \right)^{1/3} \approx \sigma N^{1/3} \left(\frac{\ell_B f^2}{\sigma} \right)^{(1-3\nu)/3(2-\nu)} \tag{1.18}$$

A large portion of this thesis is devoted to asymmetric diblock polyampholytes, and will discuss the behaviour in greater detail in Chapter 3. However, diblock polyampholytes with high asymmetry $N \approx N_-$, the polymer chain is effectively a polyelectrolyte and

the contributions from the positively charged block are negligible.

1.4.2   Strongly Associating Charged Polymers

Polyelectrolytes

The size of strongly charged polyelectrolytes was found to be shorter than originally predicted [14] owing to counterion condensation [54, 55]. In solutions, polyelectrolytes begin to overlap at concentration $c^* \approx N/R_e^3$ [50]. As strongly charged chains are close to being fully stretched $R_e \approx \sigma N$, the overlap concentration scales with the degree of polymerization N as $c^* \approx \sigma^{-3} N^{-2}$ [17]. Comparing with the neutral chain overlap concentration $c^* \sim \sigma^{-3} N^{-\nu}$, it can be observed that polyelectrolytes begin to overlap at much lower concentrations.

At high charge density, a polyelectrolyte chain would be almost fully stretched, $R_e \sim N\sigma$ in the absence of counterions. However counterions can associate with charges on the chain to reduce the line charge density of linear PEs, which has led to the idea of counterion condensation introduced by Manning [54]. Deserno et al [56] studied the counterion distribution around an infinitely long rod in a cell model [57]. The salt free case of this model can be solved analytically by employing the non-linear Poisson-Boltzmann equation [58]. More recently, Manning and Ray [59] constructed a potential between the PE and the counterion. They divide the distribution of counter ions into two regimes, i.e a layer in which a fraction of the counterions are condensed onto the PE, and a second, more diffusive regime resembling Debye-Huckel cloud [59]. A counterion located at the interface between these two regions is repelled from the PE, leading to a sharp boundary between the two regions. Manning and Ray [59] argued that this distinction is detectable as an inflection point in the integrated radial counterion distri-

bution. However Deserno et al [56] pointed out a disagreement between the Manning model and the PB theory without salt and that if the distribution of counterions is plotted against the logarithmic radial distance, an inflection point exists that separates the counterions into condensed and diffusive regimes [56] [60]. Deserno compared PB theory with computer simulations and illustrated the connection between Manning condensation and the inflection point, and then derived a PB equation for the concept of counterion condensation with added salt.

Liu et al [61] studied the behaviour of polyelectrolyte brushes and the effect of counterions on the brush morphology. They observed that flexible brushes with trivalent counterions collapse into octopus-like micelles, however more rigid chains form dendritic condensates. The latter showed much slower relaxation behaviour. Recently Michalowsky et al [62] developed a polarizable MARTINI model [63] [64] for ions in aqueous solution. The introduction of the force field allows for simulation results that are much closer to experiments by eliminating some of the scaling estimates.

Polyelectrolyte complexes are of great interest for their multitude of applications, such as drug delivery capsules [65] and PE films [66]. Zhang et al [67] studied the effects that asymmetric concentrations have on the complexation behaviour. Mixtures of oppositely charged polyelectrolytes have been studied extensively in the literature [68] [69]. Electrostatic interaction can cause these systems to phase separate into a dense phase made up of mostly PEs and a dilute supernatant.

Polyampholytes

If the electrostatic attraction strength is large enough to overcome the entropic penalty, oppositely charged monomers and their counterions bind into dipoles. Further increase

in electrostatic interaction strength leads to the formation of higher order multiplets [12].

Chapter 2

Simulation Methodology

2.1 Molecular Dynamics

Molecular Dynamics (MD) is a numerical simulation method for studying trajectories of molecules. Each particle in the N body system has its own well-defined set of forces. The trajectories are found by numerically solving Newtons equations of motion for the interacting particles.

2.1.1 Pair Interactions

In our polymer simulations, the chains are expressed by the Kremer Grest bead spring model [70], and counterions are modelled explicitly as beads that do not have any springs as they are not covalently bonded. The pairwise excluded volume of two monomers (beads) i and j, a distance r_{ij} apart, is modelled by the Lennard Jones Potential

$$U^{\text{LJ}}(r_{ij}) = 4\epsilon_{\text{LJ}} \left[\left(\frac{\sigma}{r_{ij}} \right)^{12} - \left(\frac{\sigma}{r_{ij}} \right)^{6} \right], \tag{2.1}$$

19

where σ is the bead diameter (size of the monomer), which we have chosen to be uniform in all simulations. and ϵ_{LJ} is the depth of the attractive well. To save on computation time, the truncated at a cut off distance of r_c. Where $r_c = 2.5\sigma$ or $2^{1/6}\sigma$ in a poor and good solvent respectively. Thus, the truncated and shifted form of the Lennard Jones potential is

$$U^{\text{LJ}}(r_{ij}) = 4\epsilon_{\text{LJ}} \left[\left(\frac{\sigma}{r_{ij}}\right)^{12} - \left(\frac{\sigma}{r_{ij}}\right)^{6} - \left(\frac{\sigma}{r_{\text{cut}}}\right)^{12} + \left(\frac{\sigma}{r_{\text{cut}}}\right)^{6} \right] \tag{2.2}$$

If beads i, j are covalently bonded, then this interaction is modelled by the finitely extensible non-elastic (FENE) potential

$$U^{\text{FENE}}(r_{ij}) = -\frac{1}{2} K_{\text{FENE}} R_0^2 \ln\left(1 - \frac{r_{ij}^2}{R_0^2} \right), \tag{2.3}$$

where R_0 is the maximum extension and K_{FENE} is the FENE constant.

The Coulomb potential describes the electrostatic interactions between charged beads i and j

$$U^{\text{COUL}}(r_{ij}) = k_B T \ell_B \frac{q_i q_j}{r_{ij}} \tag{2.4}$$

where q_i is the valence of bead i.

2.2 Replica Exchange

2.2.1 Parallel Tempering

For strongly associated polymer systems, it is usually very difficult to obtain reliable equilibrium properties using conventional simulation methods because these systems are typically trapped in one of many meta stable local minimum energy states [71].

There are a number of advanced methods that have been developed to overcome for this difficulty, such as simulated tempering [72, 73] or multicanonical ensemble method [74, 75], One other such method is Parallel tempering (PT), also known as Replica Exchange (RE) [76, 77, 71]. which was first devised by Swendsen and Wang [78]. The idea of PT is to simulate M replica systems over varying temperatures T_i. For simplicity, one can choose $T_{i-1} < T_i$. These replicas do not interact, however after a given time an attempt is made to swap the configuration $C_i \in T_i$ with neighbouring replica system T_{i-1} or T_{i+1}. Simulating a system at M different temperatures, parallel tempering is at least $1/M$ times more efficient than the conventional Monte Carlo [77], because the low temperature system is able to explore regions of the phase space that may not be accessible in a single temperature MC simulation that was M times as long.

2.2.2   Replica Exchange Molecular Dynamics

Swendsen and Wang [78] developed parallel tempering (replica exchange). They created replicas of a system of interest at a series of temperatures, and partially exchanged information between adjacent temperatures via Monte Carlo simulations. Complete information exchange was presented by Geyer [79]. The general idea of parallel tempering (PT) is to create M replicas of a system, usually at different temperatures. Low temperature simulations are likely to become trapped in one of many metastable states, whereas high temperature simulations are more likely to overcome the high energy barriers and explore larger volumes of the phase space. Hansmann [80] applied the parallel tempering method to biomolecules, and Sugita and Okamoto formulated a replica exchange method based on molecular dynamics (REMD). Fukushini et al [81] developed a Hamiltonian PT method, which allows for the formulation of replica exchanges with alternative parameters.

The acceptance probability ϕ in Hamiltonian PT when attempting to swap replicas i and j is [77]

$$\phi = \min \left\{ 1, \exp \left[-\beta \left([H_i(\mathbf{X}') + H_j(\mathbf{X})] - [H_i(\mathbf{X}) + H_j(\mathbf{X}')] \right) \right] \right\}, \tag{2.5}$$

where $H_i(X)$ is the Hamiltonian of configuration $\mathbf{X} = (\mathbf{r}, \mathbf{p})$, where $\mathbf{r}$ and $\mathbf{p}$ are the positions and momentums of all the particles. X, X' are the configurations in i,j respectively, prior to swapping. The Hamiltonian is the sum of the Kinetic and Potential energies

$$H(\mathbf{r}, \mathbf{p}) = K(\mathbf{p}) + U^{\text{TOT}}(\mathbf{r}) = \sum_{k=1}^{N} \frac{\mathbf{p}_k^2}{2m_k} + U^{\text{TOT}}(\mathbf{r}). \tag{2.6}$$

The average kinetic energy $\langle K(\mathbf{p}) \rangle = \frac{3}{2} N k_B T$ [71], and in our system,

$$U^{\text{TOT}}(\mathbf{r}) = U^{\text{COUL}}(\mathbf{r}) + U^{\text{FENE}}(\mathbf{r}) + U^{\text{LJ}}(\mathbf{r}). \tag{2.7}$$

If we wish to create replicas with Bjerrum length ℓ_B as our parameter choice, then replica i with Bjerrum length $\ell_{B,i}$

$$H_i(\mathbf{r}, \mathbf{p}) = K(\mathbf{p}) + U_i^{\text{COUL}}(\mathbf{r}) + U^{\text{FENE}}(\mathbf{r}) + U^{\text{LJ}}(\mathbf{r}), \tag{2.8}$$

as only the Coulomb energy component relies on the Bjerrum length. For convenience, we define $U_i^*(\mathbf{r}) = U_i^{\text{COUL}}(\mathbf{r})/(k_B T \ell_{B,i})$, the $\ell_{B,i}$ and $k_B T$ independent contribution to the Coulomb energy.

Thus, highlighting the exponent of equation 2.5

$$-\beta([H_i(\mathbf{X'}) + H_j(\mathbf{X})] \quad - \quad [H_i(\mathbf{X}) + H_j(\mathbf{X'})]) = \tag{2.9}$$

$$-\beta([U_i^{\mathrm{TOT}}(\mathbf{r'}) + U_j^{\mathrm{TOT}}(\mathbf{r})] \quad - \quad [U_i^{\mathrm{TOT}}(\mathbf{r}) + U_j^{\mathrm{TOT}}(\mathbf{r'})]) = \tag{2.10}$$

$$-\beta([U_i^{\mathrm{COUL}}(\mathbf{r'}) + U_j^{\mathrm{COUL}}(\mathbf{r})] \quad - \quad [U_i^{\mathrm{COUL}}(\mathbf{r}) + U_j^{\mathrm{COUL}}(\mathbf{r'})]), \tag{2.11}$$

as the average kinetic energy is the same for both replicas i,j and $U^{\mathrm{FENE}}, U^{\mathrm{LJ}}$ do not depend on ℓ_B. Substituting in $U^*(\mathbf{r})$,

$$\ell_{B,i}U^*(\mathbf{r'}) + \ell_{B,j}U^*(\mathbf{r}) \quad - \quad \ell_{B,i}U^*(\mathbf{r}) - \ell_{B,j}U^*(\mathbf{r'}) = \tag{2.12}$$

$$(\ell_{B,i} \quad - \quad \ell_{B,j})(U^*(\mathbf{r'}) - U^*(\mathbf{r})). \tag{2.13}$$

Substituting this back in to equation 2.5 yields a simple expression for finding the acceptance probability.

2.2.3 Testing the Replica Exchange Molecular Dynamics Model

Nymeyer [82] studied the efficiency of REMD analytically by comparing REMD with conventional MD in the study of two protein systems. They found that choosing the maximum temperature too high can greatly reduce the efficiency when compared with regular MD. To check that it is worth running REMD for our systems, we ran a couple of test simulations of our highest interaction strength, longest chain.

Figure 2.1 shows the overall average Coulomb energy profile for the system $f_- = 1/32$ and $\ell_B = 8.0\sigma$, obtained using attempted swapping frequency of once every 500 time steps (red) and normal molecular dynamics (black), both with step size $\Delta t = 0.001$. In this system, we begin with two neutral chains, assign the charges and allow the chains

23
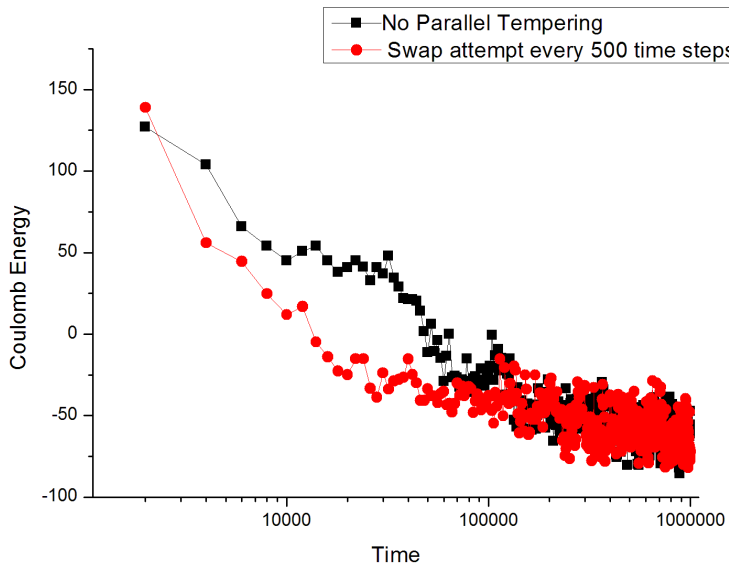
Figure 2.1: Coulomb energy, highlighting generic MD getting trapped in a meta stable state, $\ell_B = 8.0\sigma$, $f_- = 1/32$, $N_+ = 32$

to relax. The generic molecular dynamic simulation can be observed getting trapped in a metastable configuration for around a decade. This graph shows us that for this model system, REMD approaches equilibrium faster than normal molecular dynamics and thus we are less likely to be running into the issues described by Nymeyer.

Swap Acceptance Ratio

The optimal choice of temperatures for parallel tempering has been discussed in the literature [71, 78, 80, 77]. Kofke [83] showed that for a system with constant heat capacity, a uniform acceptance ratio of swaps can be obtained by taking a Geometric progression where T_i/T_{i-1} is constant. Furthermore, ref [84] discusses in detail the optimal allocation of replicas in parallel tempering simulations. They showed that 20% swap acceptance is optimum. We followed these suggestions in our simulations and found in section 3.2, an optimal Bjerrum length distribution $l_{B,i}/l_{B,i-1} = 1.3\sigma$, which yielded

during the test runs a uniform distribution of acceptance ratios of approximately 22.5%. Our test simulation was for a system with through tuning during initial equilibration of the system $f_- = 1/32$, $N_+ = 32$, $N_+ f_+ = N_- f_-$. However, the relationship between the acceptance rate and the electrostatic strength difference depends on the system parameters and as such further fine tuning is required during equilibration to determine the optimal distribution. In our final simulations, we set our Bjerrum lengths to integer values, and swapped these systems. The ratio is not uniform ($3/2 = 1.5$, $8/7 \approx 1.14$), but as we are interested behaviour at a wide range of Bjerrum lengths, the very slight decrease in swap acceptance of the higher interaction strengths is offset by using much less computing power, as we can treat each replica as a simulation of interest at sensible data points if integer values are used.

2.2.4 Advanced Techniques

Although not directly relevant in this work, it is worth discussing briefly current progresses in advanced simulation techniques. Much of the recent literature is focused on replica exchange with solute tempering (REST) [85, 86, 87, 88, 89]. This method is relevant to systems that need to explicitly solve the solvent, and the main aim is to scale the potential energy with temperature so that the polymer molecules get hotter, however the solvent remains cold, and has been shown to be considerably more efficient than generic REMD for these systems [88].

2.3   Numerical Integration Scheme

2.3.1   Velocity Verlet

For a system with N particles, we can write Newton's equations of motion as

$$\frac{d\mathbf{r}_i(t)}{dt} = \mathbf{v}_i(t), \tag{2.14}$$

$$\frac{d\mathbf{v}_i(t)}{dt} = \mathbf{a}_i(t) = \frac{\mathbf{F}_i(t)}{m}, \tag{2.15}$$

where in our system $\mathbf{F}_i = F(\mathbf{r}_i(t)) - m\zeta\mathbf{v}_i(t) + \sqrt{2m\zeta k_B T}\nu(t)$ is the force acting on particle i, and $\nu(t)$ is a noise function, see Equation 1.3

The Velocity Verlet method [36] has the advantage of storing positions $\mathbf{r}_i$, velocities $\mathbf{v}_i$ and accelerations $\mathbf{a}_i$.

$$\mathbf{r}_i(t + \Delta t) = \mathbf{r}_i(t) + \Delta t\mathbf{v}_i(t) + \tfrac{1}{2}\Delta t^2\mathbf{a}_i(t) \tag{2.16}$$

$$\mathbf{v}_i(t + \Delta t) = \mathbf{v}(t) + \tfrac{1}{2}\Delta t\left[\mathbf{a}_i(t) + \mathbf{a}_i(t + \Delta t)\right] \tag{2.17}$$

The algorithm requires two stages. Firstly, new positions at time $t + \Delta t$ must be calculated (Eq 2.16), and mid step velocities are calculated via

$$\mathbf{v}(t + \tfrac{1}{2}\Delta t) = \mathbf{v}(t) + \tfrac{1}{2}\Delta t\mathbf{a}(t). \tag{2.18}$$

The second stage is to calculate the forces and accelerations at time $t + \Delta t$, and complete the velocity step

$$\mathbf{v}(t + \Delta t) = \mathbf{v}(t + \tfrac{1}{2}) + \tfrac{1}{2}\Delta t\mathbf{a}(t + \Delta t). \tag{2.19}$$

This algorithm gives the positions, velocities and forces. Calculating the velocity at each step allows us to test the conservation of the total energy. The Velocity Verlet integrator is a symplectic integrator.

2.4 Periodic Boundary Conditions

Due to the inherent computational cost of simulating N body problems, especially the inclusion of long range Coulomb interactions, several numerical techniques must be employed to obtain reliable data. In addition to this, polymers behave differently near surfaces [36]. If one is not interested in simulating the behaviour near surfaces, periodic boundaries can be employed. A cubic box of length L is created containing a representative amount of particles, and replicated in all directions to create an infinite lattice. As a particle diffuses throughout the simulations and crosses the periodic boundary, its image reappears across the opposite boundary. A two dimensional representation can be found in fig. 2.2. In semi dilute/ dense systems, the polymer is able to diffuse and eventually is replaced by its image. For excluded volume and charge calculations, one must take into consideration the images. The images do not effect the calculation of the FENE potential.

2.5 Long Range interactions

As established earlier, charge-charge interactions are long range and decay $U(r_{ij}) \sim r^{-1}$. Typical simulation box sizes are too small to neglect the effects from an image, especially in dense systems. Increasing the box size and number of polymers can be extremely expensive, especially because the simulation time is proportional to N^2, as each particle
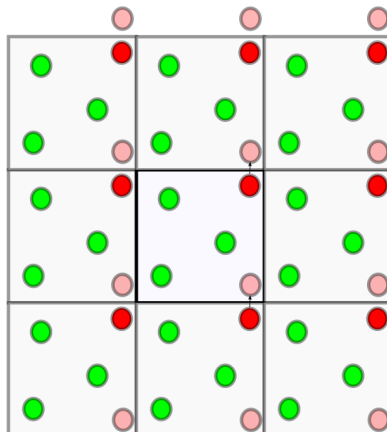
Figure 2.2: Two-dimensional visualisation of particles in simulation box surrounded by periodic images.

interacts with each other particle in long range systems.

Assuming straight forward truncation would lead to undesirable artificial surface effects when an ion crosses into the sphere surrounding the target ion.

2.5.1 Ewald Summation

The Ewald sum splits the slowly converging sum of long range potential into two sums that converge relatively quickly [90, 36]. The total electrostatic energy is

$$U_{\mathrm{coul}} = \frac{1}{2} \sum_{i,j=1}^{N_{\mathrm{part}}} {\sum_{\mathbf{n} \in \mathbb{Z}^3}}' \frac{q_i q_j}{|\mathbf{r}_{ij} + \mathbf{n}L|} \tag{2.20}$$

where the sum over $\mathbf{n}$ takes into consideration the periodic images. The prime is used to show that $\mathbf{n} = 0$ is not included when $i = j$. [90]. The main aim of Ewald summation

is to split the potential using the trivial identity

$$\frac{1}{r} = \frac{f(r)}{r} + \frac{1 - f(r)}{r}.$$ (2.21)

The first part must be negligible for $r > r_{\max}$ and the latter must be slowly varying. Traditionally f is chosen to be the complimentary error function $erfc(r)$ which leads to the Ewald formula

$$U_{\mathrm{coul}} = U_{\mathrm{coul}}^r + U_{\mathrm{coul}}^k + U_{\mathrm{coul}}^s + U_{\mathrm{coul}}^d$$ (2.22)

where the contributions from the real, reciprocal, self and dipole corrections are given by

$$U_{\mathrm{coul}}^r = \frac{1}{2} \sum_{i,j} \sum_{\mathbf{m}in\mathbb{Z}^3}' q_i q_j \frac{\mathrm{erfc}(\alpha|\mathbf{r}_{ij} + \mathbf{m}L|)}{|\mathbf{r}_{ij} + \mathbf{m}L|}$$ (2.23)

$$U_{\mathrm{coul}}^k = \frac{1}{2} \frac{1}{L^3} \sum_{\mathbf{k} \neq 0} \frac{4\pi}{k^2} e^{-k^2/4\alpha^2} |\tilde{\rho}(\mathbf{k})|^2$$ (2.24)

$$U_{\mathrm{coul}}^s = -\frac{\alpha}{\sqrt{\pi}} \sum_i q_i^2$$ (2.25)

$$U_{\mathrm{coul}}^d = \frac{2\pi}{(1 + 2\epsilon')L^3} \left(\sum_i q_i \mathbf{r}_i \right)^2$$ (2.26)

here, $\alpha = 2.5$ is defined as the Ewald Parameter in the literature [36, 90] and the Fourier transformed charged density is [90]

$$\tilde{\rho}(\mathbf{k}) = \int_{V_b} \mathrm{d}^3 r \rho(\mathbf{r}) e^{-i\mathbf{k}\cdot\mathbf{r}} = \sum_{j=1}^{N_{\mathrm{part}}} q_j e^{-i\mathbf{k}\cdot\mathbf{r}_j}$$ (2.27)

P3M

The p3m method modifies the method to allow for the application of Fast Fourier Transforms (FFTs) [91] and the details of the difficulties and application of this modification

29

is covered in detail by the literature [90]. Firstly, the charges must be replaced by a grid based charge density ρ_M.

$$\rho_M(\mathbf{r}_p) \;=\; \frac{1}{h} \int_0^L dr W(\mathbf{r}_p - \mathbf{r}) \rho(\mathbf{r}) \tag{2.28}$$

$$=\; \frac{1}{h^3} \sum_{i=1}^{N_{\text{part}}} q_i W(\mathbf{r}_p - \mathbf{r}_i) \tag{2.29}$$

where $\mathbf{r}_p$ is a discrete coordinate system, separated by $h = 1/M$ and W is the charge assignment function [90]. The simplest solution for solving with the discrete mesh is to use the PME method [91] or the SPME method [92]. Alternatively, there is the P3M method [93].

2.6   Umbrella Sampling

Systems that have an energy barrier separating two regions in configuration space may suffer from poor sampling, or even remain upsampled in reasonable computing times. For example, comparing associative polymers in the associated and disassociated regimes will enter a transitional state relatively infrequently. Furthermore, two chains that are significantly far apart may prefer to be associated, but this may not be observed in the simulation time frame. Understanding the free energy differences between these two states helps to quantify the behaviour.

The Helmholtz free energy is given by $A = -1/\beta \ln Q$, where Q is the canonical partition function [94]. Q is calculated by integrating over the whole phase space, and if the potential energy U does not depend on momentum [94],

$$Q = \int \exp\left[-\beta U(r)\right] d^n r \tag{2.30}$$

where n denotes the total degrees of freedom. We can take a reaction coordinate ξ to distinguish two states, in the aforementioned example we could take the reaction coordinate to be the physical distance between the centres of mass of the polymers. Thus, we can evaluate the probability distribution along ξ by integrating over all degrees of freedom

$$Q(\xi) = \frac{\int \delta\left[\xi(r) - \xi\right] \exp\left[(-\beta U)\right] d^n r}{\int \exp\left[(-\beta U)\right] d^n r}. \tag{2.31}$$

So, $A(\xi) = -1/\beta \ln Q(\xi)$ is the free energy along ξ, which is also known as the potential of mean force (PMF). Equation 2.31 is not possible to solve in computer simulation, but if the system is ergodic then the ensemble average $Q(\xi)$ is equivalent to the time average [94]

$$P(\xi) = \lim_{t \to \infty} \frac{1}{t} \int_0^t p(\xi(t')) dt' \tag{2.32}$$

where p counts the occurrence of ξ. Of course, we are limited by the time it takes to run a simulation. Several methods have been developed to 'force' a system to sample rare events, such as thermodynamic integration [94]. We will focus on Umbrella Sampling (US) [95]. US works by evaluating sections of ξ at different intervals (windows) and combining the results in post processing to obtain the PMF $A(\xi)$. To ensure computation at intervals of ξ, a biased potential is introduced, such as a harmonic spring between the centres of mass.

These bias potentials can be chosen in such a way that the segmented distributions overlap, thus covering the phase space. For example, Withers et al [96] evaluate the second virial coefficient of a polymer solution by introducing a spring that connects the centres of mass of two chains. Take a bias potential $\omega_i(\xi)$ in window i. The potential

31

energy of the system in this window is [94]

$$U^b(\mathbf{r}) = U^u(\mathbf{r}) + \omega_i(\xi) \tag{2.33}$$

where b,u denote biased/unbiased respectively.

To evaluate the unbiased PMF $A_i(\xi)$ one needs to find the unbiased distribution,

$$P_i^u(\xi) = \frac{\int \exp\left[-\beta U(\mathbf{r})\right] \delta\left[\xi'(\mathbf{r}) - \xi\right] d^n\mathbf{r}}{\int \exp\left[-\beta U(\mathbf{r})\right] d^n\mathbf{r}}. \tag{2.34}$$

One can obtain the biased distribution from simulation, and

$$P_i^b(\xi) = \frac{\int \exp\left[-\beta(U(\mathbf{r}) - \omega_i(\xi'(\mathbf{r})))\right] \delta\left[\xi'(\mathbf{r}) - \xi\right] d^n\mathbf{r}}{\int \exp\left[-\beta(U(\mathbf{r}) - \omega_i(\xi'(\mathbf{r})))\right] d^n\mathbf{r}}. \tag{2.35}$$

It can be shown [94] that

$$P_i^u(\xi) = P_i^b(\xi) \exp\left[\beta \omega_i(\xi)\right] \langle\exp\left[-\beta \omega_i(\xi)\right]\rangle \tag{2.36}$$

and thus

$$A_i(\xi) = -(1/\beta) \ln P_i^b(\xi) - \omega_i(\xi) + F_i. \tag{2.37}$$

if one window spans the range of ξ, then F_i can be chosen arbitrarily and the $P_i(\xi)$ can be obtained from simulation, with $\omega_i(\xi)$ chosen prior to simulation. If windows need to be combined, then there are several techniques umbrella integration [94], however in this work we focus on the Weighted Histogram Analysis Method (WHAM) [94].

2.6.1 Weighted Histogram Analysis Method (WHAM).

WHAM was proposed by Kumar et al [97]. When combining the windows, the global distribution can be given by the weighted average of the windows [94]

$$P^u(\xi) = \sum_i^{N_w} p_i(\xi) P_i^u(\xi). \tag{2.38}$$

where N_w are the number of windows and the weights are [94]

$$p_i = \frac{a_i}{\sum_j a_j}, \tag{2.39}$$

$$a_i(\xi) = N_i \exp\left[-\beta\omega^i(\xi) + \beta F_i\right] \tag{2.40}$$

where N_i is the number of steps sampled for the ith window. F_i can be calculated using

$$\exp(-\beta F_i) = \int P^u(\xi) \exp\left[-\beta\omega_i(\xi)\right] d\xi \tag{2.41}$$

Using an initial guess for F_i, One can iterate between 2.38 and 2.41 until convergence [94].

2.7 Shape Describers

As the gyration tensor $\mathbf{S}$ is a symmetric 3x3 matrix and the principal moments are given by the eigenvalues λ_x, λ_y, λ_z of $\mathbf{S}$, which can be selected so that $\lambda_x^2 \leq \lambda_y^2 \leq \lambda_z^2$ [98, 99]. These eigenvalues relate to the squared radius of gyration by

$$R_g^2 = \lambda_x^2 + \lambda_y^2 + \lambda_z^2$$

The asphericity ψ_s is defined by

$$\psi_s \equiv \lambda_z^2 - \frac{1}{2}\left(\lambda_x^2 + \lambda_y^2\right). \tag{2.42}$$

which is equal to zero when the particles take a uniform distribution on the surface of a sphere.

The acylindricity ψ_c is defined by

$$\psi_c \equiv \lambda_y^2 - \lambda_x^2. \tag{2.43}$$

which is equal to zero when the particles sit in a perfect line. The relative shape anisotropy κ^2 is defined by

$$\kappa^2 \equiv \frac{\psi_s^2 + (3/4)\psi_c^2}{R_g^4} \tag{2.44}$$

κ^2 is zero for a sphere and one for a line. This allows us to study more complex shapes than the radius of gyration.

2.8 Efficient on the Fly Calculations of the Auto Correlation Function

Studying the auto correlation functions is an important tool in understanding the behaviour of molecular systems. Whilst instantaneous changes in the force $\Delta f(t)$ usually do not yield useful information, $\langle \Delta f(t)\Delta f(0)\rangle$ does. A major problem is that evaluating these functions can be incredibly computationally expensive, especially in

34

regards to common molecular dynamics simulation times ($\approx 10^8$). Based on the algorithm proposed by Frenkel [100] we implement the multiple τ operator method as introduced by Ramirez et al [101]. A more detailed formulation can be found in [101], but the idea is to create a hierarchical box structure that allows for adjustable sampling frequencies. We create a table that remembers past values of the stress tensor $\boldsymbol{\sigma}_0 = \{\sigma_{xx}(t), \sigma_{xy}(t), ..., \sigma_{zz}(t)\}$ such as

$\boldsymbol{\sigma}^0_0$	$\boldsymbol{\sigma}^0_{-1}$	$\boldsymbol{\sigma}^0_{-2}$	$\boldsymbol{\sigma}^0_{-3}$	$\boldsymbol{\sigma}^0_{-4}$	$\ldots$	$\ldots$	$\ldots$
$\boldsymbol{\sigma}^1_{-3/2} = (\boldsymbol{\sigma}^0_{-1} + \boldsymbol{\sigma}^0_{-2})/2$	$\boldsymbol{\sigma}^1_{-5/2} = (\boldsymbol{\sigma}^0_{-3} + \boldsymbol{\sigma}^0_{-4})/2$	$\ldots$	$\ldots$	$\ldots$	$\ldots$	$\ldots$	$\ldots$
$\boldsymbol{\sigma}^2_{-2} = (\boldsymbol{\sigma}^1_{-3/2} + \boldsymbol{\sigma}^1_{-5/2})/2$	$\ldots$	$\ldots$	$\ldots$	$\ldots$	$\ldots$	$\ldots$	$\ldots$
$\ldots$	$\ldots$	$\ldots$	$\ldots$	$\ldots$	$\ldots$	$\ldots$	$\ldots$

And we solve equation 1.12 for each row of the table. We use 16 columns. This leads to very accurate early time results of the stress relaxation; less so for higher order time. However, this method cuts down the total analysis time by allowing us to calculate the stress relaxation during the simulation run (on the fly), without running into memory issues by storing $\boldsymbol{\sigma}$ for every time step. Furthermore, time is also saved by not needed to run the analysis post process. Where appropriate, we run ten simulations of each system to obtain better long term statistics, but there is still noise present.

For charged systems in this work we study the stress relaxation in two ways. Firstly, the stress tensor including only the neutral contributions to the stress, and secondly, the real space contributions are included. For discussion on including the long range contributions, see Appendix B.2.

Chapter 3

Single Chain

3.1 Introduction

In this chapter we study the static properties of single chain diblock polyampholytes in equilibrium using the Replica Exchange Molecular Dynamics method outlined in chapter 2. In chapter 4 we will discuss in greater detail the aggregation behaviour of diblock polyampholytes, however it is imperative to understand the single chain behaviour. There are experimental techniques to study structural properties of polymers in a laboratory, such as small angle [102, 103] or dynamic light scattering [104], however certain behaviours are difficult to observe with present technology due to time and length scale limits.

Wang and Rubinstein [12] studied the conformational behaviour of symmetric diblock polyampholytes via both scaling theory and molecular dynamics. They identified three main regimes determined by the electrostatic interaction strength. For small Bjerrum length ℓ_B, the chain as a whole folds but each block swells slightly. The folding is caused by association of oppositely charged blocks, and the stretching by self repulsion

of same charged ions on each block. The second regime is weak association, and chain conformation in this regime can be explained by the dense packing of electrostatic blobs [13]. The last regime is strong association in which the charged monomers are able to overcome the entropic penalty and begin binding to oppositely charged ones. At the onset of this regime, dipoles form by charged monomer pairing. Increasing electrostatic interaction strengths leads to the formation of increasing orders of multiplets [12], similar to those observed in ionomers [30].

The behaviour of single chains is difficult to observe in experiments with current technology. Experimentally, diblock polyampholytes have been shown to associate into stable micelles over a wide range of solution pH [105, 106].

In this chapter we study asymmetric diblock polyampholytes. Firstly, we study chains with positively charged block length N_+ and charge fraction f_+. The composition of the negatively charged block is chosen so that the chain carries zero net valence, specifically $N_+ f_+ = N_- f_-$. In the second half of this chapter, we study chains with fixed positively charged block length N_+ and global charge fraction $f = f_- = f_+$, however these chains are able to carry a net charge by increasing N_-.

3.2 Asymmetric Diblock Polyampholytes Carrying Zero net Charge, $N_- f_- = N_+ f_+$, $N_- \geq N_+$

3.2.1 Polymer Models and Simulation Methods

The polymers are represented using the Kremer Grest bead-spring model [70], see Section 2.1.1. Each chain consists of N monomers split into positively and negatively

charged blocks of lengths N_+ and N_- respectively. The charges are chosen to be uniformly distributed along each block. We focus on polymers with block length $N_+ = 32$, and positive charge fraction $f_+ = 1/2$ over a range of Bjerrum lengths $\ell_B/\sigma = \{0.25, 0.5, 1.0, 2.0, 4.0, 8.0\}$. The fraction of charged monomers on the negatively charged blocks $f_- = \{1/2, 1/4, 1/8, 1/16, 1/32\}$, thus $N_- = \{32, 64, 128, 256, 512\}$. As all charges are contained on the chain, which is overall charge neutral, periodic boundary conditions are not required and the electrostatic interactions can be calculated via direct summation. We are interested in polymers in a good solvent and thus we take $\epsilon_{\mathrm{LJ}} = 1.0$ and $r_{\mathrm{cut}} = 2^{1/6}\sigma$ for the LJ interactions. For the FENE coefficients we choose $k_{\mathrm{FENE}} = 7.0$ and $R_{\mathrm{FENE}} = 2.0$ to be consistent with the literature [12].

To study the conformational behaviour, we employ REMD [71, 77, 80] with swaps in the Bjerrum space as laid out in Section 2.2.2. To start the simulation, a neutral polymer is generated as a self-avoiding random walk [36] and allowed to warm up in the absence of charge. The next stage is to turn on the charges and run frequent REMD swaps to ensure that the highly charged systems are not getting caught in an unrepresentative metastable state. Without REMD, the $N = 384$ and $\ell_B/\sigma = 4.0$ system takes approximately 2×10^6 time steps for the radius of gyration to relax to its equilibrium value. We run frequent swap attempts every 5×10^3 time steps for 10^7 time steps, with an average successful swap every 25×10^3 time steps. The choice of replica distances is essential, as too far apart they swap too infrequently, and too close they swap more than the desired amount. There is no way of knowing a priori the ideal distances. However this can be done by studying the swap ratio of shorter runs. Attempting a swap every 10^6 time steps with an acceptance ratio of approximately 20 % [71] yields an average successful swap approximately 5×10^6 time steps. If any dynamical or stress relaxation analysis is required then analysis should only be performed between swaps to ensure

38

adherence to physical behaviour.

3.2.2 Simulation Results

Visualisation
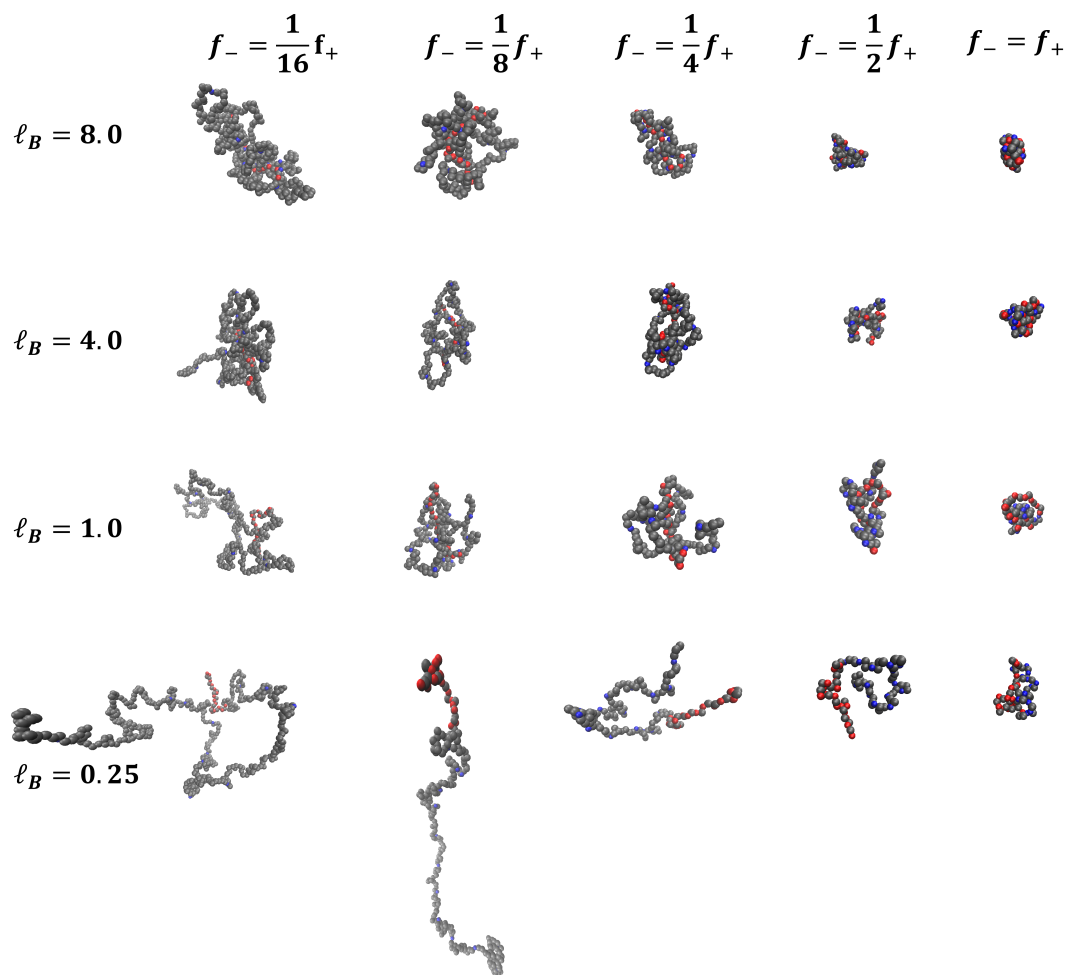
Figure 3.1: Snapshots of the asymmetric net neutral PA chains $N_- f_- = N_+ f_+$, with $N_+ = 32$ and $f_+ = 1/2$ for selected Bjerrum lengths $\ell_B/\sigma = \{0.25, 1.0, 4.0, 8.0\}$

Figure 3.1 shows representative snapshots for the systems analysed. The symmetric chains ($f_+ = f_-$) take globular conformations as expected from the literature [12, 13].
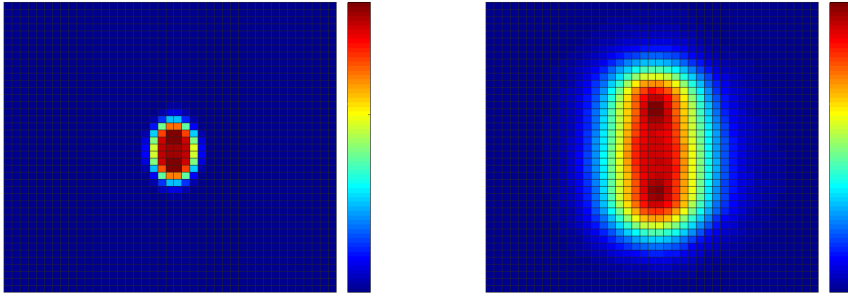
(a) Distribution of $f_- = f_+$, $\ell_B/\sigma =$ 8.0

(b) Distribution of $f_- = f_+/16$, $\ell_B/\sigma = 8.0$ (All charged monomers)

Figure 3.2: Visualisation of the distribution of all charged monomers of the chains. The symmetric case forms a tightly packed globule and the asymmetric forms a cylindrical shape. with the shorter block extending along the principle axis

In the absence of charge, the chains behave like neutral polymers with length N. At low electrostatic interaction strength, an increase in the neutral segment length between negatively charged monomers as $1/f_-$ yields a swelling of the shorter positively charged block. As the Bjerrum length ℓ_B increases more negatively charged monomers tend to associate with the positively charged ones. If the asymmetry is low, this leads to the collapse of the diblock PA chain. But if the asymmetry is high, or f_- is small, the conformational entropy of the longer block forces the chain to take the conformation of a bottle brush with the shorter block working as the back bone.

Figures 3.2a - 3.3b present a visualisation of the distribution of monomer distributions for further visualisation. The symmetric case in Figure 3.2a shows a densely packed globule, as expected in the literature [12]. Figure 3.2b presents the distribution of all monomers of the highly asymmetric $f_- = f_+/16$ chain. As can be observed, the monomers are packing into a cylindrical shape. Comparing Figures 3.3a and 3.3b, the negatively charged monomers are closely packing with the positively charged monomers, however the neutral chain segments are looping up, allowing the ions to associate. This
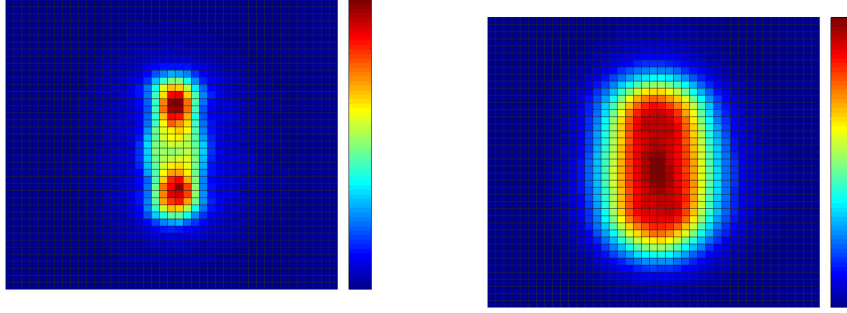
(a) Distribution of $f_- = f_+/16$, $\ell_B/\sigma = 8.0$ (All negatively charged monomers)

(b) Distribution of $f_- = f_+/16$, $\ell_B/\sigma = 8.0$ (All monomers)

Figure 3.3: Visualisation of the distribution of negatively charged monomers (left) and all monomers (right) for the $f_- = f_+/16$ and $\ell_B/\sigma = 8.0$ chains. The ions show close packing whereas the chains as a whole show a cylindrical shape.

leads to a 'bottle brush' conformation.

Radius of Gyration and End to End distance

Figure 3.4 shows the average radius of gyration R_g and average end-to-end distance R_e for the $f_- = 1/2$ symmetric system. Neutral chains, $\ell_B/\sigma = 0.0$, scale $R_e \sim N^\nu$, where $\nu = 0.588$ in a good solvent [38]. At $\ell_B/\sigma < 1$, both blocks swell whilst the chain as a whole collapses, indicating the chain is in the folding regime. As the asymmetricity increases, the positive block swells, however both the negatively charged block and the chains as a whole collapse. Around $\ell_B/\sigma = 1.0$ the system enters a weakly associating regime. Here the symmetric whole chain R_g and block radii of gyration R_g^+, R_g^- are indistinguishable as the chain has collapsed into a globule [12]. There is an increase in swelling for positive blocks with higher asymmetries due to the increased energetic cost of folding the neutral chain segments to allow association of oppositely charged ions. Further increases in the electrostatic interaction strength lead to denser packing for the symmetric chains. For asymmetric chains, we see a transitional behaviour. For
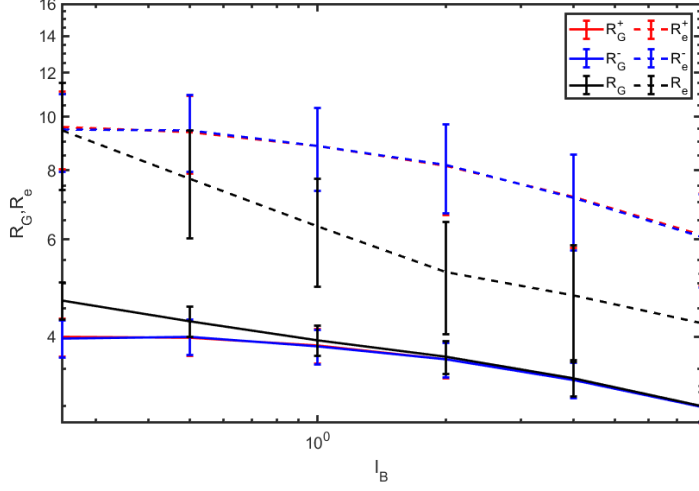
Figure 3.4: Average radius of gyration R_G and end to end distance R_e, $f_- = f_+$, as a function of ℓ_B

low asymmetry, the chains begin to fold as the ions begin to bind. For long enough neutral segments between the negatively charged monomers, the ionic binding does not result in a collapse of the chain into a globular conformation, instead it further swells as the neutral segments are expelled, due to conformational entropy.

A transition in the conformational behaviour is observed at $f_- = 1/8$ in Figure 3.6. With increase of ℓ_B, initially the positively charged block swells, and stays swollen. On the other hand, the negatively charged block can be seen following the globular collapse behaviour. The distance between charges on the negatively charged block means the ions must overcome the entropic penalty to associate with the oppositely charged block. For the oppositely charged monomer to associate with each other it is much easier for the positively charged block to stretch than for the longer block to collapse, and thus the positive block swells. As the electrostatic interaction strength increases, the chain collapses tighter but this is much less pronounced than in the less asymmetric cases. Further increase in the chain asymmetry leads to a shift in the highly

42
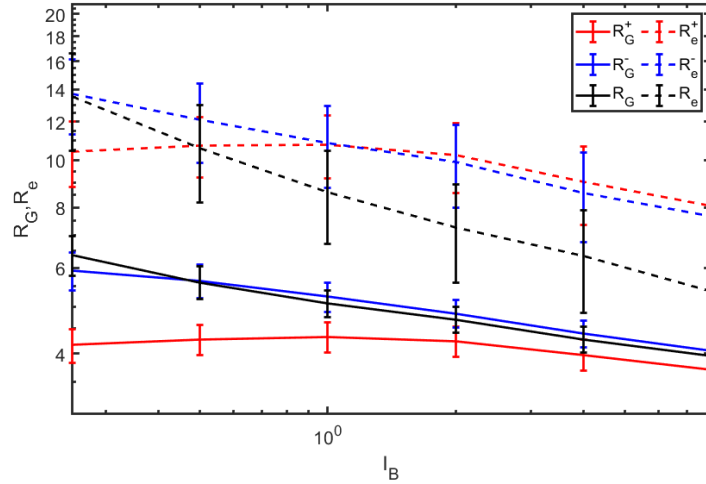
Figure 3.5: Average radius of gyration R_G and end to end distance R_e, for PA chains with $f_- = f_+/2$, as a function of Bjerrum length l_B
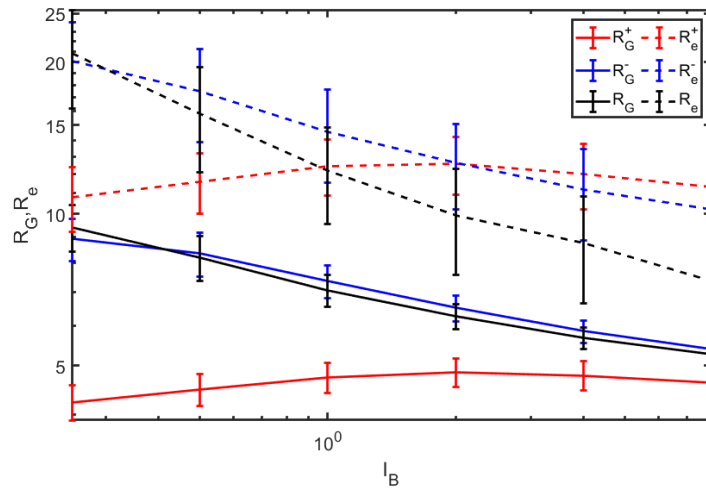
Figure 3.6: Average radius of gyration R_G and end to end distance R_e for PA chains with $f_- = f_+/4$, as a function of ℓ_B

43
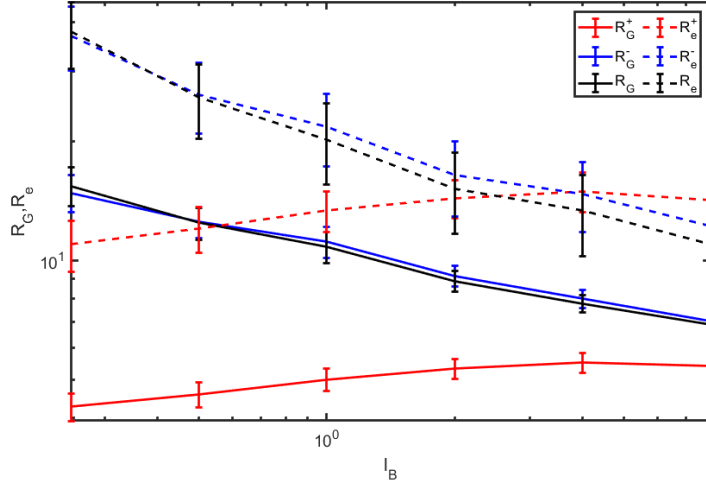
Figure 3.7: Average radius of gyration R_G and end to end distance R_e, $f_- = f_+/8$, as a function of ℓ_B

charged behaviour, as observed in Figure 3.7. Initially, the chain follows neutral chain behaviour. The positively charged block swells and the negatively charged block (and thus the chain as a whole) folds at smaller ℓ_B. However, as ℓ_B increases, the positive block continues to swell, and the collapsing of the oppositely charged block stalls. At this asymmetry the positive block must swell even further such that the negative block overcomes the entropic penalty and begins binding, the neutral segments must loop up as both ends are bonded with the shorter block, forming a bottle brush conformation. It is more important now to switch to discussing the end to end distance of the positive block in these high ℓ_B cases as it is similar to a polyelectrolyte chain stretching with increased intra block repulsion. It is worth also noting that in the strongly associating case, the negatively charged block R_e is also increasing with the electrostatic interaction, implying the presence of a bottle brush. The joint point between two blocks is at one end, and the free ends of the two blocks are near each other on the other end of the bottle brush. As the positive block stretches, thus so does the negative block R_e.

44
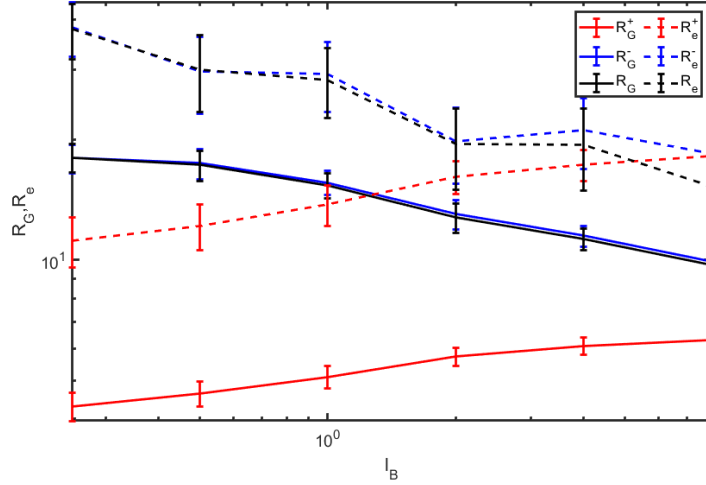
Figure 3.8: Average radius of gyration R_G and end to end distance R_e, $f_- = f_+/16$, as a function of ℓ_B

Figure 3.8 shows R_G and R_e of the highly asymmetric PA chains with $f_- = 1/32$. Here values of R_G for the chain and negative blocks are indistinguishable because the negative block dominates the overall chain conformation due to its shear size. This conformational behaviour is similar to that of the $f_- = 1/16$ case, and we reach the asymmetry limit of conformational behaviour. In the strongly associating, highly asymmetric cases, the average end to end distances $R_e^+ \approx R_e^-$. This seems to imply that the negatively charged monomers are bonded in sequence with the positively charged ones according to their chemical distances from the joint point.

Average Coulomb energy per charged monomer

Figure 3.9 presents the average coulomb energy for a charged monomer. Both positively charged (red) and negatively charged (blue) monomers are present. In symmetric PA chains, the results of both positive and negatively charged monomers are indistinguishable as they behave in the same manner. At small ℓ_B, the attraction between oppositely charged monomers is still weak with no ionic bonding, so the intra block electrostatic
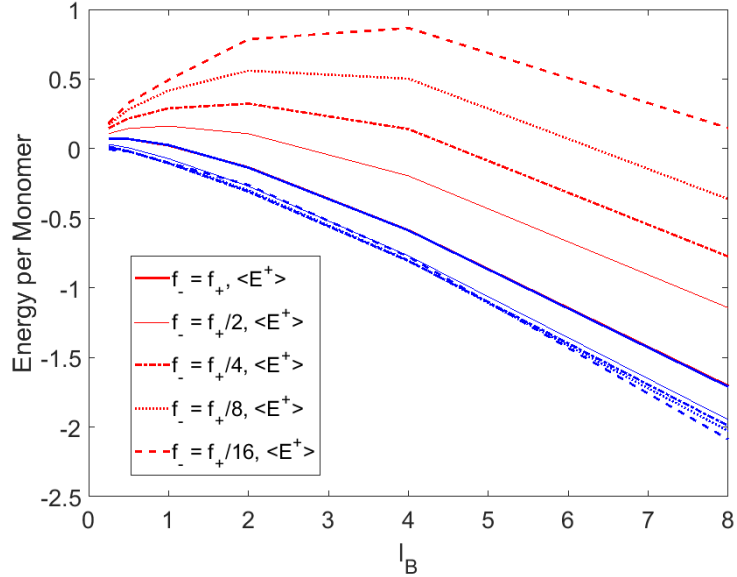
Figure 3.9: Average Coulomb energy per charged monomer, for all systems studied. both the positively charged monomers (red) and their respective negatively charged monomers (blue) are presented.

repulsion energy leads to an overall positive Coulomb energy per charged monomer. As the charge strength increases, the dense packing on ions leads to an overall strong attraction of monomers.

As the asymmetry increases, the energy data profiles of the negatively charged monomers seem to converge.

Shape Describers

Figures 3.10-3.12 present the relative shape anisotropy κ^2 as a function of ℓ_B. If $\kappa^2 = 0$ the monomers of the PA chains are spherically symmetrical, and $\kappa^2 = 1$ when all monomers lie on a straight line. The symmetric case shows an initial elongation over dense packing, as the repulsion of similarly charged ions dominates in these short chains. Then, for systems with low asymmetry and increasing electrostatic interactions strength
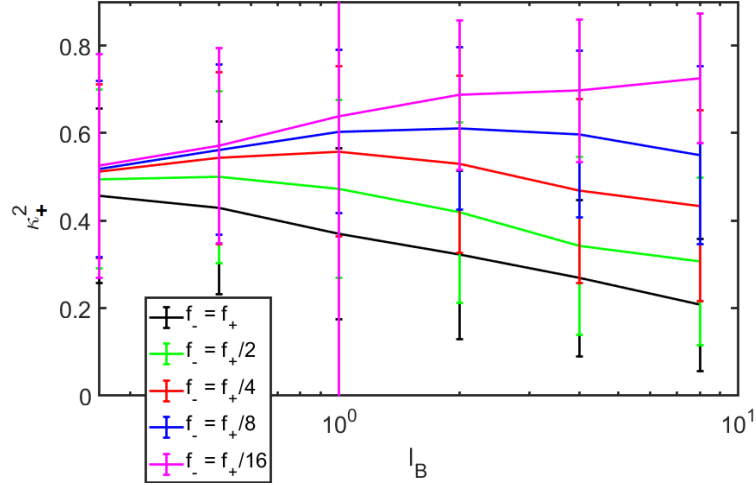
Figure 3.10: Relative shape anistotropy of the positively charged blocks

leads an increase in the sphericity. As the asymmetry increases, so does the chain length, which leads to increasing ashpericity as it requires more energy to overcome entropic penalty and associate with the oppositely charged block. As ℓ_B increases, the whole chain collapses, driven by the association of oppositely charged monomers. For highly asymmetric chains, there is a transition in the conformational behaviour with increasing electrostatic interaction strengths. The whole polymer begins to pack into cylindrical shapes. As the charged overcome the entropic penalty strong charge association takes place, the neutral chain segments in the negatively charged block must loop up to allow close binding of the oppositely charged monomers, which leads to the bottle-brush conformation.

Figure 3.10 presents κ_+^2 for the positively charged blocks. The symmetric system is following the folding and globular pictures, as expected with increasing ℓ_B, reflected in the decrease in κ_+^2. For asymmetric chains, the charge density in the negatively charged block is weak, so the intra-block electrostatic repulsion leads to swelling of the positively charged block at small ℓ_B and consequently an increase in κ_+^2. If the asymme-

47
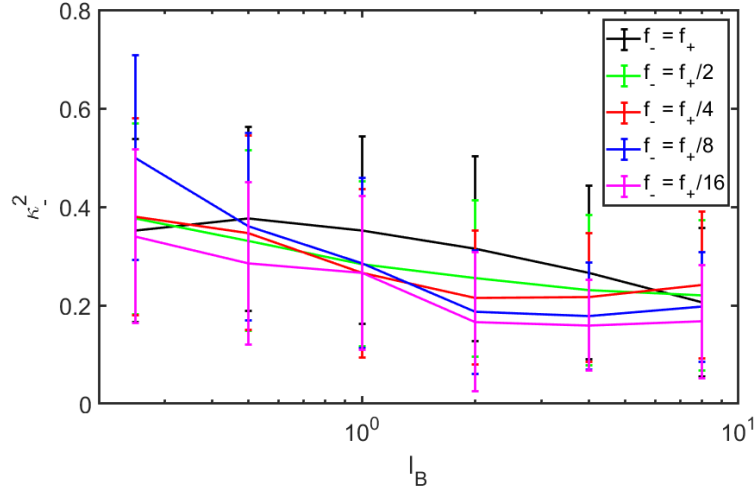
Figure 3.11: Relative shape anisotropy of the negatively charged blocks

try is relatively low, the increasing electrostatic repulsion between oppositely charged monomers lead to the collapse of both blocks and so a decrease in κ_+^2, similar to the symmetric case. But if the asymmetry is high, the positive block needs to stretch out in order to bing with the negatively charged monomers due to the high conformational entropy cost of folding (looping) the longer neutral segments.

Figure 3.11 presents κ_-^2 negatively charged blocks. The differences between the black lines in Figures 3.10 and 3.11 is due to the rotation of the positive block to align with the axis. Whilst the positive block is geometrically restricted by this rotation and shift, the negatively charged block is surrounding, thus the two graphs do not match even though this is a symmetric system. In the symmetric chains κ_-^2 decreases with ℓ_B above a relatively small ℓ_B. For the asymmetric chains, the negatively charged monomers are pulling closer to the positive charges by increasing electrostatic attraction with ℓ_B, leading to a decrease in κ_-^2 initially. But when all the opposite charges have formed ionic bonds along the positive block there is no further space for the negative block to collapse, so κ_-^2 remains nearly constant at high ℓ_B. It is noted that conformations of

48
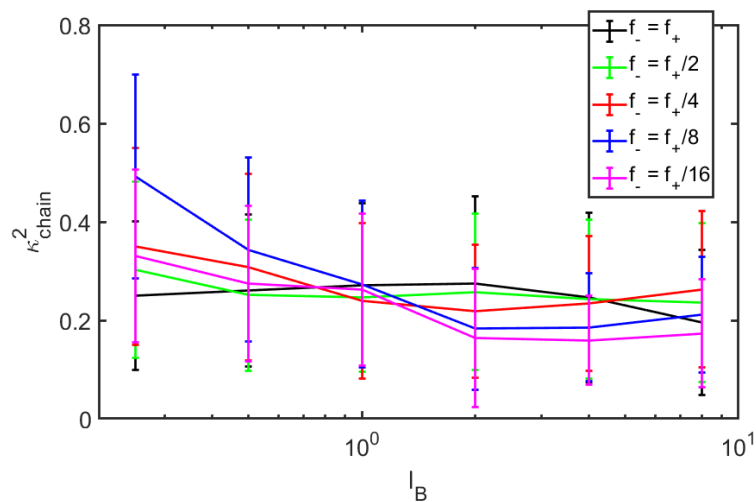
Figure 3.12: Relative shape anistoropy of the whole chains

the neutral segments are playing a dominant role in determining the κ_-^2 values for high asymmetry chains.

Cylindrical Charge distributions

With enough evidence that the asymmetric positively charged blocks are elongating, it is worth looking at the cylindrical distribution of monomers. We rotate and shift the PA chains so that the longest principle axis of the positive block sits along the x axis based on the gyration tensor. Figures 3.13 - 3.17 present charge distributions as a function of their radial distance from the x axis.

In the symmetric case as low ℓ_B, the distributions of different charges should be different with the positive charges closer to the x axis, i.e at smaller r. For increasing electrostatic interaction strength, the negatively charged monomers behave similarly to the positive charges as they start to bing tighter and tighter. As the asymmetry is increased, we see a wider distribution in the negatively charged monomers, as neutral chain segment behaviour dominates.
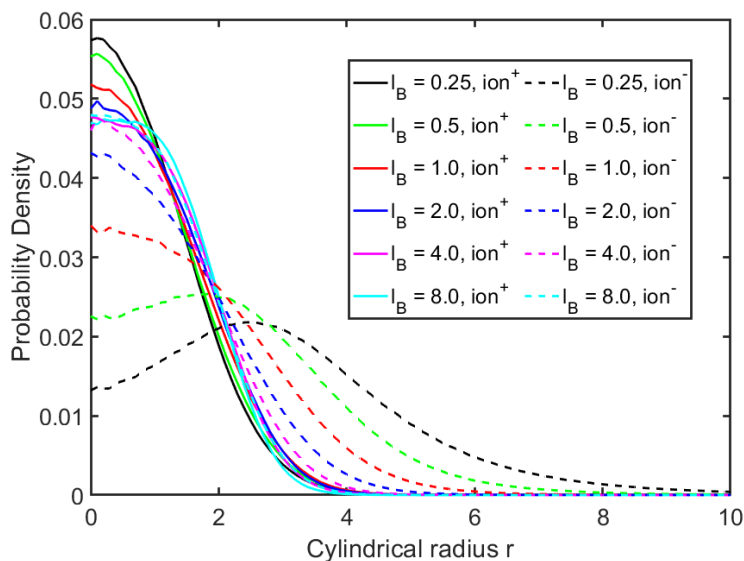
Figure 3.13: Radial distribution of charged monomers relative to the principle axis of the positively charged block for the symmetric $f_- = f_+$ chain

At higher ℓ_B values, we see distributions of negatively charged monomers again showing that they have overcome the conformational entropic penalty of the neutral chains.

Also presented in the 3.17 are the distributions of all monomers on the negatively charged block. This shows that at low electrostatic interaction strengths the negative charged monomer distribution is dominated by the neutral chain behaviour, and at high ℓ_B values the charged monomers are behaving wildly different from the chain as a whole, again pointing out the bottle brush conformation due to ionic binding.

Radial Energy Profiles

Figures 3.18 - 3.22 present the Coulombic energy per charged monomer as a function of their radial distance to the principal axis of the positively charged block. These energy profiles provide further evidence of the above mentions conformational transitions as a
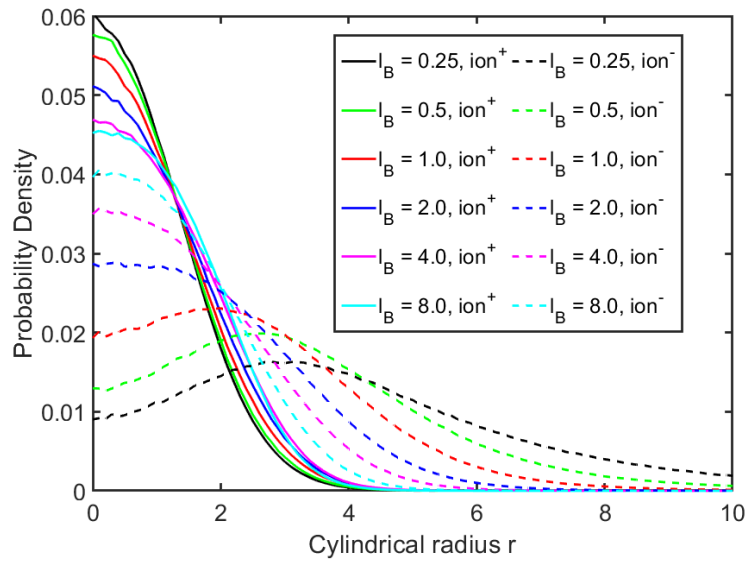
Figure 3.14: Radial distribution of charged monomers relative to the principle axis of the positively charged block for the asymmetric $f_- = f_+/2$ chains
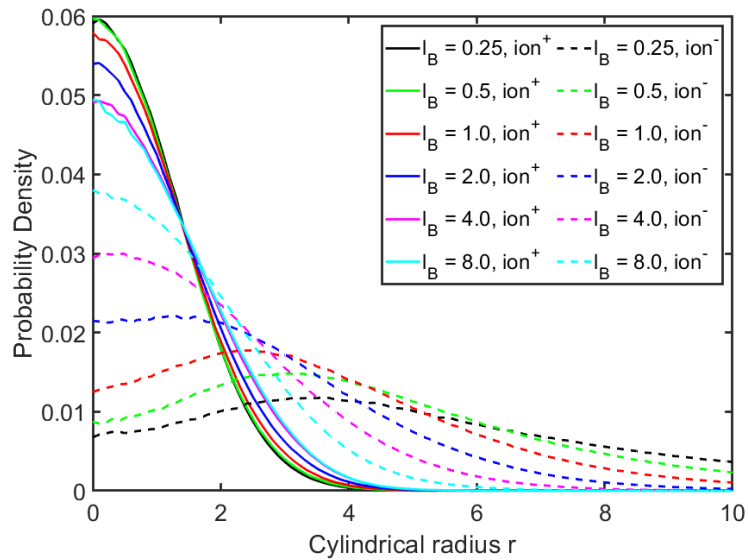
Figure 3.15: Radial distribution of charged monomers relative to the principle axis of the positively charged block for the asymmetric $f_- = f_+/4$ chains
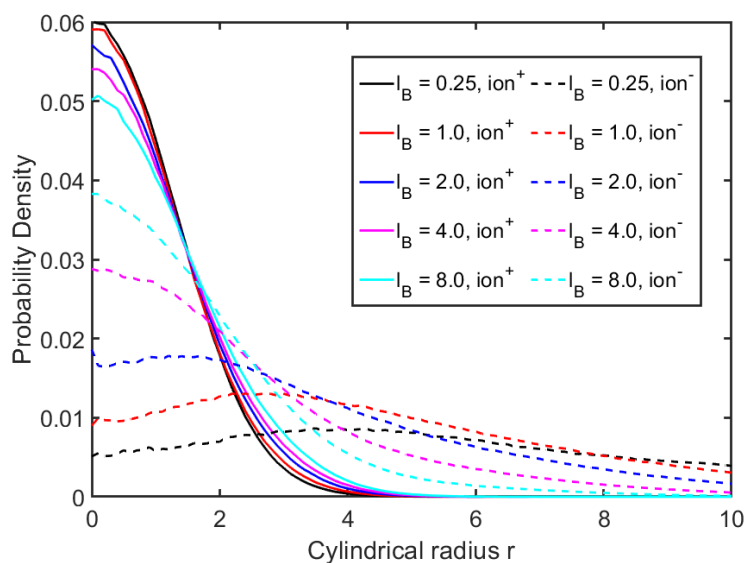
Figure 3.16: Radial distribution of charged monomers relative to the principle axis of the positively charged block for the asymmetric $f_- = f_+/8$ chains
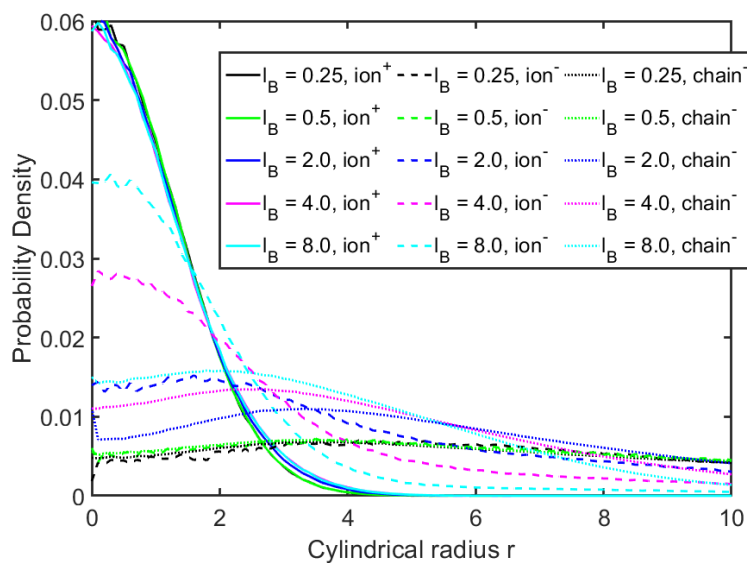
Figure 3.17: Radial distribution of charged monomers relative to the principle axis of the positively charged block for the asymmetric $f_- = f_+/16$ chains

52
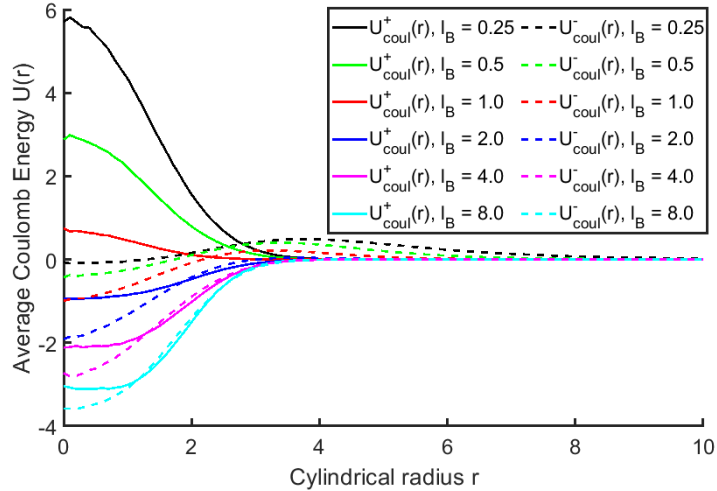
Figure 3.18: Radial Energy profile of charged monomers relative to the principle axis of the positively charged block for the symmetric $f_- = f_+$ chains

function of electrostatic interaction strength and chain asymmetry, namely the folding, to globular and bottle brush transitions.

The radial energy profiles highlight the barrier transition in the chain boundary shifting with increased chain length.

3.2.3 Conclusion

In the absence of charge, the diblock chains with $N_- f_- = N_+ f_+$ would behave as neutral polymers of length $N = N_+ + N_-$. As the electrostatic interaction strength is increased, the chain conformation transition from folding to coil, then to weakly and finally strongly associating state [12]. An asymmetric increase in neutral chain segment lengths on the negatively charged block yields a swelling in the positively charged block at increasing electrostatic interaction strengths. It requires higher attraction energy to fold the negatively charged ions. As the electrostatic interaction strength increases above the entropic barrier, more negatively charged monomers are able to bind with the oppositely charged block. For small asymmetries this yields a folding of the two

Figure 3.19: Radial Energy profile of charged monomers relative to the principle axis of the positively charged block for the asymmetric $f_- = f_+/2$ chains
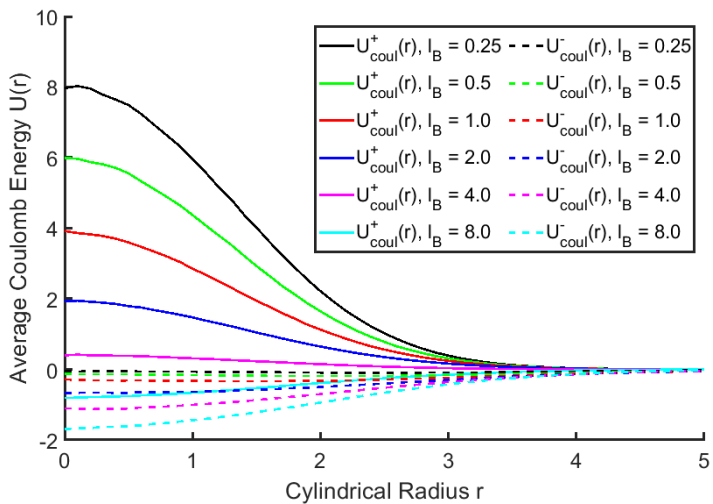
Figure 3.20: Radial Energy profile of charged monomers relative to the principle axis of the positively charged block for the asymmetric $f_- = f_+/4$ chains
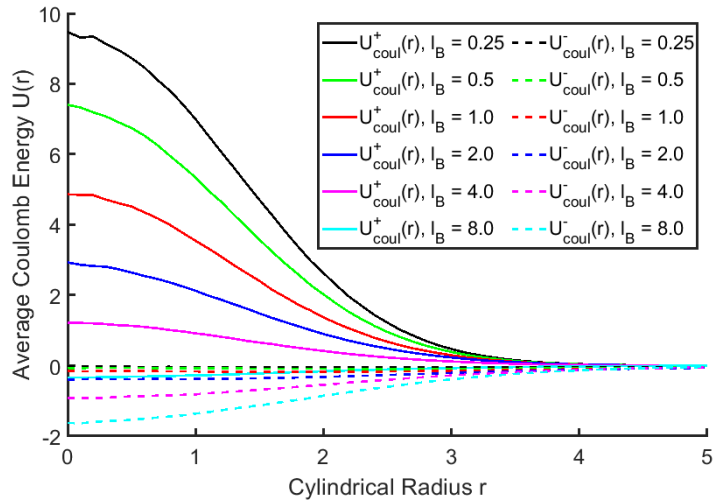
Figure 3.21: Radial Energy profile of charged monomers relative to the principle axis of the positively charged block for the asymmetric $f_- = f_+/8$ chains
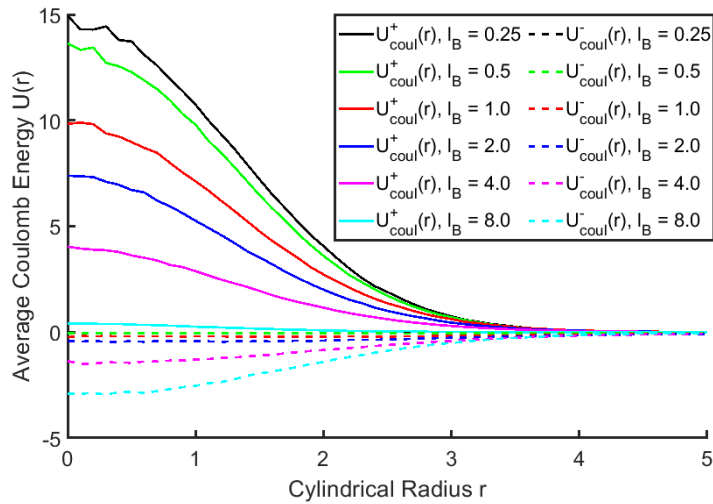
Figure 3.22: Radial Energy profile of charged monomers relative to the principle axis of the positively charged block for the asymmetric $f_- = f_+/16$ chains

individual blocks into a globule, however chains with longer neutral segments on the negatively charged block cause a further extension of the positively charged block and looping of the neutral segments of the other block due to ionic binding, such that they take a bottle brush conformation.

3.3 Asymmetric Diblock Polyampholytes carrying net charge, $N_- \geq N_+$, $f_- = f_+$

3.3.1 Introduction

In this section we focus on diblock PA chains with degree of polymerisation $N = N_+ + N_-$ and identical charge fractions $f = f_- = f_+$, the net charge of the system is defined by

$$eZ_{\text{net}} = e\Delta Nf, \tag{3.1}$$

where $\Delta N = N_- - N_+$. If the system is charge symmetric, PA chains behave as discussed in the literature [12, 13], in which they collapse into a globule, driven by the charge density fluctuation induced attraction of oppositely charged monomers [47, 13]. For low asymmetries the chains follow dense packing of electrostatic blobs [13], giving the chain size

$$R_{\text{gl}} \approx \xi_e \left(\frac{N}{g_e} \right)^{1/3} \approx \sigma N^{1/3} \left(\frac{\ell_B f^2}{\sigma} \right)^{(1-3\nu)/3(2-\nu)}. \tag{3.2}$$

In the limit of high asymmetry $N \approx N_- >> N_+$, the contribution from the shorter block to the overall behaviour can be considered negligible and the chain is effectively equivalent to a polyelectrolyte [13, 17]. Shusharina et al [13] developed scaling theory for diblock polyampholytes in salt free solutions. They predicted that in the intermediate

asymmetry regime, a chain should collapse into a tadpole shape with a globular head of size R_{head} and a polyelectrolyte tail of length R_{tail}. In their prediction, whether a monomer is in the tail or head is determined by the balancing of charge density induced attraction against the repulsive energy of bringing another charge into the head, leading to

$$\frac{\ell_B Z_{\text{head}}}{R_{\text{head}}} \approx \frac{\ell_B Z_{\text{tail}}}{R_{\text{tail}}} \tag{3.3}$$

where eZ_{head} and eZ_{tail} are the net charges of the head and tail respectively. However, over a wide range of ℓ_B and chain asymmetries, we do not see tadpole as the most favourable conformation. Instead, single chains deform and stretch to associate with more oppositely charged monomers, whilst simultaneously reducing the intra-block electrostatic repulsions. In the limit of high electrostatic interaction strength, the polymers adopt a helical/ PE core conformation. Above a critical asymmetry, the excess charges are sent out in the form of a tail, leading to a cigar-like helix/PE core head with polyelectrolyte tail.

3.3.2   Models and Methods

We simulate diblock PA chains with $N_+ = 128$, $f_- = f_+ = 1/2$ at $\ell_B = \{0.5, 1.0, 2.0, 4.0\}\,\sigma$. The lengths of the negatively charged blocks range from $N_- = 128$ to 416 in increments of 8. In these cases, counterions are required to satisfy the electro-neutrality of the system and thus PBC are required [36]. We also define relative charge asymmetry $N_{\text{excess}} = \Delta N/N_+$, as an important feature relating to the asymmetry. We are interested in polymers in a good solvent and thus take the LJ parameters $\epsilon_{\text{LJ}} = 1.0$ and $r_{\text{cut}} = 2^{1/6}\sigma$. For the FENE coefficients we choose $k_{\text{FENE}} = 7.0$ and $R_{\text{FENE}} = 2.0$ to be consistent with the literature [12]. Lastly, the step size is $dt = 0.001$, the temperature $T = 1$, monomer density $\rho = 1 \times 10^{-3}$ and friction constant $\zeta = 1$
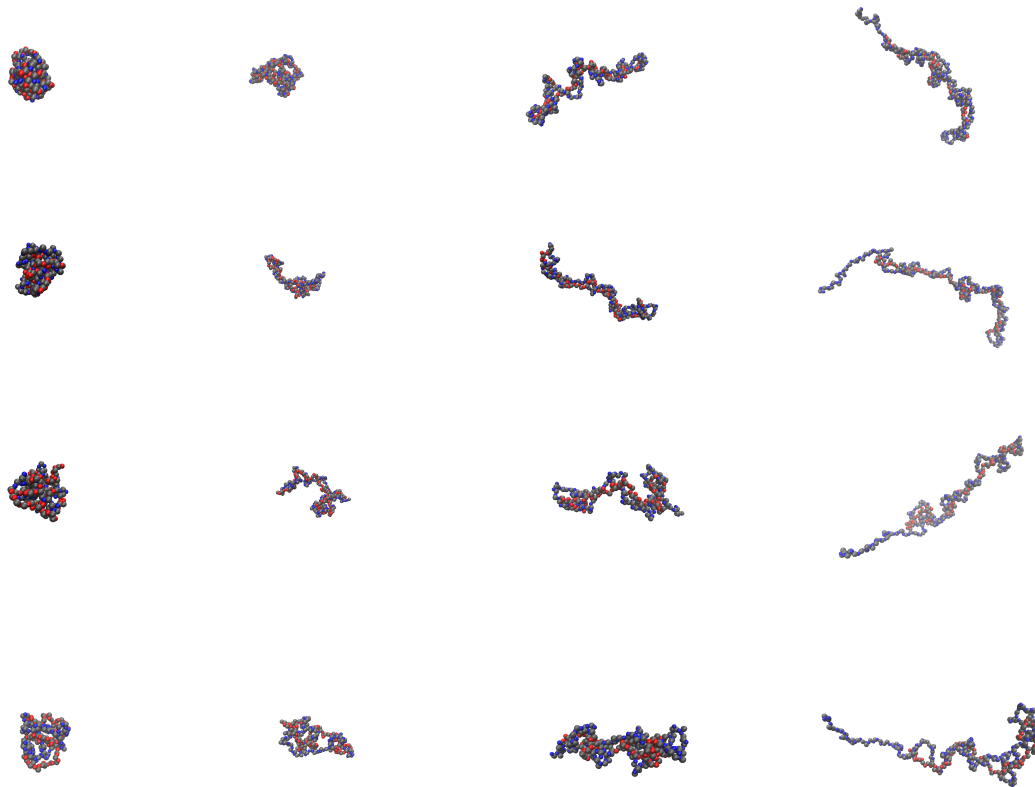
Figure 3.23: Snapshot visualisations of chains, from bottom to top, $\ell_B = \{0.5, 1.0, 2.0, 4.0\}\sigma$. From left to right, $N = 252$, $N = 288$, $N = 320$, $N = 384$. $N_+ = 128$, $f = 1/2$

3.3.3   Results

Visualisation

Figure 3.23 shows snapshots of sample configurations of four different systems. Symmetric diblock PAs form globulars due to the electrostatic attraction. As the asymmetry increases, the globules start to take a more elongated shape. Above a critical asymmetry, the chain becomes an oblong, consisting of a positive central line with the negative block wrapping around. In the extreme case, a very stretched central line and increas-
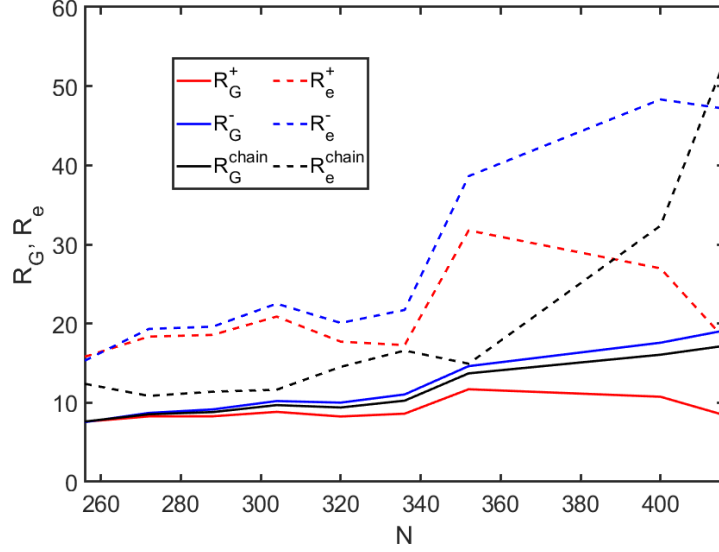
Figure 3.24: Average Radius of Gyration R_G and end to end distance R_e of the individual components with respect to N for $\ell_B = 0.5\sigma$

ingly tight wrapping with a tail pointing out carrying part of the excess charges. This elongated head structure is clearly different from the tadpole structure with spherical head theoretically predicted [13].

Radius of Gyration and End to End Distance

Figures 3.24 -3.27 show the average Radius of Gyration R_G and end to end distance R_e of the individual components for $\ell_B = \{0.5, 1.0, 2.0, 4.0\}\sigma$ respectively for various chain asymmetries. In all instances, the positively charged block continues to stretch until reaching a plateau. The chains start to send part of the additional charges out as a PE tail at around $N = 320$, corresponding to $N_{\text{excess}} = 0.5$. For low asymmetry, the chains take globular conformations as predicted by Shusharina and follow the picture of dense packing of oppositely charged blobs. However this behaviour quickly changes. At intermediate charge asymmetries, instead of favouring the conformation of a globular head with a polyelectrolyte tail, the head stretches to become a net-charged oblong.
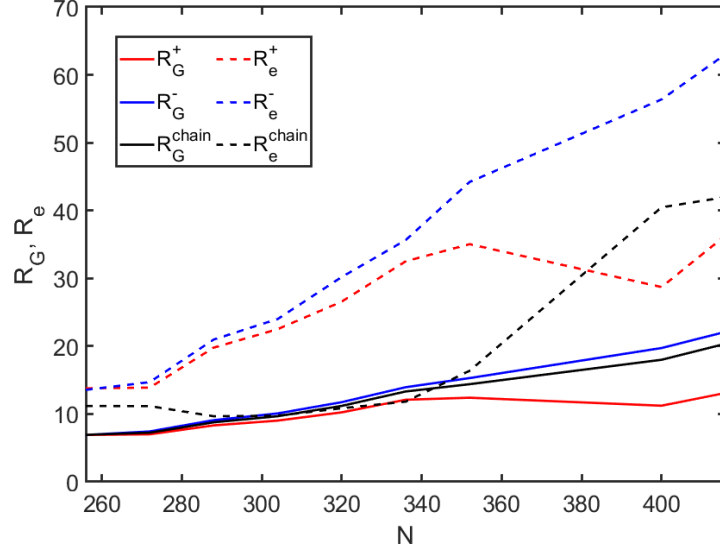
Figure 3.25: Average Radius of Gyration R_G and end to end distance R_e of the individual components with respect to N for $\ell_B = 1.0\sigma$

As the asymmetry increases, it is further stretched until the head is like a positively charged polyelectrolyte core with the longer chain wrapping around. Thus, in the highly asymmetric case, we view this as a cigar like head with helix/PE core structure with a polyelectrolyte tail carrying part of the excess charges.

Head and Tail Conformation Analysis

For characterising the conformation of asymmetric diblock PA chains according to the tadpole picture, we define the PE tail sticking out of the head as the part of the negatively charged block where the charged monomers have no positively charged neighbours. We define two monomers are neighbours if their centres of mass are within a distance r_{neigh} Results are sensitive to choice of this value, but we aim to provide qualitatively coherent results, and chose $r_{\text{neigh}} < 1.5$. Figure 3.28 shows the comparison between the simulation data and theoretical prediction, for the number of net charges Z_{head} in the head, for all ℓ_B studied. The net valence of the head in the tadpole regime
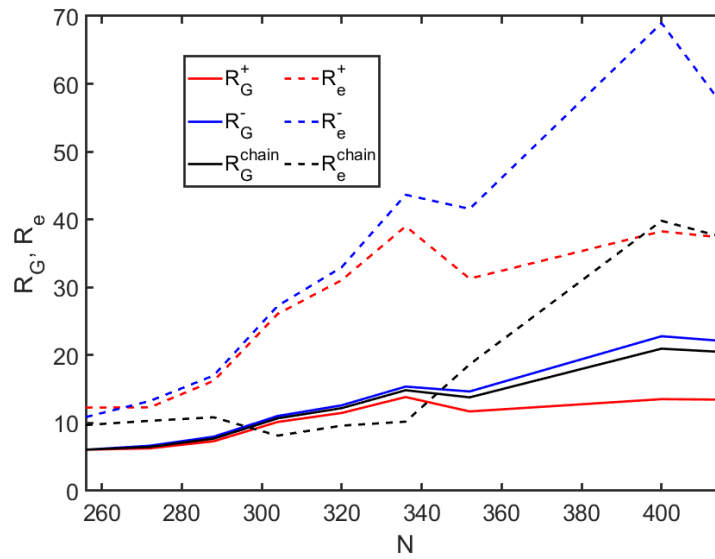
Figure 3.26: Average Radius of Gyration R_G and end to end distance R_e of the individual components with respect to N for $\ell_B = 2.0\sigma$
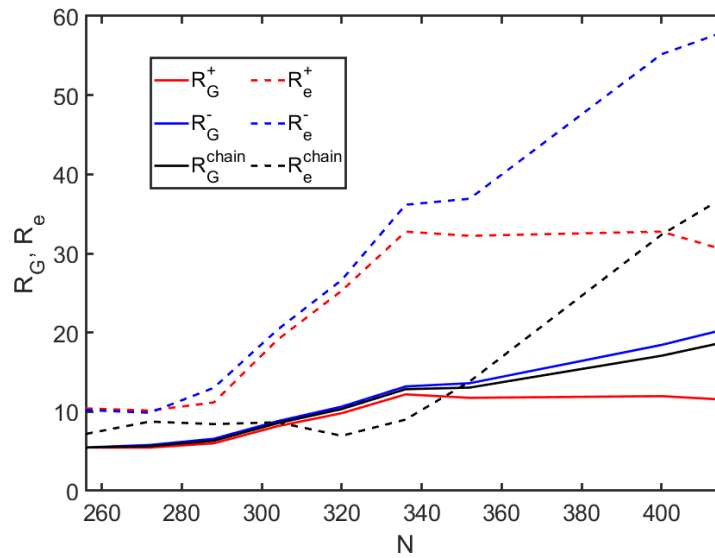
Figure 3.27: Average Radius of Gyration R_G and end to end distance R_e of the individual components with respect to N for $\ell_B = 4.0\sigma$
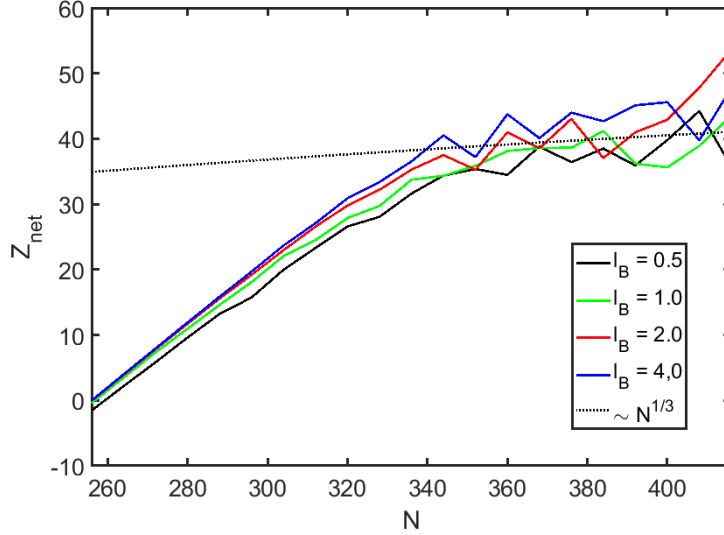
Figure 3.28: Net charge of the head Z_{head}. The dashed line is the theoretical prediction of equation 3.4, subject to a vertical shift.

is predicted for $\Delta N/N << 1$ [13]

$$Z_{\text{head}} \approx N^{1/3} f(uf^2)^{-4/9} \tag{3.4}$$

For small asymmetries, the net charge of the head grows linearly, as all charges are incorporated in the head. A universal transition from globular or cigar to head-tail or cigar tadpole conformation takes place at a certain charge asymmetry, regardless of ℓ_B. In the range of chain length were head to tail conformation is formed, this scaling behaviour seems to be followed, but it is noted that the theoretically predicted variation in Z_{head} over the N range we studied is very small, thus not much different from a constant.

Figure 3.29 presents the size of the head (R_G) and the size of the tail (R_e). In Shusharina et al's picture, the crossover from globule to head occurs when $R_{\text{head}} \approx R_{\text{tail}}$ [13]. The cross over of R_{head} and and R_{tail} can be seen in figure 3.29 in the range of
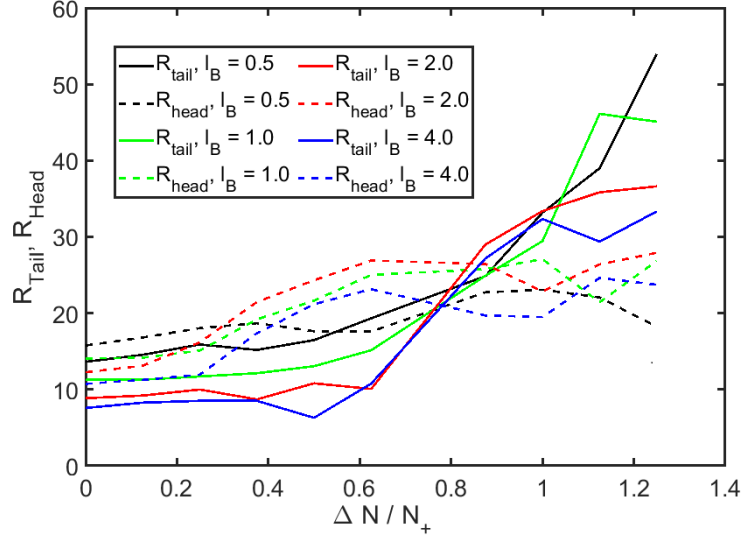
Figure 3.29: R_{head}, Radius of gyration (R_G) and R_{tail} end to end distance (R_e).

$\Delta N/N_+ \approx 0.5 \sim 0.8$, but the identification of the exact crossing point is subject to the definitions of head and tails, their sizes R_{head} and R_{tail} and the statistics of the data.

Figures 3.30 - 3.33 present the average radii of gyration and end-to-end distances for the PA chains as a function of $\Delta N/N_+$, for each ℓ_B. Shusharina et al predicted that the length of the tail scales [13]

$$R_{\text{tail}} \approx b\Delta N(uf^2)^{1/3}. \tag{3.5}$$

This $R_e^{\text{tail}} \sim N$ scaling behaviour can be qualitatively observed in our simulation results for the highly asymmetric systems, after the onset of the head-tail conformation regime.
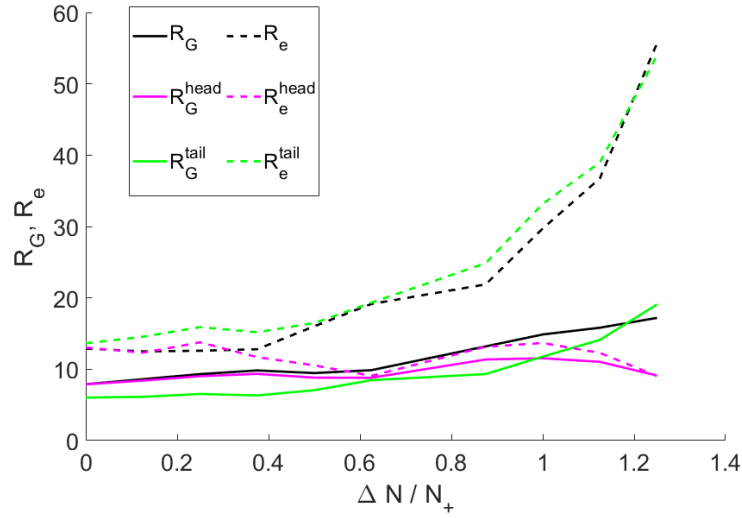
Figure 3.30: Average Radius of Gyration R_G and end to end distance R_e of the individual components, namely head, tail and entire chain, for diblock PAs at $\ell_B = 0.5\sigma$
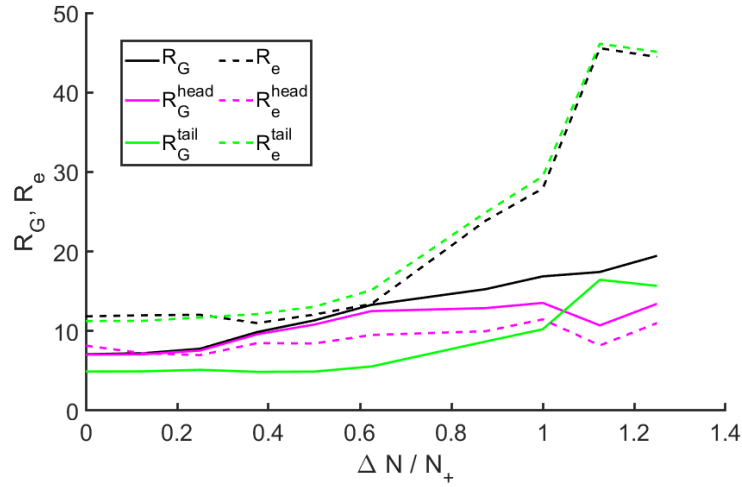
Figure 3.31: Average Radius of Gyration R_G and end to end distance R_e of the individual components, namely head, tail and entire chain, for diblock PAs at $\ell_B = 1.0\sigma$
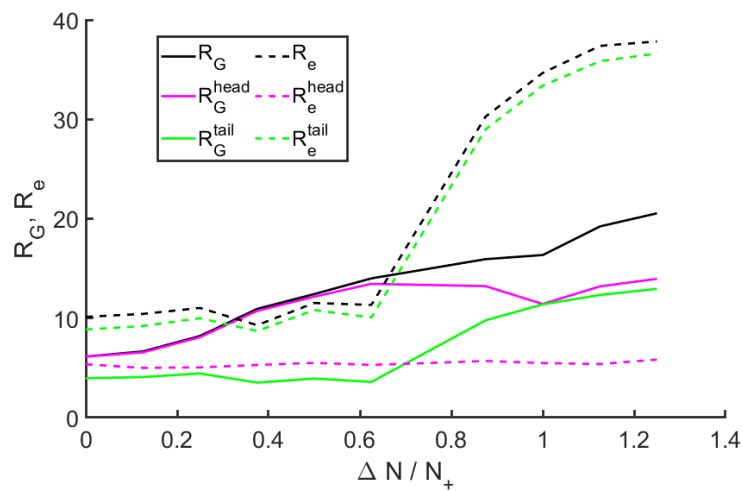
Figure 3.32: Average Radius of Gyration R_G and end to end distance R_e of the individual components, namely head, tail and entire chain, for diblock PAs at $\ell_B = 2.0\sigma$
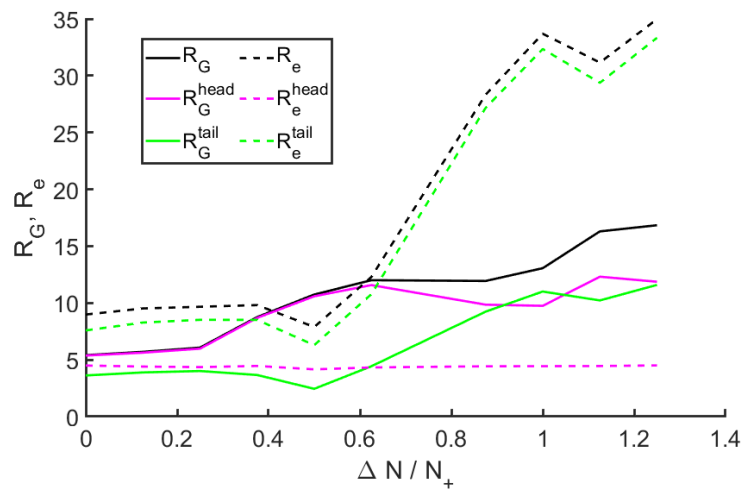
Figure 3.33: Average Radius of Gyration R_G and end to end distance R_e of the individual components, namely head, tail and entire chain, for diblock PAs at $\ell_B = 4.0\sigma$
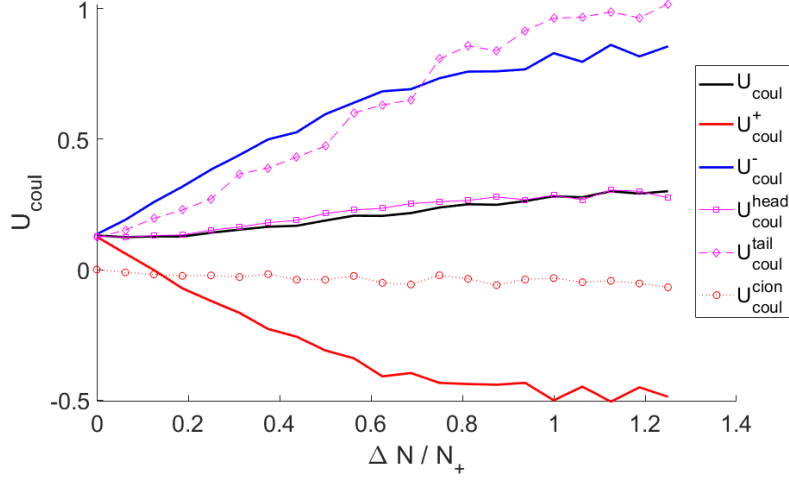
Figure 3.34: Average energy experienced per ion, $\ell_B = 0.5\sigma$

Average Coulomb Energy per charged monomer

Figures 3.34 - 3.37 show the average Coulomb energy per ion as a function of relative charge asymmetry $N_{\text{excess}} = \Delta N/N_+$, each figure corresponds to a different electrostatic interaction strength. Figures 3.38 - 3.41 show the Coulomb energy per charged monomer for four sample systems as a function of ℓ_B. The results are shown for individual components of the chains As the asymmetry increases, the total Coulomb energy experienced by the positively charged monomers U_{coul}^+ is negative with its magnitude increases due to the increased number of negatively charged monomers associating with them. On the contrary, the energy U_{coul}^- experienced by the negatively charged monomers is positive with its magnitude, increases due to the increased repulsion among themselves. It can also be observed that the average Coulomb energy per charged monomer inside the head follows similar behaviour as that of all charged monomers in the system, showing that the behaviour of the system is largely dominated by the head. In the highly charged case, a PE tail sticking out which can attract and condense the counterions.

66
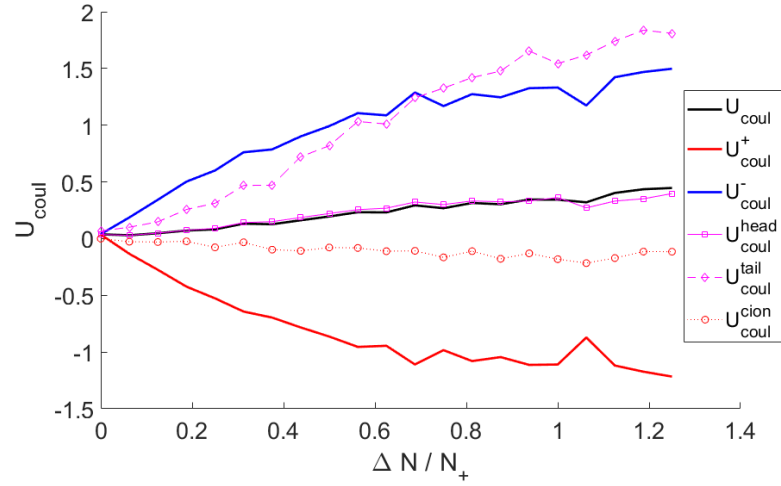
Figure 3.35: Average energy experienced per ion, $\ell_B = 1.0\sigma$
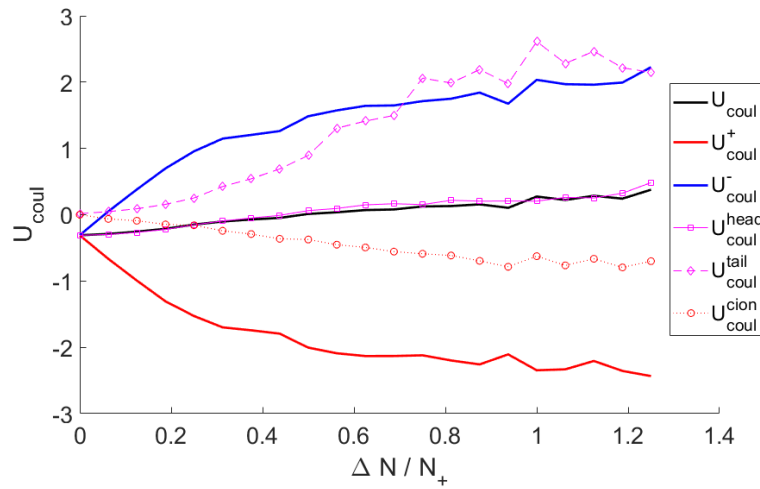
Figure 3.36: Average energy experienced per ion, $\ell_B = 2.0\sigma$

67
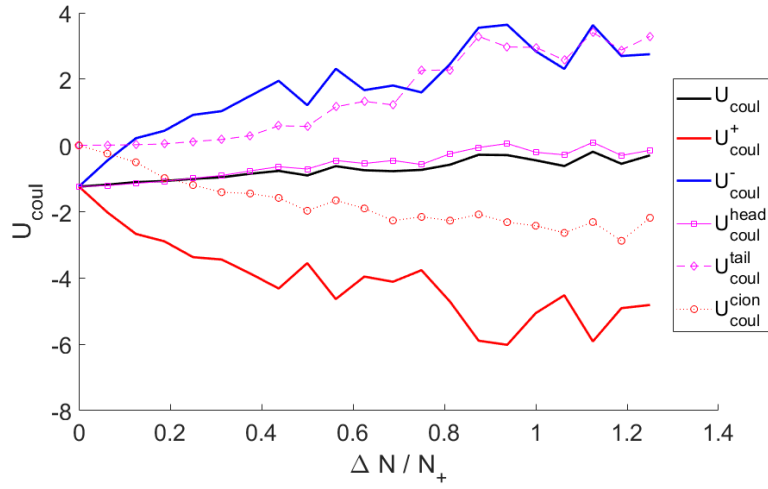
Figure 3.37: Average energy experienced per ion, $\ell_B = 4.0\sigma$
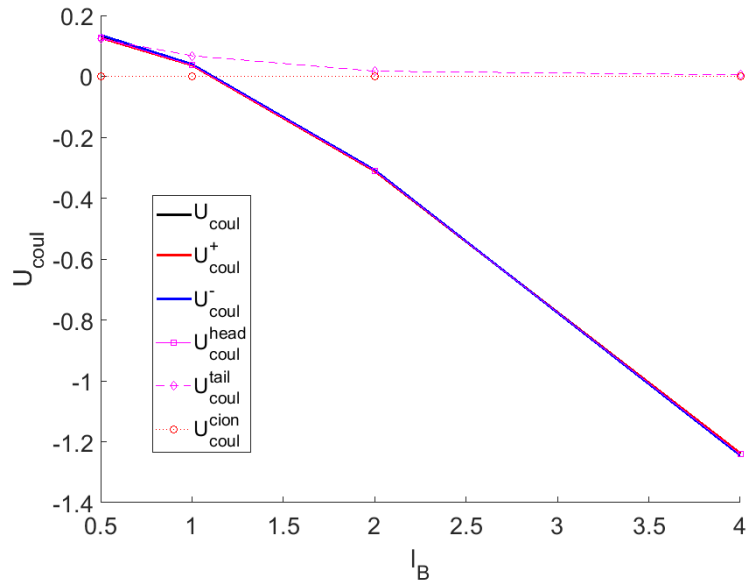
Figure 3.38: Average Coulomb energy experienced per ion $N = 256$

68
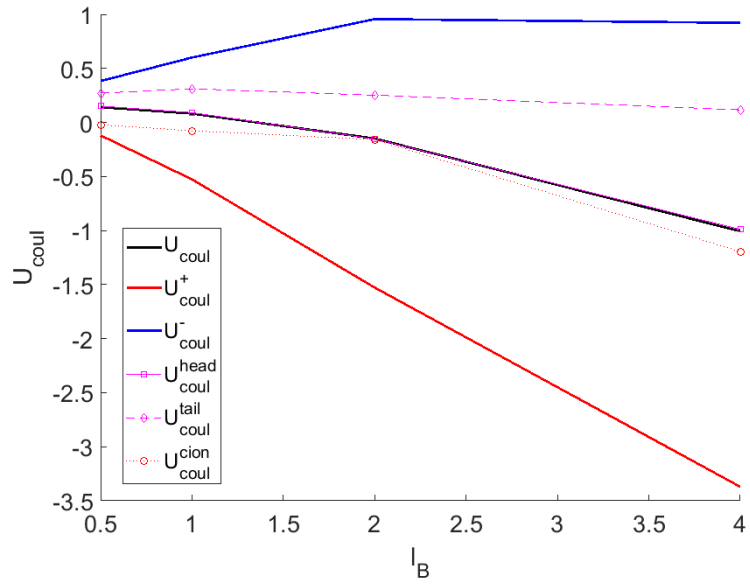
Figure 3.39: Average Coulomb energy experienced per ion $N = 288$
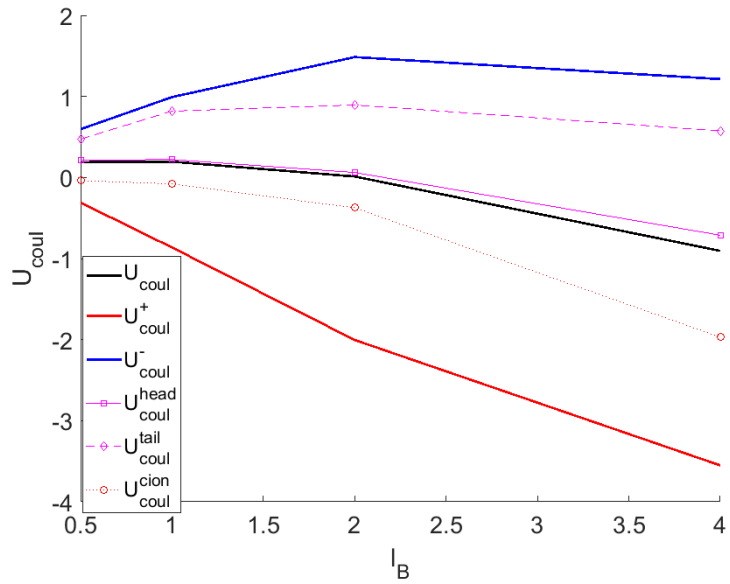
Figure 3.40: Average Coulomb energy experienced per ion $N = 320$

69
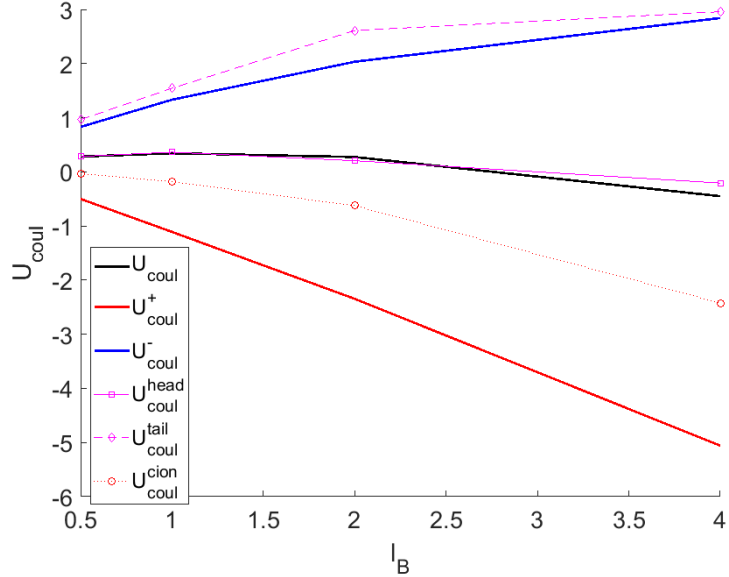
Figure 3.41: Average Coulomb energy experienced per ion $N = 384$

3.4   Conclusions

Please note that the results in this section are subject to noise, and require further data. However, we show that symmetric diblock PA chains form globules, consistent with the work of Wang and Rubinstein [12]. With increasing charge asymmetry the globule starts to elongate into cigar-like shapes. If the electrostatic interaction strength is high it can extend into into a helix/ PE core structure with the longer block wrapping around the shorter one. Although infrequent, low symmetric chains at low ℓ_B are able to adopt the helical structure, see figure 3.42. The two oppositely charged blocks scramble together until $N_- \approx 1.5N_+$. A further increase in charge asymmetry leads to a PE tail sticking out carrying part of the excess charges. The chain conformation thus turns into a tadpole-like shape consisting of a cigar-like head carrying excess charge, and a polyelectrolyte tail containing the rest of the charges. This conformational transition is qualitatively consistent with the theoretical predictions of Shusharina et al [13], however the theory didn't consider the elongation of the head. It is worth noting that our

70
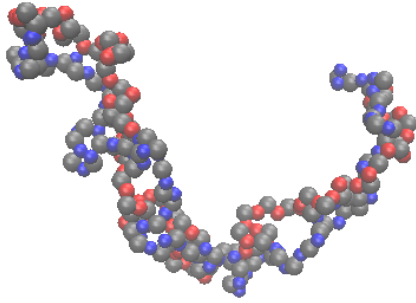
Figure 3.42: Snapshot of a symmetric chain of length $N = 256$ adopting an infrequent helical structure at $\ell_B = 0.5\sigma$

results are relevant to a good solvent, whereas the theory relates to θ solvent. Further theoretical work is still needed for describing our simulation results.

Chapter 4

Self-Assembly Behaviour of Asymmetric Diblock Polyampholytes

4.1   Interactions between two asymmetric PA chains

4.1.1   Introduction

To understand the underlying mechanisms in the aggregation behaviour of charged polymers, it is imperative to analyse the interactions between two such chains. Symmetric diblock polyampholytes continue to aggregate with increasing number of chains and form a dense sediment [13]. For the asymmetric PA chains, such as those with $f = f_+ = f_-$ and $N_- > N_+$, the fluctuation induced electrostatic attractions between the oppositely charged blocks irrespective of which polymer they belong to, brings the chains together. The aggregation of the chains can reduce the surface energy per chain, which can counter-balance the electrostatic repulsion energy caused by the net charge of

72

the aggregate [13]. But the size of the aggregate is limited by the net charge carried by each chain, eZ_{net}. Thus, micelles are predicted to form when the surface energy gain in the head is larger than the electrostatic energy of the tail [13], i.e., when $Z_{\text{net}} < Z_{\text{unimer}}$

$$Z_{\text{unimer}} \approx N f \left(\frac{N_{\text{neutr}}}{N} \right)^{1/3},$$

(4.1)

where

$$N_{\text{neutr}} = (l_B f / \sigma)^{-2/3}$$

(4.2)

which is the length of a diblock PA chain whose size is comparable to one electrostatic blob. It is worth noting that for simulation it is more convenient to discuss the behaviour in terms of the bead size; the Kuhn length b is proportional to the Lennard Jones diameter σ, a fully extended bead spring polymer has length $L = Nb \approx N\sigma$ If $Z_{\text{net}} > Z_{\text{unimer}}$ the chains prefer to stay as individual unimers (single chains), as the cost of bringing these excess repulsive charges together outweighs the benefits of reducing the surface energy.

In this chapter we present our MD simulation results on the association behaviour of asymmetric diblock PA chains by investigating the stability of the preassembled 2-chain and 16-chain aggregates. The umbrella sampling method is used to calculate the effective interaction potential, or potential of mean force, between two asymmetric chains for understanding the driving force for their association or repulsion. A relatively wide range of chain length, asymmetric and electrostatic interaction strengths is covered.

4.1.2 Models and Simulation Methods

We study diblock PA chains with fixed positive block length of $N_+ = 128$ and various negative block lengths $N_- = \{128, 144, 160, 188, 192, 256\}$. The charge fractions

are fixed to $f_- = f_+ = 1/2$. The polymers are considered to be in a good solvent and thus we take the LJ parameters $\epsilon_{\mathrm{LJ}} = 1.0 k_B T$ and $r_{\mathrm{cut}} = 2^{1/6}\sigma$. For the FENE parameters we choose $k_{\mathrm{FENE}} = 7.0 k_B T/\sigma^2$ and $R_{\mathrm{FENE}} = 2.0\sigma$ as before. The Bjerrum length is increased from $\ell_B/\sigma = 1/8, 1/4$ to 4 by an increment factor of 2. The Langevin equations of motion of the monomers and counterions are integrated with the velocity Verlet method with time step size $dt = 10^{-3}\tau_{\mathrm{LJ}}$. MD simulations of the association/dissociation behaviour of PA chains are performed with periodic boundary conditions with the electrostatic interactions handled by the P3M method. The number density of particles (monomers and counterions) is taken to be $\rho = 10^{-3}\sigma^{-3}$.

We first allow $N_{\mathrm{poly}} = 2$ neutral chains of length $N = N_+ + N_-$ to relax freely, then drag them together with an artificial harmonic force between the centres of mass. This force is introduced for preassembling the PA chains into aggregate, because it is computationally impractical to simulate micellization process starting from solutions of randomly distributed chains. The neutral chains continue to relax whilst still being pulled together. The charges are then turned on, and after a further 10^7 time steps we turn off the drag force and continue with the standard MD simulations. Whilst the behaviour after the switch-off may be unrepresentative of a real system, it allows us to investigate the stability of the aggregates and the length of time for reaching possible equilibrium state.

There is an issue when using only a single starting position in which we have limited sampling. Most systems has a single starting position, however the $N = 272$ simulations were performed from five starting configurations to help improve the statistics.

The interaction energy between two PA chains is calculated using the umbrella

sampling method where we simulate $N_w = 20$ sufficiently overlapping windows in each case. We employ a harmonic spring with spring constant $k = N^{-1/3} k_B T / \sigma^2$, which is related to the radius of gyration of a collapsed single-chain globule [49]. Periodic boundary conditions with P3M are still used, but the number density of particles is taken to be $\rho = 10^{-7} \sigma^{-3}$ such that the periodic images of the PA chains play very minor role in any simulated window. The low density will have some quantitative, but no qualitative, effect on the counterion condensation behaviour, as will be demonstrated below for the systems simulated using the standard MD method. No REMD is used for the umbrella sampling, although Ito et al. [107] presented a method for replica exchange umbrella sampling (REUS), in which the umbrella windows are swapped with particular attention paid to ensuring sufficient overlap of the replicas based on test simulations. Our PA chains can be much longer than the PN molecules they studied.

4.1.3 Simulation results and discussions

Standard MD simulations of preassembled aggregates

Figure 4.1 presents the snapshots of the two asymmetric PA chain systems, each obtained from standard MD simulation at $t = 10^5 \tau_{\mathrm{LJ}}$ after turning off the drag force between their centres of mass. At Bjerrum lengths $\ell_B / \sigma \leq 1$, the two PA chains show a general repulsion behaviour, regardless of the chain asymmetry. According to the theoretical calculations of Shusharina et al. the net charge $Z_{\mathrm{net}} = 8$ for the PA chains with length $N = 272$ is smaller than the critical value of Z_{unimer} (≈ 21) at $\ell_B / \sigma = 1$, and so these chains are predicted to aggregate to form micelles. However the pairs of chains do not show a stable association state in our simulations. At higher ℓ_B values, the PA chains with low asymmetry can be trapped in the meta-stable preassembled aggregate state due to the strong electrostatic attraction. The aggregate of the two chains with
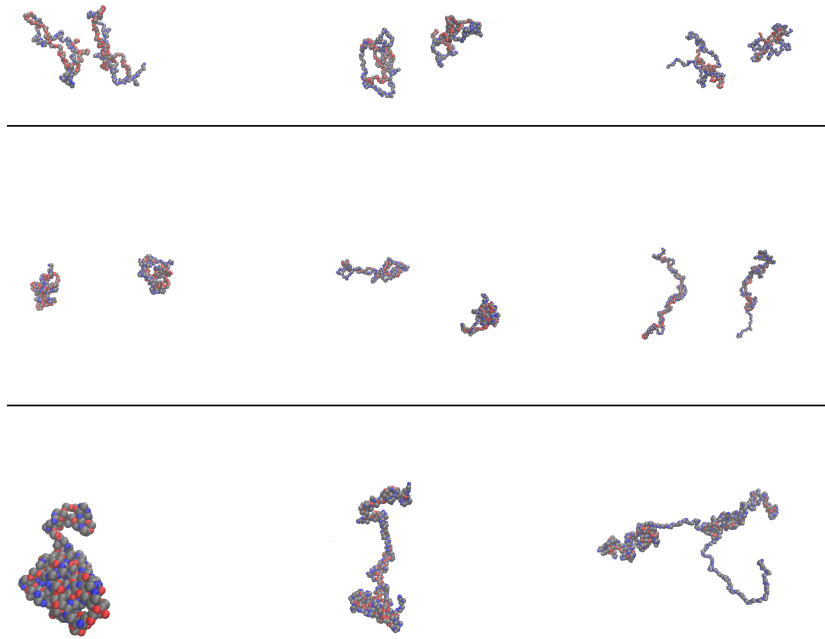
Figure 4.1: Snapshots of the two asymmetric PA chain systems, each obtained at $t = 10^5 \tau_{\mathrm{LJ}}$ after turning off the drag force between their centres of mass. From left to right, the chain lengths are $N = 272, 320, 384$, respectively, corresponding to the asymmetries of $\Delta N/N_+$ from $1/8, 1/2$ to 1. The Bjerrum length increases from top to bottom as $\ell_B/\sigma = 1/4, 1$ and 4.

$N = 272$ at $\ell_B/\sigma = 4$ takes the configuration of a globular head and a double-helix tail. The one formed by two chains with $N = 320$ takes a similar configuration, but a longer helix/PE core tail due to the larger N_- and so higher asymmetry. A close inspection indicates that each positively charged block is associated with the negatively charged block of the other chain. This is a favourable arrangement for holding the two chains together, although they may still separate at longer times. When the asymmetry is further increased to $\Delta N/N_+ = 1$ and so $N = 384$, the aggregate already starts to disassociate with only a small associating section between the PE tail of one chain with the helix/PE core head of the other chain. Each geometric part of the chain conformation, i.e., the helix/PE core head or PE tail, is negatively charged and there is no strong charge density fluctuations in the head to give rise to the local attraction. Therefore the two PA chains tend to repel each other at high l_B values.

Figures 4.2 and 4.3 present snapshots of two much longer chains with $N = 1124$ ($N_+ = 512$ and $N_- = 612$) at $\ell_B/\sigma = 1/2$. Figure 4.2 demonstrates the two blocks in each chain already wrap around each other to form a helix/PE core structure. Figure 4.2 shows the polymers coloured by the chain they belong to, and shows that these coils can belong to the same chain. This helix/PE core structure is relatively long and flexible, so can still coil up to give a head of globule-like shape. Such helix/PE core structures are net charged and so do not tend to aggregate with each other, so do the PE tails. The two PA chains thus eventually separate from each other.

Coulomb energy analysis

Since the association of the asymmetric PA chains is driven by the local charge density fluctuations, the stability of the preassembled aggregates can be partly understood from analysing the electrostatic interaction energies of the PA chains in their aggregate or separate state, $E_{\text{aggregated}}$ or $E_{\text{separated}}$, respectively. As there are only two PA chains,
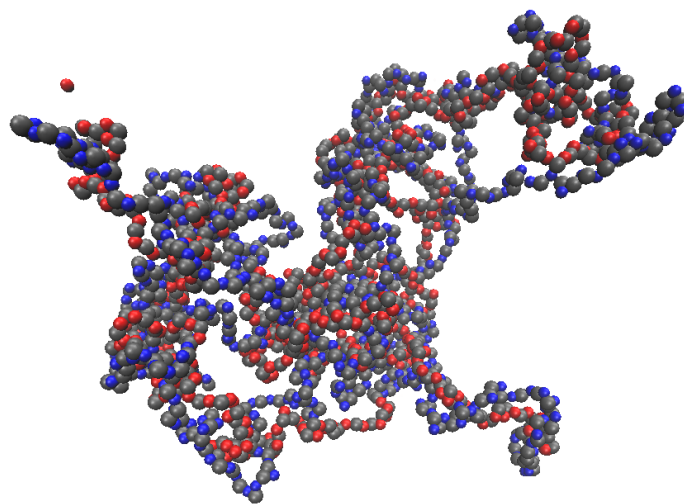
Figure 4.2: Snapshot of two preassembled asymmetric PA chains with length $N = 1124$ $(N_+ = 512)$, $f = 1/2$ and $\ell_B/\sigma = 1/2$.
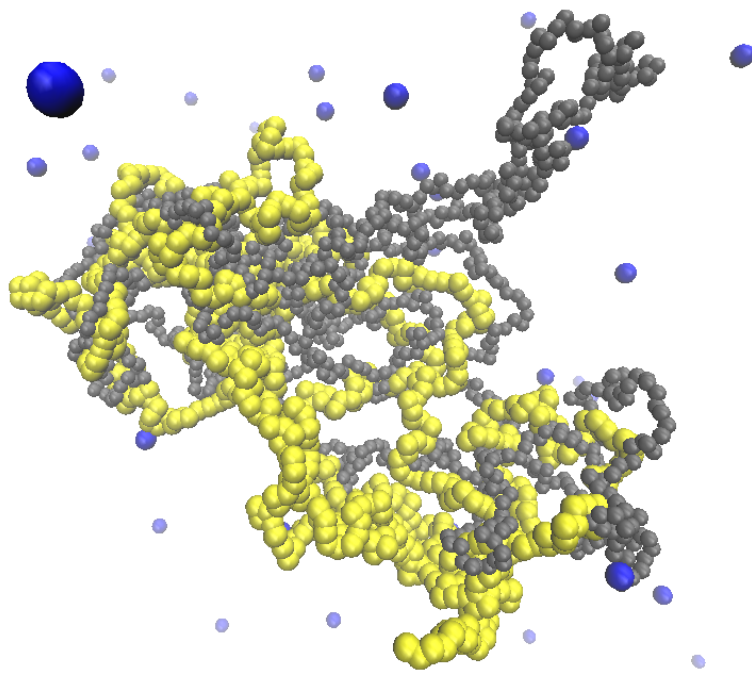
Figure 4.3: Snapshot of two preassembled asymmetric PA chains, including counterions with length $N = 1124$ ($N_+ = 512$), $f = 1/2$ and $\ell_B/\sigma = 1/2$, coloured by chain and counterion

they are either aggregated or separated, never both at once. We can also calculate the Coulomb energy for each block of the chains.

In Figure 4.4 we plot the total Coulomb energies of the systems comprised of two preassembled asymmetric PA chains with chain lengths (a) $N = 272$ and (b) 320 as functions of time, respectively. For comparison, the Coulomb energies calculated for the two chains in their aggregate and separate states are also included, where only the monomer contributions are included. More precisely, these energies are calculated as

$$E_{\text{tot}} = E_{\text{monomer-monomer}} + E_{\text{monomer-counterion}} + E_{\text{counterion-counterion}} \quad (4.3)$$

$$E_{\text{aggregated (separated)}} = E_{\text{tot}} - E_{\text{counterion}} \quad (4.4)$$

The Bjerrum length is $\ell_B/\sigma = 1$ in both cases. Time zero in these plots corresponds to the moment when the artificial drag force is removed. In each system, the total Coulomb energy shows a drop at the transition point when the two chains start to separate from each other, indicating that the unimer phase is energetically more favourable. The variation of the system configuration from the aggregate to separate state can be visualised from the snapshots taken at different times. It should be noted that the results in Figure 4.4 do not include surface energy which is theoretically predicted to stabilise the micellar core by balancing the electrostatic repulsion [13]. The translational entropy is another factor which can drive the chains to leave each other. At least for the systems shown in Figure 4.4, the surface energy gain does not seem to be sufficient to overcome the electrostatic repulsion between the net charges of the PA chains and the translational entropy. A more rigorous calculation of the interaction potential, or the potential of mean force (PMF), between two PA chains can be obtained from the umbrella sampling simulations as discussed below.

The contributions of counterions to the total Coulomb energy of the system can

be calculated using the data in Figure 4.4 as $E_{\text{tot}} - E_{\text{aggregated (separated)}}$, depending on the interested time scale. Their contributions are relatively small for the systems with low chain asymmetry because of the small number of counterions (e.g., 16 for two PA chains of length $N = 272$) . They become more important with the increase of the chain asymmetry, as seen in Figure 4.4(b) for the system with $N = 320$. The counterion contributions may also vary with the change of the number density of particles, because the counterions will prefer to stay away from the PA chains due to translational entropy.

Figure 4.5 presents the results on the average Coulomb energy per charged monomer obtained from the MD simulations of two preassembled asymmetric PA chains. The chain lengths are selected to be $N = 272, 320$ and 384, corresponding to the systems studied in Figure 4.1. For each given system with chain length N and Bjerrum ℓ_B, the energy is calculated for all charged monomers in the system, E^N, and also for those in the positively and negatively charged blocks, E^{N+} and E^{N-}, respectively. As shown in 4.1, depending on N and ℓ_B, the two preassembled PA chains may separate from each other at a certain time. In such a case, the Coulomb energy is calculated by averaging over both the aggregate regime, noted as $E^{N(+,-)}_{\text{aggregated}}$, and the separate regime, $E^{N(+,-)}_{\text{separated}}$. If the two chains remain aggregated over the entire simulation run, the results are only given for $E^{N(+,-)}_{\text{aggregated}}$. For the two nearly symmetric chains with $N = 272$, the chains fluctuate between being in the aggregated and separated states at $\ell_B/\sigma \leq 1$, owing to the relatively weak electrostatic attractions between the two chains, induced by the local charge density fluctuations, allowing chain entropy to play a more significant role. The energy difference between the aggregate and separate states in these cases is negligible. At larger ℓ_B, the two chains always remain to be associated, which is consistent with the association tendency of symmetric PA chains. When the chain length, and consequently the chain asymmetry, is increased, the Coulomb energy of the system in
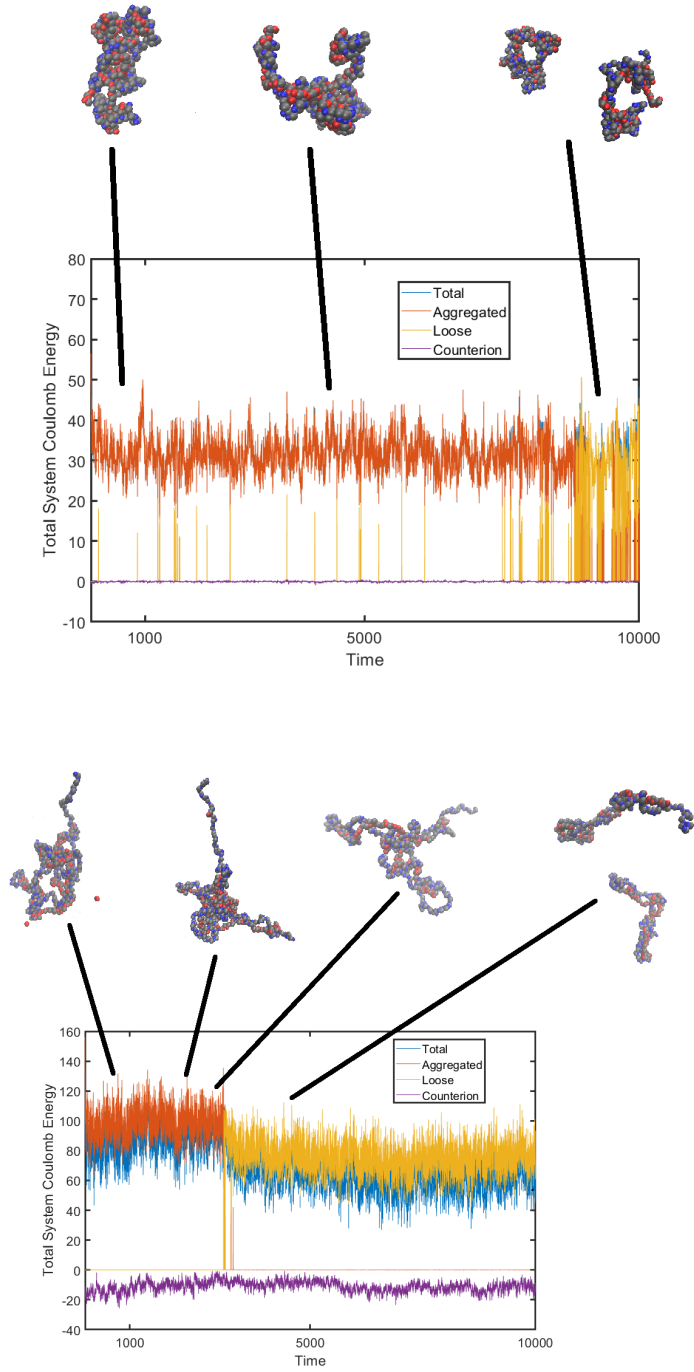
Figure 4.4: Coulomb energies of the systems comprised of two preassembled asymmetric PA chains with chain lengths (a) $N = 272$ and (b) 320, respectively. The Bjerrum length is $\ell_B/\sigma = 1$. Here the total energy refers to the total Coulomb energy of the whole system including the two PA chains and counterions, while the Aggregate and Separate energies refer to the Coulomb energies of the two PA chains (excluding counterions) when they are in the aggregate and separate states, respectively. The data points are block averaged values over time block interval of $1000\tau_{LJ}$. The snapshots of the PA chains at different times are also included for reference.

the separate state becomes lower than that in the aggregate states, and so the two chains separate into unimers after a certain time. For $N = 384$, the separation happens at $\ell_B/\sigma \leq 2$. The overall Coulomb energy of the system also stays positive, reflecting the electrostatic repulsion feature between the highly asymmetric PA chains. At high Bjerrum lengths $\ell_B/\sigma = 4$, the total Coulomb energies of all three systems are negative and the chain aggregation is likely the stable state, although further study is required to confirm this system is not trapped in a meta stable state.

The Coulomb energies calculated for individual blocks can provide further information about the association state of the PA chains. Since the length of the positively charged block is fixed, the attractive energy gain per charged monomer in these blocks increases with the increase of the chain length due to the presence of more negatively charged monomers, but this is counter balanced by the increment in the repulsive energy in the longer negatively charged blocks. It is the sign of the total Coulomb energy, together with the surface energy, that determines the association state of the PA chains.

Potential of mean force between two PA chains

The association possibility of two PA chains can be found by calculating their potential of mean force using umbrella sampling simulations. To test our implementation of the umbrella sampling method, we first run simulations to calculate the PMF between two identical polyelectrolyte chains of length N and compare the results with the known potential expression of $U(r) = l_B k_B T N^2 / r$ as expected for two point charges of valence N at distance r. In all cases, we run $N_w = 16$ individual windows in parallel and fix the windows to have the biased potential equilibrium value $d_{\mathrm{eq}} = 4ir/\sigma$, $i = \{0, 1, .., 15\}$ apart. The longest chain we simulate is $N = 320$, with Bjerrum length $\ell_B = 1.0\sigma$. From Figure 3.25, one can see that the longest average end to end distance for a chain of this
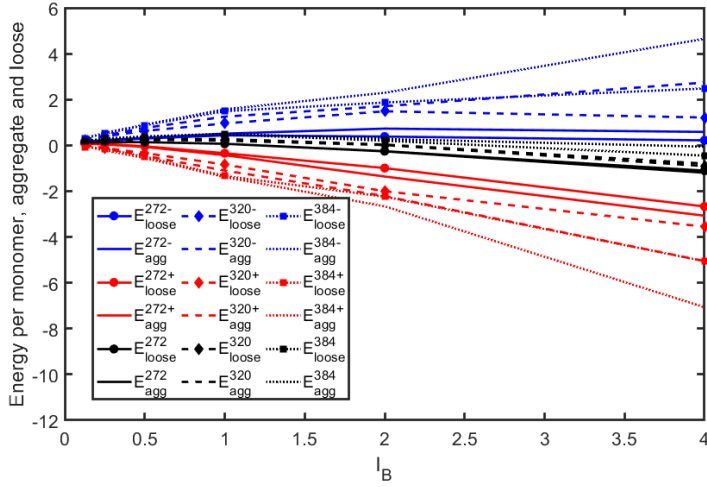
Figure 4.5: Average Coulomb energy per charged monomer obtained from simulations of two preassembled asymmetric PA chains. See the main text for the description of the data sets.
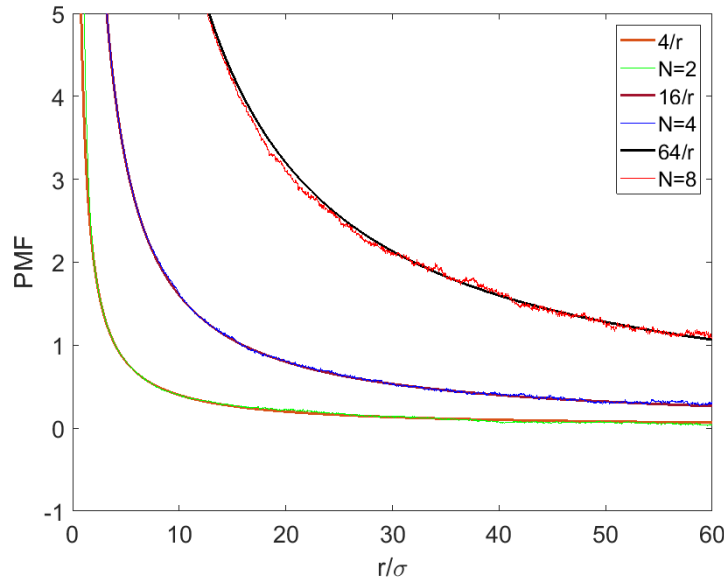
Figure 4.6: Potential of mean force between two identical polyelectrolyte chains of lengths $N = \{2, 4, 8\}$ and charge fraction $f = 1$ at $\ell_B/\sigma = 1$ as obtained from umbrella sampling simulations. For each system, the potential of mean force similar to $U(r) = l_B k_B T N^2/r$ as expected for two point charges of valence N at distance r is also included for comparison.

84

length is $R_e^+ \approx 30$. As the furthest equilibrium value is around twice this distance, we argue that this is enough to capture the difference between associated and disassociated states. Figure 4.6 shows that our umbrella sampling simulation generate PMF results in very good agreement with the potential of the idealised point charge systems at distances larger the radii of gyration of the PE chains. This validates the implementation of the method. These chains are relatively small, and with a Bjerrum length $\ell_B/\sigma = 1$ there is no counterion condensation. Thus, these PE chains take a stretched configuration due to the electrostatic repulsions between the like charged intrachain monomers, with chain end-to-end distance $N\sigma$. Variation in the conformational entropy in these chains is very small; two similarly charged PE chains undergo purely repulsive interactions, and is analogous to two rigid charged rods. The rotational entropy has been taken into account via the ensemble average. If we simulated PE chains that are much longer, the fitting may not work at shorter centre-to-centre distances between the two chains due to the entropic contributions of the chains.

Our calculation of the PMF of diblock PA chains starts with the shortest chains of length $N = 2$ which are actually dipoles consisting of one positively and one negatively charged monomer. Figure 4.7 presents the PMF results for different electrostatic interaction strengths. At very low ℓ_B values, the excluded volume effects dominate. With increasing ℓ_B the PMF shows the $1/r^6$ behaviour at larger distances which is the average interaction potential between two rotating dipoles. At higher ℓ_B, an electrostatic attraction well appears at around $r = 2\sigma$, corresponding to the head to tail association of the two dipoles. A further increase in ℓ_B leads to another well at $r \approx \sigma$, corresponding to the formation of a quadrupole [12]. In any case the steep growth of the PMF at small r is due to the Lennard-Jones potential which prevents the overlap of the monomers.

Figure 4.8 presents the PMF results calculated for two symmetric diblock PA chains.
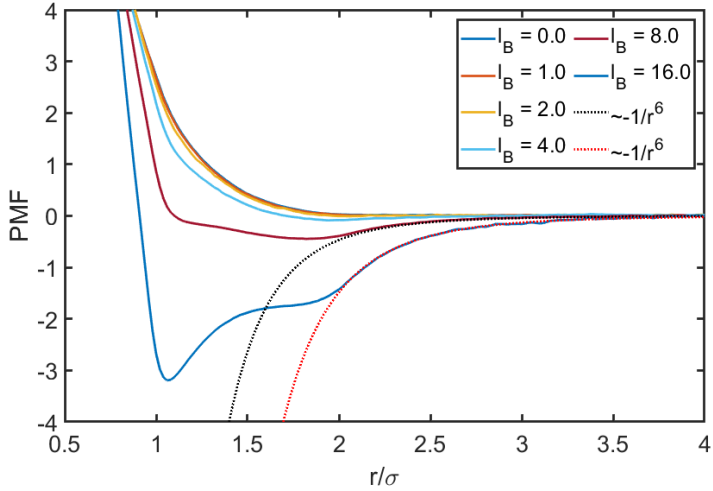
Figure 4.7: Potential of mean force obtained from umbrella sampling simulations of a pair of dipoles each consisting of one positively and one negatively charged monomer.

The chain length is increased from $N = 4$ to 256 for two charge fractions $f = 1/2$ and $1/4$. The Bjerrum length is $\ell_B/\sigma = 1$ in all cases. The number of monomers in an electrostatic blob at this ℓ_B can be estimated as $g_e \approx (l_B f^2/\sigma)^{-1/(2-\nu)} \approx f^{-1.416}$ where $\nu = 0.588$ for good solvent condition. It gives $g_e \approx 2.67$ for $f = 1/2$ and 7.12 for $f = 1/4$. These g_e values are subject to change by a constant multiplication factor, considering the scaling feature of the estimation and that the chain segments at these length scales are not flexible. Anyhow, they imply that for short diblock PA chains each block may correspond to only one or few electrostatic blobs. The fluctuation-induced attractions between the two chains are not strong enough to overcome the translational entropy. They will tend to stay as unimers. The PMF data for the short diblock PA chains thus show the general repulsive feature. With the increase of chain length, the number of electrostatic blobs per block also increases. The symmetric PA chains will aggregate into globular clusters whose structures are represented by the dense packing of oppositely charged electrostatic blobs [12]. Correspondingly the PMF of the longer symmetric diblock PA chains show significant attractive character at short distances.
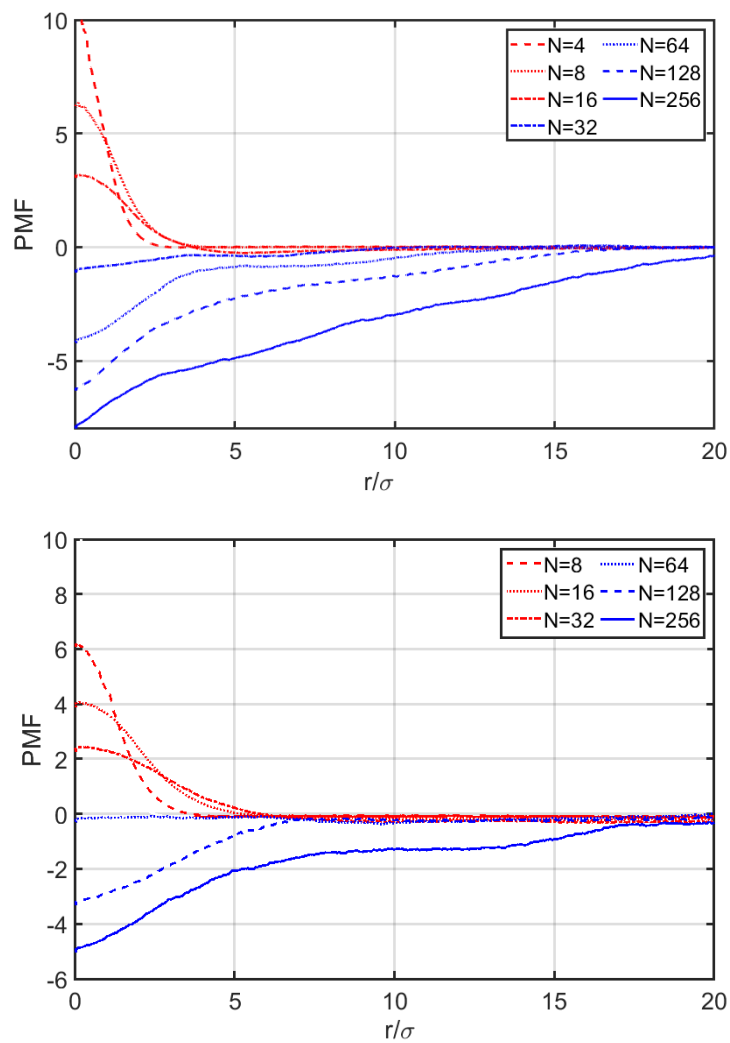
Figure 4.8: Potential of mean force obtained from umbrella sampling simulations of two symmetric diblock PA chains for various chain lengths and charge fractions $f = 1/2$ (a) and $1/4$ (b) . The Bjerrum length is $\ell_B/\sigma = 1$ in all cases.

As a result, in the solutions of long symmetric diblock PA chains (say with $N = 256$) the aggregate can keep on growing to form a sediment phase. Unlike the steep growth in figure 4.7, as the chain length increases in figure 4.8, the centres of mass become easier to overlap, resulting in a softening of the potential.

Figure 4.9 shows the PMF data for asymmetric diblock polyampholytes with asymmetry $\Delta N/N_+ = 1/8$. The chain length is increased from $N = 34$ to 272 with an increment factor of 2 for N_+. Two charge fractions $f = 1/2$ and $1/4$ are studied and the Bjerrum length is $\ell_B/\sigma = 1$ in all cases. These results are qualitatively similar to those of the symmetric PA chains with same N_+ values in Figure 4.8 due to the relatively low asymmetry. But for each given N_+, in the $f_+ = 1/2$ case, the attraction strengths at short distances between the asymmetric chains are weaker than those of their symmetric counterparts. This can be more conveniently seen by comparing the PMF values at $r = 0$. For example, this PMF value is about $-5k_BT$ for the asymmetric chains with $N = 272$ and $f = 1/2$, which it is close to $-8k_BT$ for the symmetric chains with $N = 256$ and $f = 1/2$. The difference can be understood from the electrostatic repulsion caused by the net valences of the asymmetric chains. Figure 4.9 indicates that PA chains with relatively low asymmetry can aggregate into clusters if their centres of mass can approach each other within a certain distance.

When the centre-of-mass distance between two chains is beyond their overlapping range, the PMF shows the repulsive behaviour as expected for the interaction between two likely charged objects. This is more evident for the longer chains due to the larger net valence per chain. Two PA chains with $N = 272$ and $f = 1/2$ at $\ell_B/\sigma = 1$ repel each other at a separation $r \geq 20\sigma$. The average radius of gyration of such chains is $R_g \approx 7\sigma$. For the asymmetric diblock PA chains to aggregate into stable clusters or micelles in dilute solutions, they need to overcome the long-range repulsion in order to approach each other. On the other hand, two previously aggregated chains can
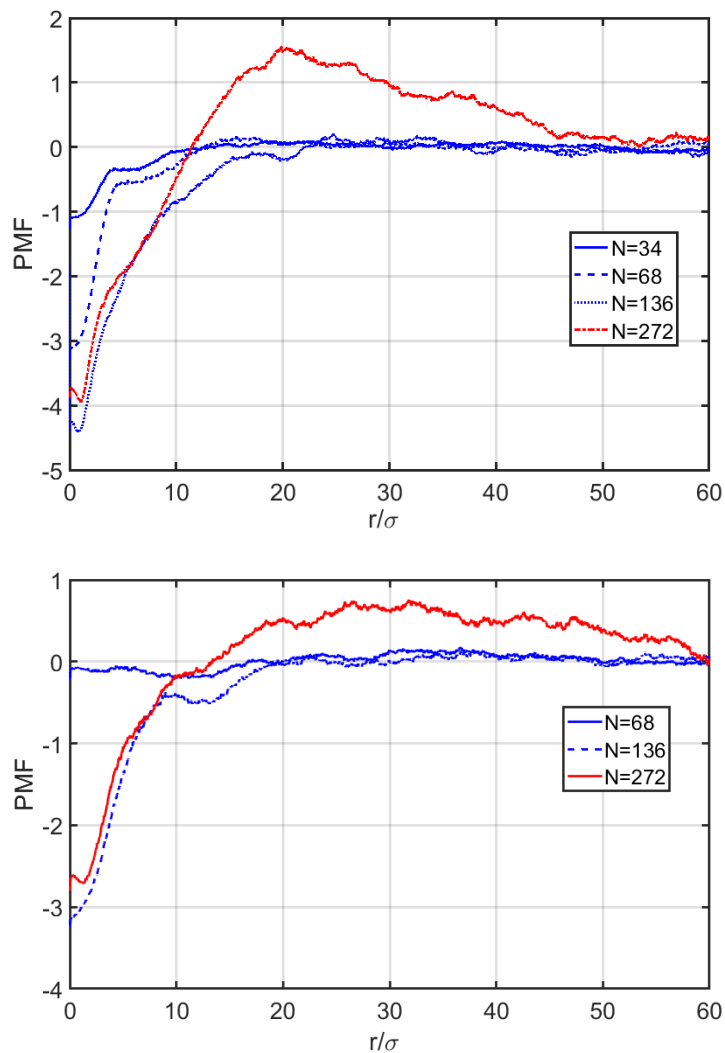
Figure 4.9: Potential of mean force obtained from umbrella sampling simulations of two asymmetric diblock PA chains with asymmetry $\Delta N / N_+ = 1/8$ for various chain lengths and charge fractions $f = 1/2$ (a) and $1/4$ (b). The Bjerrum length is $\ell_B / \sigma = 1$ in all cases.

undergo many association-dissociation events due to thermal fluctuations. When the separation between their centres of mass is large enough, the electrostatic repulsion will push them away. They can either associate with other neighbouring chains in solutions with relatively high polymer concentrations, or simply draft away in dilute solutions. The latter case is shown in Figure 4.1 for the two chains with $N = 272$ and $f = 1/2$ at $\ell_B/\sigma = 1$. A critical concentration of PA chains needs to be met for the formation of stable aggregates or micelles.

The situation is totally different for highly asymmetric diblock PA chains. As shown in Figure 4.10. Here we present just the longest chain studied, as a means of comparison with the longer chains in Figures 4.8 and 4.9. The PMF between two PA chains with length $N = 320$ and so asymmetry $\Delta N/N_+ = 1$ at $\ell_B/\sigma = 1$ shows strong repulsion behaviour for the entire range of reaction coordinates studied. Therefore such highly asymmetric chains could not form stable aggregates.

A note on initial configurations used in umbrella sampling

When performing umbrella sampling simulations of systems with chain lengths $N \geq 128$, we observe a common problem related to the initial configurations of the system, which results in unphysical knotting or hooking of the two chains when the charges are turned on, see Figure 4.11. Due to the chains being held a certain distance apart, sometimes when the charges are turned on the blocks collapse into an unfavourable configuration but are unable to reorient into a more favourable position due to the positioning of the centre of mass being held. Whilst knots may appear in reality, specifically in this situation the chains look like two pieces of overlapping string being pulled apart, and is clearly not realistic. One possible solution is to relax the chains separately to avoid the initial knotting and then drag them to their reference distance. However this approach could be problematic for the aggregating state, because it may
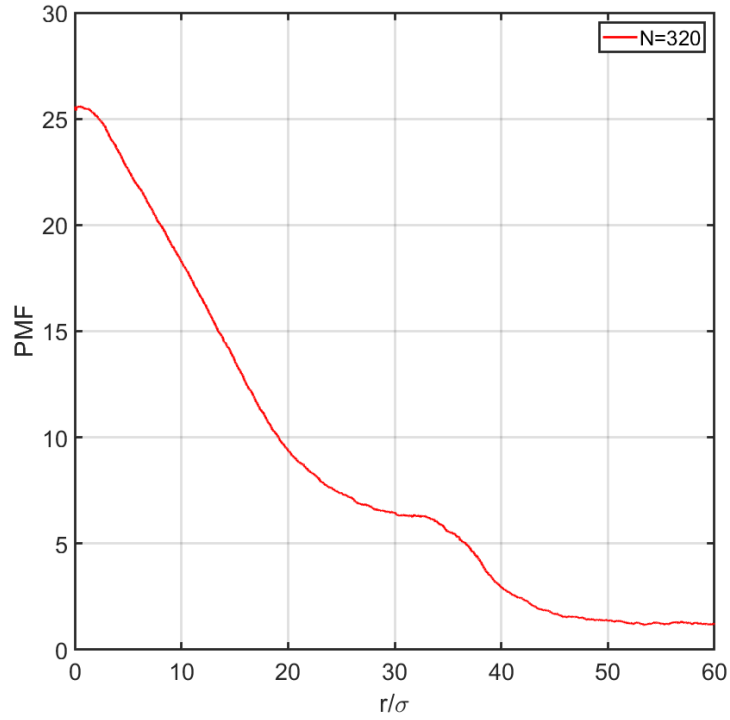
Figure 4.10: Potential of mean force obtained from umbrella sampling simulations of two asymmetric diblock PA chains with length $N = 320$, asymmetry $\Delta N/N_+ = 1/2$ and $f = 1/4$. The Bjerrum length is $\ell_B/\sigma = 1$.
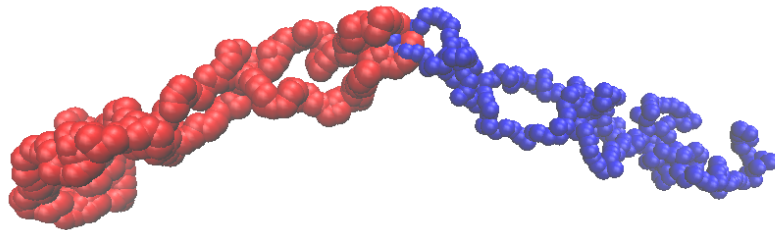
Figure 4.11: Evidence of an infrequent unphysical knot, caused by the bias potential harmonic spring between the centres of mass of the two chains (red and blue). Two symmetric chains, $N = 256$, peak distribution $16r/\sigma$
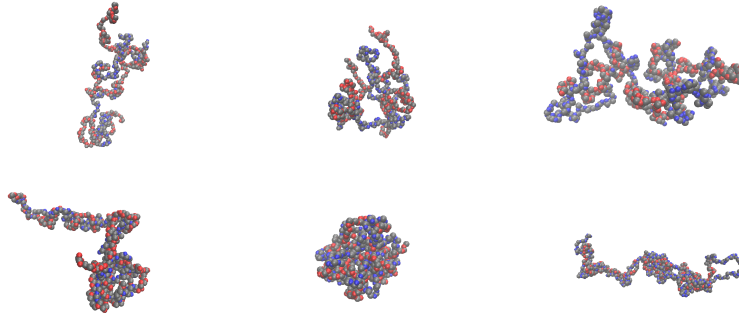
Figure 4.12: Snapshots of the systems comprised of two asymmetric diblock PA chains with one PE stabiliser taken at $t = 10^5 \tau_{\mathrm{LJ}}$ in the MD simulations. From left to right, the lengths of the PA chains are $N = 272, 320$ and $N = 384$, corresponding to asymmetries $\Delta N / N_+ = 1/8, 1/2$ and 1, respectively. The length of the PE chains in all systems is $N_{\mathrm{PE}} = N_+ = 128$. The Bjerrum length is $\ell_B / \sigma = 1/8$ in the top row and 1 in the bottom row.

lead to unfavourable configurations at the early stage in the simulation and consequently affect more than one windows. Another solution is to run parallel tempering during the warm-up process, check for the undesired configurations with knotting behaviour and filter them out . However this is computationally costly, because many parallel runs are needed if we do not know which system will knot. We found that the unphysical knotting situation can be easily spotted in the probability distribution of the centre-of-mass distances in a simulation window when it tends to overlap with the distribution in a neighbouring window. In that case, we run 10 more simulations in that specific window and pick up the ones that do not knot.

Polyelectrolyte Stabiliser

As discussed in Chapter 3, the single asymmetric PA chains tend to take the conformations of a net charged elongated globular or helix/PE core head, where the short positively charged block is wrapped by the longer negatively charged block, and a polyelectrolyte tail if the asymmetry is high. For forming a stable cluster or micelle, the

92

head structures need to open up allowing them to interpenetrate each other and have cross associations of the blocks or electrostatic blobs from one chain with oppositely charged blocks or electrostatic blobs from other chains. But in the process of aggregation or micellization, when the PA chains meet each other in a solution, there may be no sufficient time for them to unwrap the head structures before separating apart again due to the electrostatic repulsion and translational entropy, see Figure 4.1.

Here we propose a potential solution by introducing positively charged polyelectrolyte chains into the solution which effectively work as cross-linkers to bridge the overall negatively charged PA chains and allow them sufficient time to unwrap and remix their oppositely charged blobs. The PE chains also help to reduce the net valences of the aggregates and make them more stable. As a preliminary test, we set the length of the PE chains equal to that of the positively charged blocks of the diblock PA chains, i.e., $N_{\mathrm{PE}} = N_+ = 128$. They also have the same charge fractions as the PA chains they are mixing with. This choice is probably also convenient from the experimental point of view, because only one type of positively charged chains need to be synthesised. For each system comprised of two PA chains, one PE chain is introduced.

Figure 4.12 shows the snapshots of the systems consisting of two asymmetric diblock PA chains and one PE stabiliser. The lengths of the PA chains are $N = \{272, 320, 384\}$. The total net charges on the three polymer chains in each system are thus $\{+48, 0, -64\}$ at charge fraction $f = 1/2$, respectively. Despite the net charges in some of the systems, the preassembled aggregates in all studied systems remain stable throughout the entire simulation duration. It is noted that helix/PE core is still the dominating local structure, but now can be formed by blocks from different PA chains or with the PE chain.

It may look like that the effect of introduction PE chains can also be achieved by simply reducing the asymmetry of the diblock PA chains. But the key difference

lies in their role of bridging the PA chains to prevent them from running away before establishing interchain associations of the oppositely charged blocks or electrostatic blobs. To keep the original asymmetry of the PA chains also means that only a few relatively long negatively charged blocks need to stick out of the aggregate which carry part of the overall excess net charges of the system and stabilise the globular core to form stable micelles. The functioning of the PE stabilisers will be examined in section 4.2.1 for the aggregates comprised of 16 chains which are more relevant to micelles studied in theoretical models [13].

4.1.4   Conclusions

The association behaviour between two asymmetric diblock polyampholytes have been studied by MD simulations using pre-assembled aggregates over a range of chain lengths and asymmetries, charge fractions and Bjerrum lengths. The potential of mean force between two asymmetric PA chains has also been calculated using umbrella sampling methods. The PMF results show that two PA chains with relatively low asymmetry are attractive to each other at centre-of-mass distances comparable or smaller than the chain size, which favours the chain aggregation. At larger centre-of-mass distances, they repel each other as expected for two likely charged objects. Since the single asymmetric diblock PA chains tend to take the conformations of an elongated globular or helix/PE core shape at low asymmetries and a head-tail geometry with an elongated globular or helix/PE core head and a single polyelectrolyte tail at high asymmetries, the formation of stable clusters or micelles requires the interpenetration of the globular or unwrapping of the helix/PE core structures to allow the interchain associations of oppositely charged blocks or electrostatic blobs. The successful association between two chains may require multiple attempts as the shallow penetration can be easily

disrupted by thermal fluctuations and the intrinsic electrostatic repulsion between the likely charged chains. At concentrations below a critical (micellization) value, even the preassembled PA chains will separate from each other due to translational entropy. This is observed in our MD simulations of the preassembled PA chains with different asymmetries at $\ell_B/\sigma \leq 1$. On the other hand, the PMF data of highly asymmetric PA chains show repulsive behaviour for the entire centre-of-mass distance range, indicating that no stable aggregates could be formed by such chains.

In order to facilitate the formation of stable aggregates, we have proposed to introduce positively charged polyelectrolyte chains into the solutions of asymmetric PA chains, which can work as cross-linkers to bridge the PA chains with net negative valences and enhance the probabilities of interchain association of the oppositely charged blocks or electrostatic blobs. An addition of a PE chain to the systems of the two asymmetric PA chains lead to stable aggregates at all chain asymmetries studied at $\ell_B/\sigma = 1$ over the entire simulation duration.

4.2 Stability of pre-assembled aggregates of asymmetric diblock PA chains

4.2.1 Introduction

Shusharina et al predicted that the diblock polyampholyte chains with tadpole shape conformations will aggregate into micelles when the surface energy gain due to the aggregation of their heads is larger than the repulsion energy between their tails [13]. The micelles are predicted to take star-like geometry consisting of a globular core, where most of the constitute chains are completely confined in, and a long corona consisting of entire stronger charged blocks of other chains, carrying part of the excess charges of

the system. This is energetically more favourable than the so-called crew-cut micelle structure where each constitute diblock chain sends out part of its longer block to form a short corona.

For a micelle comprised of N_{poly} diblock PA chains of length N in a $\theta-$solvent, the core size is predicted to be [13]

$$R_{\text{core}} \approx \sigma N_{\text{poly}}^{1/3} N^{1/3} \left(\ell_B f^2 / \sigma \right)^{-1/9}, \qquad (4.5)$$

and the surface energy per chain is given by

$$\frac{F_{\text{surf}}}{k_B T} \approx \frac{R_{\text{core}}^2}{N_{\text{poly}} \xi_e^2} \approx N_{\text{poly}}^{1/3} N^{2/3} \left(\ell_B f^2 / \sigma \right)^{4/9}, \qquad (4.6)$$

where ξ_e is the size of electrostatic blob size.

Balancing the surface energy of the micellar core and the electrostatic energy in the corona, the equilibrium aggregation number of a micelle formed under the condition that most of the counterions are in the surrounding solutions is

$$N_{\text{poly}} \approx N^{-1/3} \left(\frac{\Delta N}{N} \right)^{-5/3} \left(\ell_B f^2 / \sigma \right)^{-2/9}. \qquad (4.7)$$

We perform MD simulations of preassembled aggregates comprised of 16 asymmetric diblock PA chains over a range of chain lengths and electrostatic interaction strengths. The main focus is on examining the stability of the preassembled aggregates and whether the star-like or the crew-cut structure is more favourable for the systems with composition falling well into the parameter range for forming stable micelles as predicted by the theoretical work of Shusharina et al. [13].

4.2.2 Models and Simulation Methods

Unless otherwise stated, we simulate preassembled aggregates comprised of $N_{\text{poly}} = 16$ asymmetric diblock PA chains of length $N = \{256, 264, 272, ..., 384\}$ at Bjerrum lengths $\ell_B = \{0.125, 0.25, 0.5, 1.0, 2.0, 4.0\}\sigma$. The length of the positively charged blocks is fixed to $N_+ = 128$ and the fraction of charged monomers is $f = 1/2$. We are interested in polymers in a good solvent and thus we take the LJ potential parameters $\epsilon_{\text{LJ}} = 1 k_B T$ and $r_{\text{cut}} = 2^{1/6}\sigma$. For the FENE coefficients we choose $k_{\text{FENE}} = 7 k_B T / \sigma^2$ and $R_{\text{FENE}} = 2\sigma$ to be consistent with the literature [12]. Periodic boundary conditions are applied with the electrostatic interactions handled by the P3M method. The number density of particles (monomers and counterions) is taken to be $\rho = 10^{-3}\sigma^{-3}$.

Our simulations begin with warming up the neutral chains for a time duration of $10^3 \tau_{\text{LJ}}$, and then dragging them together by harmonic springs connecting their centres of mass to relax for another time period of $10^4 \tau_{\text{LJ}}$. Following that the charges are turned on and the system continue to relax for another $10^4 \tau_{\text{LJ}}$ with the drag forces on. The main simulations start at time $t = 0$ right after the drag forces are turned off.

4.2.3 Simulation Results and discussions

Figure 4.13 presents the snapshots of the systems comprised of 16 preassembled asymmetric diblock PA chains with lengths $N = \{256, 272, 288, 320, 384\}$ at two different Bjerrum lengths $\ell_B/\sigma = 0.5$ and 1 taken shortly after the drag forces are turned off. The aggregates simulated at $\ell_B/\sigma = 1$ show clear star-like micellar structures and the number of long arms in the corona increases from 0 in the symmetric case to 2 at $N = 272$ and asymmetry $\Delta N/N_+ = 1/8$, 5 at $N = 288$ and $\Delta N/N_+ = 1/4$ and more for longer chains and so higher asymmetries. In all cases studied, the total number of arms is always smaller the number of chains in the aggregate. This provides qualitative
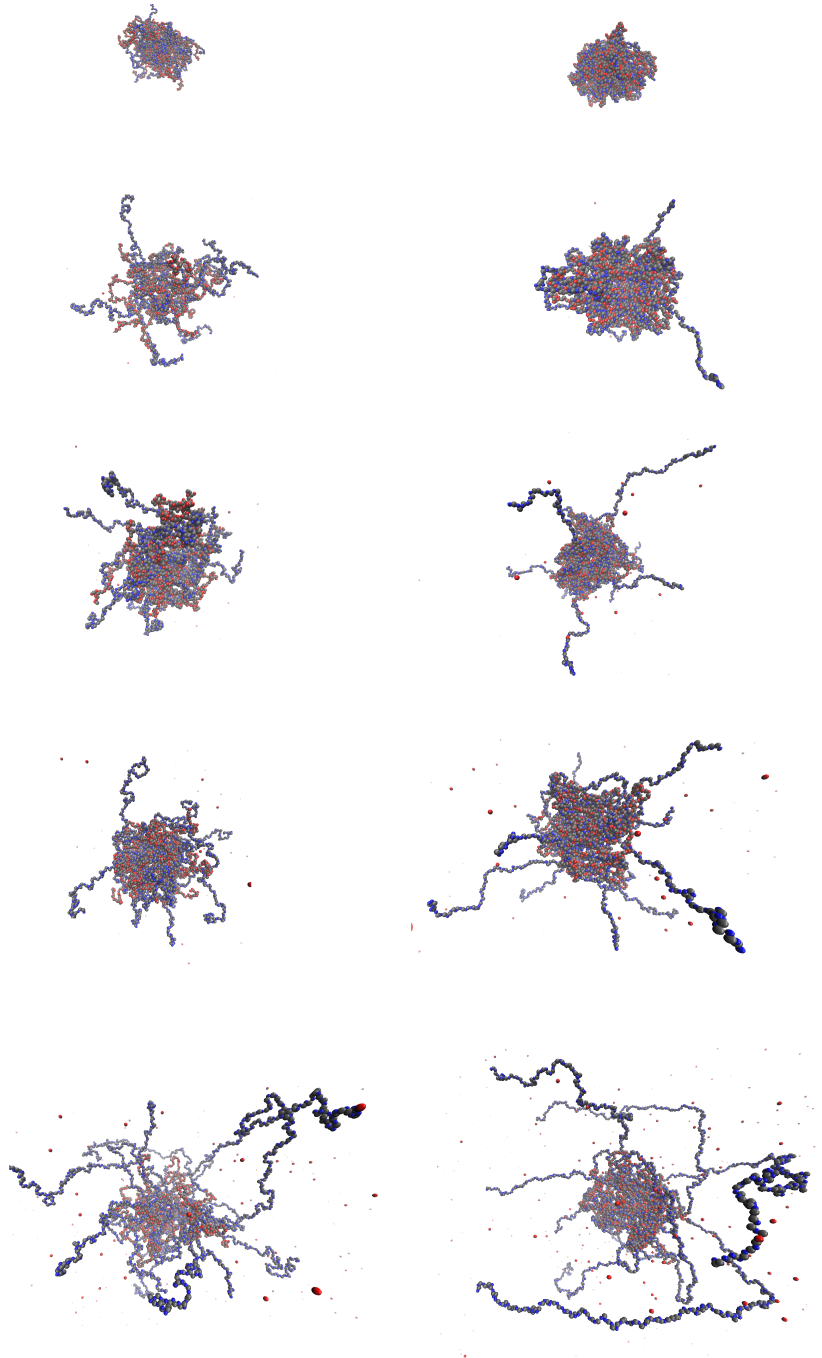
Figure 4.13: Snapshots of the systems comprised of 16 preassembled asymmetric diblock PA chains taken at simulation times $1 \sim 2 \times 10^4 \tau_{\mathrm{LJ}}$ after turning off the drag forces. From top to bottom, the chain length in each row increases as $N = \{256, 272, 288, 320, 384\}$. The Bjerrum length is $\ell_B/\sigma = 0.5$ in the left column and 1 in the right column.
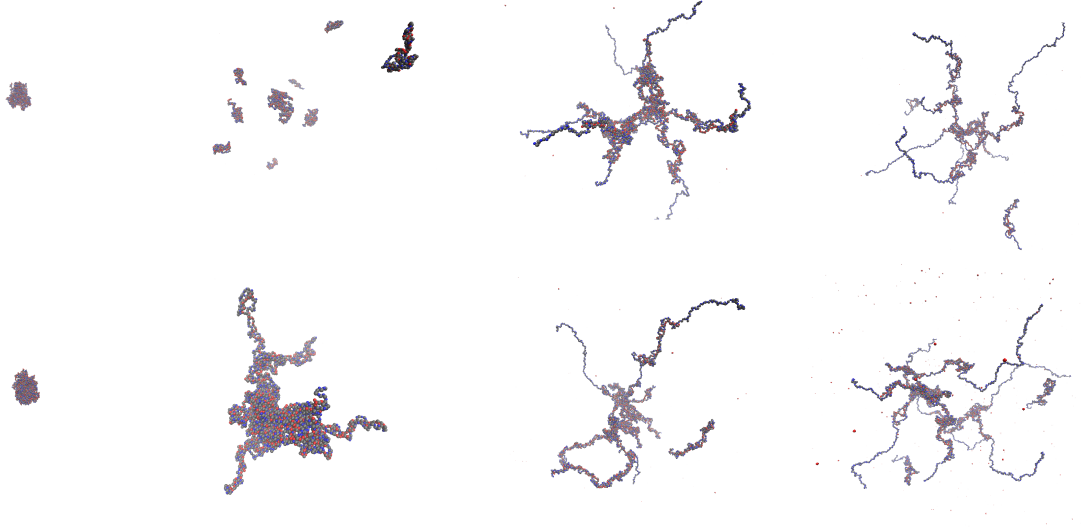
Figure 4.14: Snapshots of the systems comprised of 16 preassembled asymmetric diblock PA chains taken at simulation times at simulation times $9 \times 10^4 \sim 10^5 \tau_{\mathrm{LJ}}$ after turning off the drag forces. From left to right, the chains lengths are $N = 256, 272, 320$ and 384, respectively. The Bjerrum lengths are $\ell_B/\sigma = 1$ in the top row and 4 in the bottom row.

support to the star-like picture predicted by Shusharina et al. [13]. However these micelle-like structures are unstable and will evolve into different types of structures depending on the system parameters.

In the top row of Figure 4.14, we show the snapshots of the systems studied in the right Column of Figure 4.13 at $\ell_B/\sigma = 1$ which are taken at simulation times significantly after turning off the drag forces. The aggregate formed by symmetric chains with $N = 256$ remains to be stable as expected. But that formed by the slightly asymmetric chains with $N = 272$ and $\Delta N/N_+ = 1/8$ breaks into smaller clusters of various sizes. The aggregates constructed by chains with larger asymmetries also have some unimers broken off. The remaining parts of the aggregates evolve into star-like or hyper-branching structures with "arms" or "strands" composed of helical structures and single PE tails. In the highly asymmetric cases, such as $N = 384$ ($\Delta N/N_+ = 1$), the

PA chains take highly stretched conformations composed of helix/PE core and single PE segments. They connect with each other and even with their periodic images to form percolated network structures.

An increase of the Bjerrum length to $\ell_B/\sigma = 4$ does not improve the situation. As shown in the bottom row of Figure 4.14, the aggregates constructed by PA chains with low asymmetries $\Delta N/N_+ \leq 1/8$ remain intact but take non-globular shape, see the case with $N = 272$. But the aggregates formed at higher asymmetries also evolve into complex structures, similar to those at $\ell_B/\sigma = 1$. The complication of the structures formed in different systems make sit difficult to develop theoretical models to describe them.

Coulomb energy analysis

Figure 4.15 presents the simulation results on the total Coulomb energies, $E_{\text{tot}}(t)$, of the systems consisting of 16 asymmetric PA chains as functions of time. For the system comprised of symmetric chains with $N = 256$, $E_{\text{tot}}(t)$ reaches its plateau value shortly after turning off the drag force. The average plateau value decreases with the increase of the Bjerrum length, indicating that the preassembled aggregate is getting more and more stable.

The E_{tot} data of the system with low chain asymmetry of $\Delta N/N_+ = 1/8$ ($N = 272$) also show a general trend of decreasing with the increasing electrostatic interaction strength. A more detailed energy analysis of this system at $\ell_B/\sigma = 1$ is given in Figure 4.16(a) where the aggregate energy is calculated for all chains associated into clusters of various sizes by using eq. 4.3, while the separate energy is calculated for the chains in the form of unimers using the same equation. It can be seen that the breakage of the preassembled aggregate into smaller clusters leads to a decrease of the total Coulomb energy of the system, which is accompanied with the loss of surface energy and the gain

of translational entropy. At $\ell_B/\sigma = 4$, the aggregate remain intact, but the deformation of its geometric shape results in a slight increase in the total Coulomb energy, so the system probably has not reached the equilibrium state.

The total Coulomb energies in the systems with higher chain asymmetries show a general trend of decreasing with time at each given ℓ_B, indicating that the structural changes are favourable in reducing the electrostatic energy. This can be seen more clearly in Figure 4.17 for the system with $N = 320$. Therefore the separate energy remains to be zero, meaning that all 16 chains are still in connection with each other over the simulation time duration.

Apart from the symmetric case, the Coulomb energy data show that the asymmetric systems either have not reached their steady state or been trapped in meta-stable state. Therefore the simulation results we obtained so far could not lead to a solid conclusion about the aggregation behaviour of the asymmetric diblock PA chains.

4.2.4 Polyelectrolyte Stabiliser

Similar to the 2-chain cases, we can also introduce positively charged PE chains into the 16- chain systems for stabilising the aggregates. As a preliminary test, we only replace one of the asymmetric diblock chains with a PE chain of length $N_{\mathrm{PE}} = N_+ = 128$. As can be observed in 4.18, the introduction of a PE stabiliser leads to much more stable aggregates. The preassembled aggregate comprised of 15 PA chains of length $N = 320$ and one PE chain develops into a micellar structure composed of a dense micellar core and a corona constructed by long arms each having an inner helical structure and an outer single PE tail. A similar structure is also obtained for the system with highly asymmetric PA chains of length $N = 384$, where the arms are even longer.

The addition of PE stabilisers thus can potentially lead to the formation of stable
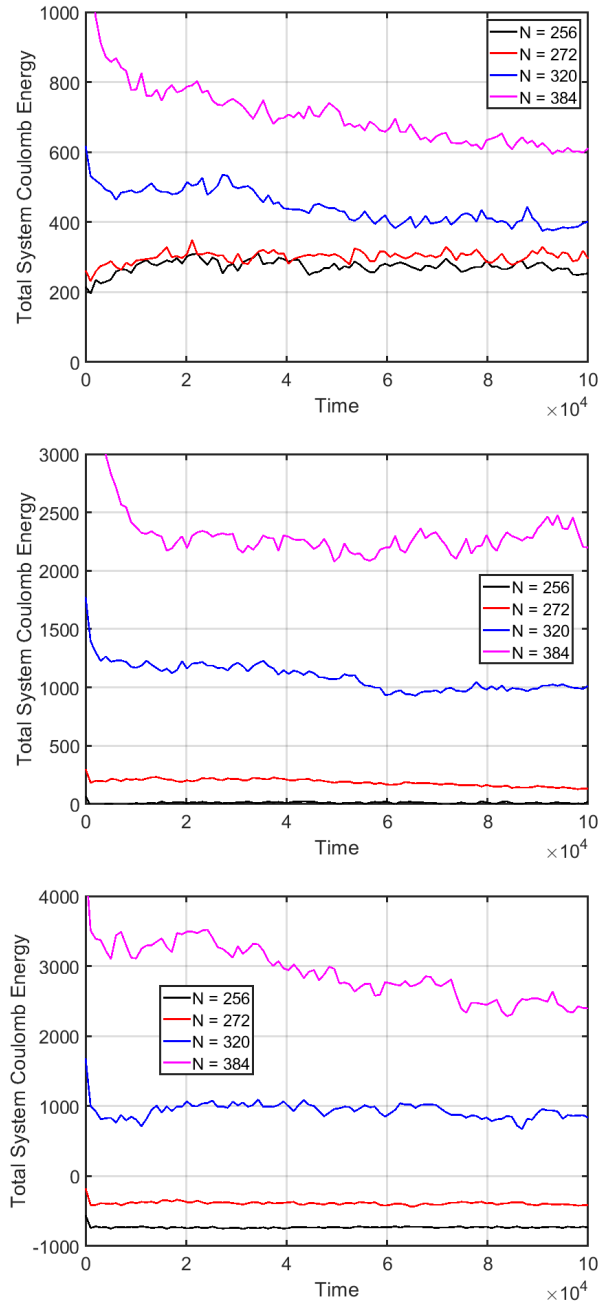
Figure 4.15: Total Coulomb energies of the systems consisting of 16 asymmetric PA chains with different chain lengths as functions of time, averaged by blocks of time. The Bjerrum lengths are $\ell_B/\sigma = 1/8$ (a), 1 (b) and 4 (c), respectively.
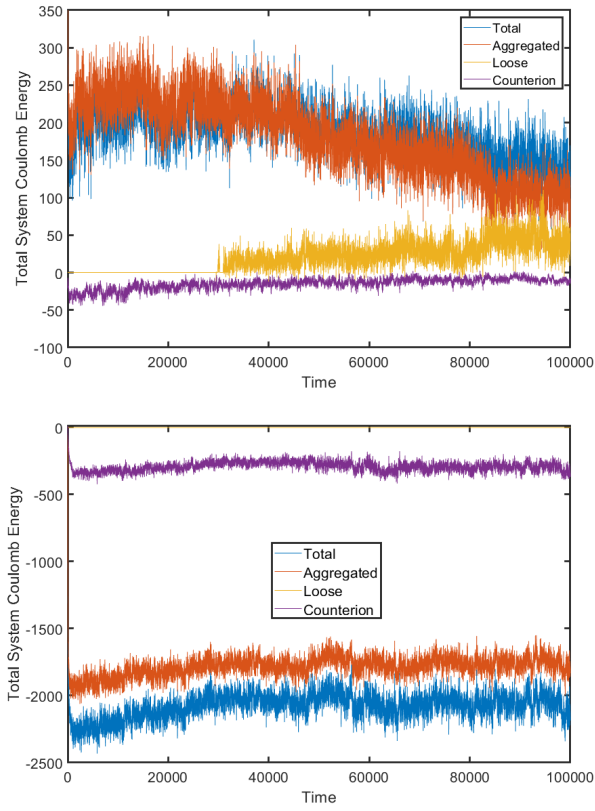
Figure 4.16: Total, aggregate and separate energies of the system consisting of 16 PA chains with $N = 272$ at Bjerrum lengths $\ell_B/\sigma = 1$ (a) and 4 (b), respectively.
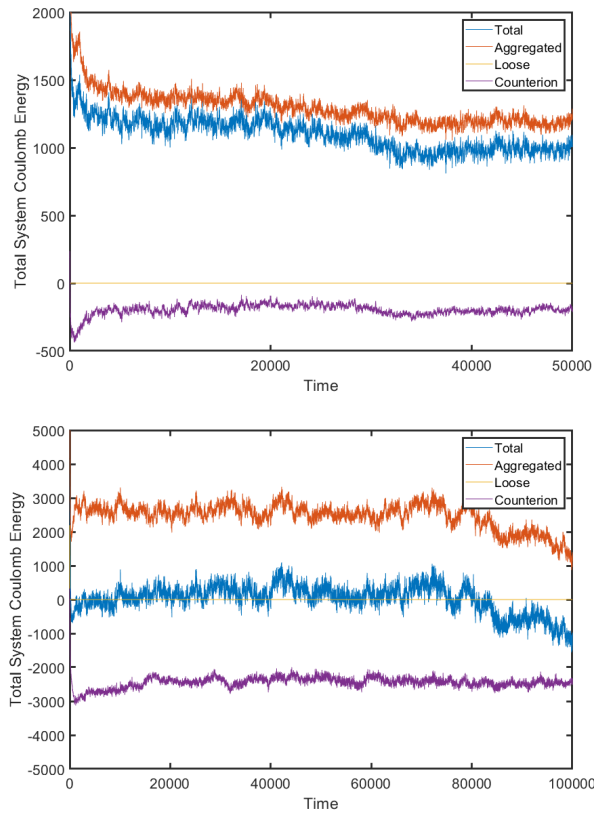
Figure 4.17: Total, aggregate and separate energies of the system consisting of 16 PA chains with $N = 320$ at Bjerrum lengths $\ell_B/\sigma = 1$ (a) and 4, respectively.

micelles in the solutions of asymmetric diblock PA chains. Further simulation runs over much longer time period are still required to study the stability of these micelle-like structures as well as the optimal length and fraction of the PE stabilisers.

4.3 Conclusions

The stability of preassembled aggregates comprised of 16 asymmetric diblock PA chains have been studied by MD simulations for different chain lengths/asymmetries and electrostatic interaction strengths. Apart from the symmetric systems where the aggregates remain intact as stable globules, the preassembled aggregates formed by asymmetric PA chains either break up into smaller clusters or evolve into complicated structures, such as star-like, hyper-branching or network structures. Coulomb energy analyses indicate that these complicated structures have not reached the equilibrium state or been trapped in meta-stable state over the simulation duration. The introduction of a single PE chain into the systems consisting of PA chains with medium to high asymmetries has been shown to result in stable micelle-like structures composed of a dense micellar core and a corona constructed by long arms each having an inner helical structure and an outer single PE tail. Further simulation runs are needed to test the stability of these micelle-like structures and understand the functioning mechanism of the PE stabilisers.
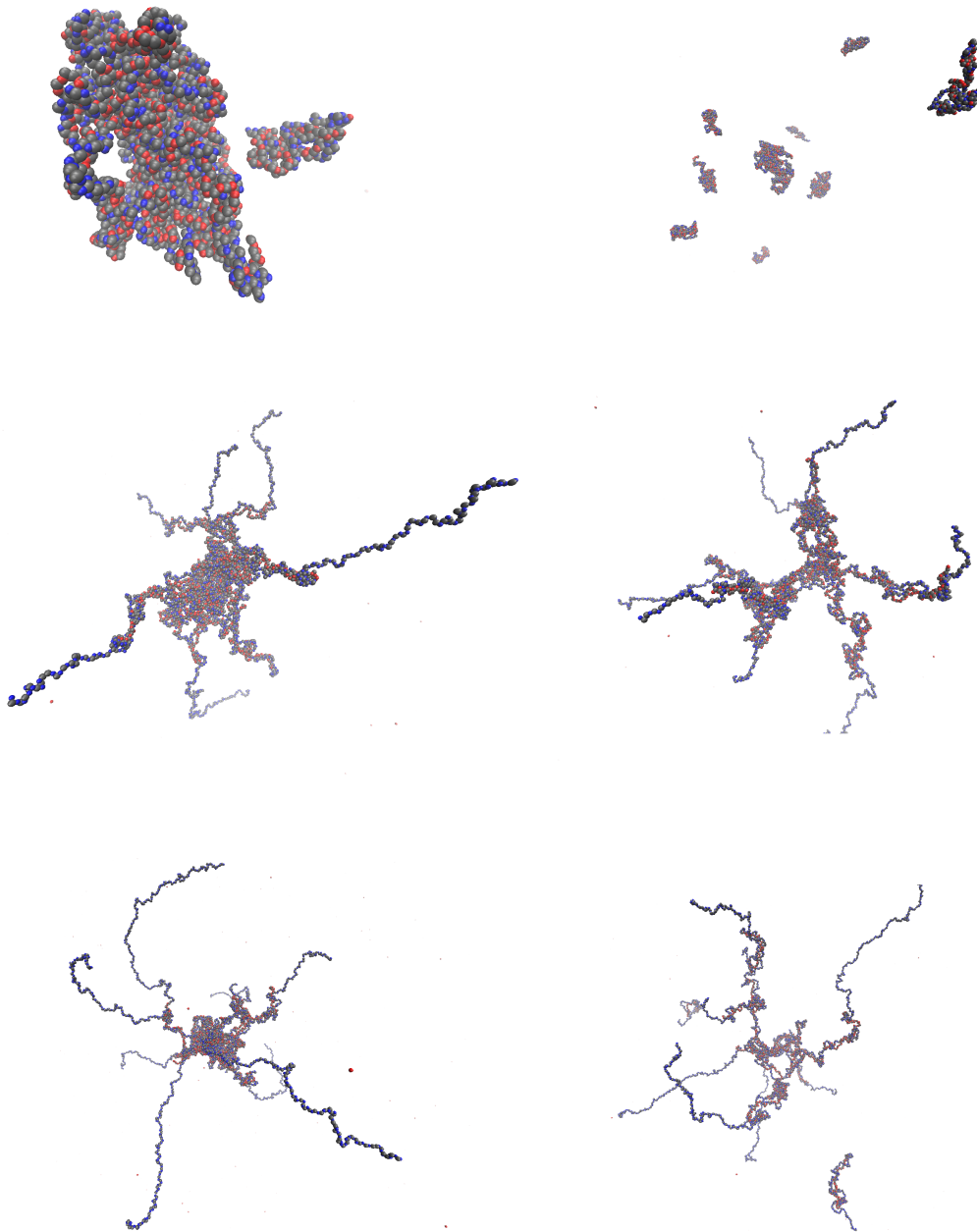
Figure 4.18: Snapshots of the systems consisting of 16 PA/PE chains taken after long MD simulation runs after switching off the drag forces. The systems on the left column are comprised of 15 asymmetric diblock PA chains and 1 PE stabiliser, and those on the right consist of 16 asymmetric diblock PA chains. The chain length increases from top to bottom as $N = \{272, 320, 384\}$. In all cases $\ell_B/\sigma = 1$.

Chapter 5

Dynamics of Ionomers

5.1 Introduction

Ionomers are flexible polymers with ionic groups covalently bonded to the chain back-bones. Different from polyelectrolytes which typically have very high ionic contents (up to the point of water soluble), they contain relatively low molar fractions ($<$ $10 - 15 mole\%$) of ionic content. The ionic groups on the chains can associate with counterions to form ionic clusters in low dielectric solvents, leading to the formation of supramolecular polymer networks [21]. The reversibility of the electrostatic bonding allows for the development of self healing or shape memory materials [1], similar to other reversible associative interactions such as hydrogen bonding [4, 5, 6, 7], metal-ligand bonding [8, 9] and $\pi - \pi$ stacking [2, 3]. These materials find numerous applications such as rheology modifiers [25], batteries [26] and suspending agents for drug delivery [27].

Charged polymer systems with very low electrostatic interaction strength show no preference for ion-counterion association and thus behave as their neutral counterparts [17]. But when the electrostatic attraction energy is strong enough to overcome en-

tropic penalty, the polymer charges and their counterions undergo pairwise bonding to form dipoles, which can further associate into multiplets with increasing electrostatic interaction strength [12]. Ionomer systems are in strong association regime where ionic clusters are formed and cross-link the precursor or parent polymers into transient networks [21]. As a consequence, chain dynamics in the ionomer systems are drastically slowed down when compared with their neutral polymer counterparts [22, 23, 24].

The factors that determine the dynamics of ionomers can be separated into two groups, namely the polymeric and electrostatic contributions. The first group includes the polymer composition, architecture and degree of polymerisation N as well as the entanglement length L_e in the system [35]. The related characteristic times are the monomer relaxation time τ_0, the chain Rouse time τ_R and reptation or terminal time τ_d. In the latter group, the important factors include the number of ionic groups (for simplicity, ions) along each polymer chain, N_s, and the electrostatic interaction strength as measured by the Bjerrum length ℓ_B. The fundamental characteristic time is the electrostatic bonding lifetime τ_b [31]. This can be extended to the so-called renormalized bond lifetime τ_b^* by considering the many breaking and re-forming events between a pair of charges before finding new association partners. [11, 29, 108]. In supramolecular systems, the simplest type of reversible association is pairwise bonding of stickers, such as binary hydrogen bonding [109, 110], which has been extensively studied both experimentally and theoretically [110, 31]. Due to the nature of charge associations, ionic clusters in ionomers can be of various sizes and structures [31]. This makes it very challenging to give an unambiguous definition of the renormalized association lifetime. Previous works reported in literature have generally treated the ion-counterion pairs or dipoles as stickers [23]. We will also refer a closely-associated pair of ion and counterion as a sticker in this chapter, but bear in mind that the ions and counterions are included explicitly in our simulations and also in the structure analysis.

The transient network formation in an associative polymer system depends on the number of stickers per chain N_s and the functionality of the stickers. If N_s is large, supramolecular networks can form even if the association of stickers is pairwise due to the presence of multiple cross links per chain [111, 23]. If N_s is small, a higher sticker functionality is required for the systems to create three-dimensional (3D) networks [112]. For instance, telechelic chains have stickers only at the chain ends [113, 114]. If the stickers associate pairwise, they undergo a head to tail association to form long linear chains [115, 116]. However an increment in the functionality from $f = 2$ to $f \geq 3$ will lead to 3D transient network formation. [112, 29]. The nature of electrostatic interactions means $f > 3$ for the stickers in ionomer systems, which apparently facilitates the formation of percolated networks.

The dynamics of associative polymers, including ionomers, can vary qualitatively depending on the relative magnitudes of N, L_s and L_e, where L_s is the length of a segment between stickers. The simplest case is $L_e > N > L_s$ where the chains are unentangled [117, 118, 23, 119]. Each sticker in associated state will add extra friction to the chain motion and so slows down its relaxation dynamics. The effective friction coefficient incurred by the associated sticker is proportional to the renormalized sticky bond lifetime τ_b^* [11, 31]. At time scales shorter than τ_b^* the system behaves as a permanent network. At larger time scales, the chain undergoes Rouse-like relaxation but with the extra frictions from the associated stickers. The Sticky Rouse model predicts the sticky Rouse relaxation time as $\tau_R \approx L_s \tau_b^*$ which is significantly larger than the standard Rouse time $\tau_R \approx N^2 \tau_0$[120]. The unentangled ionomer systems we studied fall in this situation.

The second case is $N > L_s > L_e$ where the polymers are entangled with each other and the average separation between the stickers along the chain is larger than the entanglement length. Leibler et al. studied such systems with pairwise sticker

109

associations [31, 23]. The dynamics of non-associative entangled polymers is described by the reptation or tube model [35, 40, 37]. The presence of the stickers will not affect L_e greatly, but affect the relaxation modulus at time scales larger than the entanglement time τ_e. [31] The sticky Rouse model was extended to the sticky reptation model for describing the relaxation behaviour of such entangled associative polymers by including the entanglement effects [31, 11].

The last case is $N > L_e > L_s$ where the systems consist of entangled associative polymer with the average distance between the stickers smaller than the entanglement length. The high density of stickers will alter the effective diameter of the confining tube and so change the chain dynamics greatly, leading to significant increase in both the stress plateau modulus and the terminal relaxation time. In ionomer systems, multiplets are formed by the association of ion pairs. The resulted high association energy barrier will consequently prolong the sticker lifetime τ_b^* and so the terminal relaxation time τ_d of the system. [23]

Amin et al. have performed hybrid MC/MD simulations of unentangled telechelic chains with stickers of functionality $f = 3$ [29]. They found that percolated transient networks begin to form when the association energy of stickers is around $4.3k_BT$. At higher association energy, the majority of stickers are associated into clusters which work as cross-linkers for the supramoleculer network. The dissociation of stickers from the clusters they previously belong to is dominated by a partner exchange mechanism. A phantom chain hopping model was proposed to describe the relaxation of the telechelic chains.

In this work, we study the dynamics and rheology of unentangled ionomer systems with two different types charge distributions. One group of systems are composed of monodisperse telechelic chains with a charged monomer at each chain end [31, 121] The other type of systems consist of a mixture of 50% telechelic chains and 50% chains with

110

a single charge on the central monomer, giving an average of 1.5 ions per chain. [21] The telechelic and single charged chains are of the same length and carry charges of the same sign. Counterions are added to neutralize the systems. Ion-counterion association happens at high Coulomb interaction strength, leading to the formation of percolated polymer networks and consequently slow relaxation of the ionomers in comparison with their neutral counterparts.

The rest of the chapter is organised as follows. In Section 2 we present the simulation model and the sampling techniques used in this work. The static, dynamic and rheological properties of the ionomer systems are presented and discussed in Section 3. Summaries and prospectives are given in Section 4.

5.2   Models and Methods

The polymer chains are represented by the Kremer-Grest (KG) bead-spring model which has been widely used for studying the dynamics of polymer melts [70]. In this model, the monomers interact with each other via the purely repulsive Lennard-Jones potential with the cut-off distance $r_{cut} = 2^{1/6}\sigma$. The bonding between adjacent monomers along the chains are modelled by the FENE potential with the parameters $k_{\mathrm{FENE}} = 30\sigma$ and $R_{\mathrm{FENE}} = 1.5\sigma$, which are selected to prevent the chains from passing through each other [70, 40]. The density of all particles is chosen to be $\rho = 0.85\sigma^{-3}$ as this is widely acknowledged as representative of polymer melts [70]. Counterions are included when building the periodic boundary. The entanglement length for the flexible KG bead-spring chains is estimated to be in the range of $L_e = 50 - 80$ [40, 122].

Without loss of generality, we assign monovalent positive charges to the end or middle monomers of the telechelic or single-charged chains and monovalent negative charges to the counterions. The total number of counterions in each system is thus

simply equal to the total number of charged monomers. The counterions are represented by the same type of bead as the monomers, thus have purely repulsive LJ interactions among themselves and with the monomers.

As mentioned above, two types of ionomer systems are studied, i.e., the systems containing only telechelic chains and the mixture systems consisting of half telechelic and half middle-charged chains. We choose two chain lengths, $N = 21$ and 41, to ensure the polymers are unentangled. Periodic boundary conditions are used and the Coulomb interactions are handled with the P3M method. Most of the results reported below are obtained from simulations using a total number of $N_{\text{poly}} = 100$ chains in the central simulation box. The finite size effect is investigated for a selected telechelic system by increasing N_{poly} to 200 and 400. For all studied systems, the Bjerrum lengths are changed in the range of $\ell_B/\sigma = \{0, 5, 10, 20\}$ and occasionally 40. The MD simulation time steps are accordingly varied from 0.01 to 0.001, for around 10^8 total time steps in all cases.

For each simulated ionomer system, we first equilibrate its neutral version for 10^7 time steps to ensure the chains have fully relaxed, and then turn on the charges. Due to the high electrostatic interaction strengths being used, we further employ Replica Exchange Molecular Dynamics (REMD) [71, 77] with swaps in the Bjerrum length space for a further 10^7 time steps to allow the system to access the equilibrium state. After that standard MD simulation runs are carried out for studying the dynamic and rheological properties of the ionomers, including the stress and chain end-to-end vector correlation functions as well as the monomer mean-squared displacements.

For the stress relaxation function $G(t)$, we employ the multiple-tau correlator method to calculate it on the fly in order to get good statistics [101]. For the ionomer systems, we calculate $G(t)$ both with and without the electrostatic interaction contributions for

separating the Coulombic and polymeric contributions. When these calculations were performed, we were having technical difficulty in using the P3M method to calculate the stress tensor, mainly with the Fourier space components. Therefore in the $G(t)$ results reported in this chapter, the electrostatic contributions to $G(t)$ were obtained by simply summing up the electrostatic interactions between all charges within a cut-off distance. Future work will need to include the long range contribution to the stress tensor calculation, using the equation provided in Appendix B.2. This will allow us to compare our simulation results of $G(t)$ in a more quantitative way with experimental measurements or possibly theoretical predictions (if available). It should be noted that this problem only affects the discussions about the stress relaxation in a quantitative but not qualitative way. Our simulation results for any other structure are not affected, and dynamic observables are accurate, because the MD simulations are performed using the full version of the P3M method. The k-space contribution, which contains contributions from all periodic images, is typically larger than the real-space contributions, so can not be neglected, unless the Bjerrum length $\ell_B/\sigma \ll 1$, or the simulation box is extremely large. Alternatively, the inclusion of added salt effectively screens the electrostatic interactions. In the following simulations, both the real and k-space contributions are included when calculating the electrostatic interaction forces. Therefore the structural and dynamic properties of the simulations are all calculated properly. This is in principle sufficient for understanding the microscopic relaxation mechanisms of the charged polymer systems.

The only problem is with the calculation of the stress $G(t)$. At the time when the thesis was written, we were unable to find an adequate way to include the k-space contribution to the stress. This will thus affect the quantitative accuracy of the stress, making it smaller than the actual value. However, the general variation trend and related discussions are still qualitatively valid. For more quantitative comparison

with experimental data and theoretical predictions on the rheological behaviour of the charged polymer systems, we will need to incorporate the k-space contributions. This is now possible, as suggested in recent literature [126].

5.3 Simulation Results and Discussions

Simulating small box sizes, such as in this chapter, can lead to the introduction of systematic errors, which are known as finite size effects, and one must take this into consideration when discussing the following work. To understand these errors one needs to simulate larger systems and extrapolate up to an infinite system. See Appendix B.1 for further discussion.

5.3.1 Static properties

Formation of ionic clusters and networks.

Figure 5.1 presents the snapshot of a mixture ionomer system consisting of half telechelic and half middle-charged chains with length $N = 21$ at Bjerrum length $\ell_B = 20.0\sigma$. For simplicity only charged monomers and counterions are shown. Figure 5.1(a) clearly shows that the charged monomers or ions have associated with counterions into large ionic clusters due to strong electrostatic attractions. In order to quantify the ionic cluster formation, we define a criterion that any two oppositely charged beads at a centre-to-centre distance $r < r_c = 1.4\sigma$, or equivalently at a Coulombic interaction energy $U^{\mathrm{coul}} < -\ell_B k_B T / 1.4\sigma$, are considered to be ionically bonded and belong to the same ionic cluster. By grouping all charged particles into ionic clusters interesting structural feature is observed. Whilst isolated ionic clusters do exist, the proximity of charges leads to the inter-connection of ionic clusters via strands of alternating charges
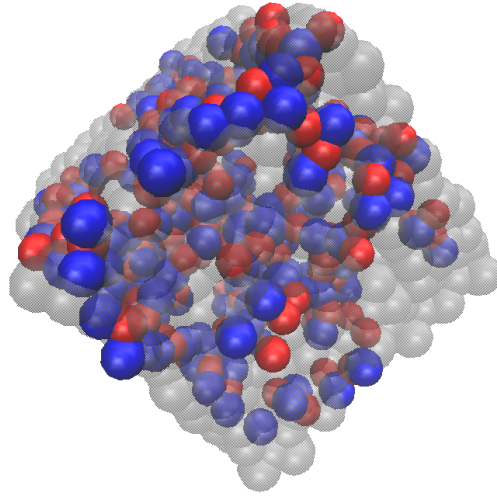
(a)
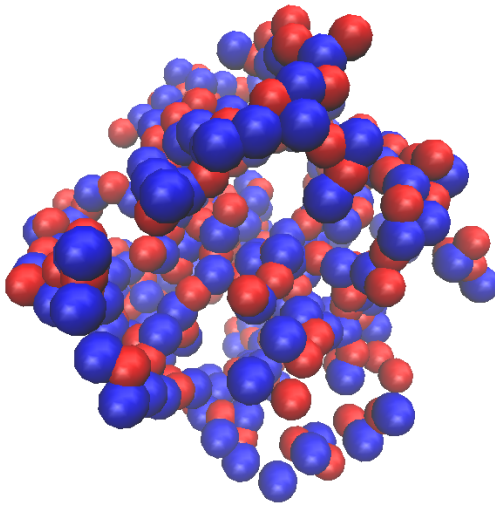
(b)

Figure 5.1: Snapshots of an ionomer system consisting of $N_{\mathrm{poly}} = 100$ telechelic chains with chain length $N = 21$ at Bjerrum length $\ell_B = 20.0\sigma$. (a) Charged monomers (ions) and counterions are in red and blue colours, and transparent grey monomers are the neutral segments;(b) Only the ions. The charges can be seen forming a large network throughout the simulation box.

to construct a percolated network that spans the entire simulation box and connects with its periodic images. This ionic network works as a scaffold to further cross-link the precursor polymer chains into a supramolecular polymer network. Such a (polymer) network on (ionic) network structure is distinctive from the transient networks generally observed in associative polymer systems with sticker functionality $f \geq 3$ where sticker clusters or micellar cores of finite sizes are bridged by polymer chains. [23, 29, 121] This can be attributed to the nature of the electrostatic interaction, which allows for formation of large ionic clusters or structures, and the high charge density in the systems of short ionomer chains. As discussed below, the ionic network provides pathways for the diffusion of the charged monomers or stickers and so facilitate the relaxation of the ionomers. If the chain length is increased, e. g. to $N = 41$, separated ionic clusters are more likely to be formed due to the reduced charge density. The relaxation mechanism would be dominated by partner exchange between individual ionic clusters, as proposed by Amin et al. [29].

One major difficulty in characterising the structural properties of ionomer systems is to define open and closed electrostatic bonds [11]. Since the electrostatic interaction energy between two charges varies smoothly with the inverse of their distance, i.e., $U^{\mathrm{coul}} \sim 1/r$, there is no clear cut-off distance r_{cut} to separate the open and close states. If the charge density is low, the ionic clusters are well separated from each other and so it is rather insensitive to the r_{cut} value used to quantify the cluster size. However, at high charge densities, the choice of r_{cut} is more delicate. Wang and Rubinstein have used $r_{\mathrm{cut}} = 1.5\sigma$ in analysing multiplet formation in diblock polyampholyte chains [12]. We have tested different cut-off values from 1.3σ to 1.6σ and found some quantitative but no qualitative differences in the ionic cluster size distribution. Therefore we choose to use $r_{\mathrm{cut}} = 1.5\sigma$ to be consistent with previous publication. Some results on the probabilities to find ionic clusters of different cluster obtained by using $r_{\mathrm{cut}} = 1.4\sigma$ are

116
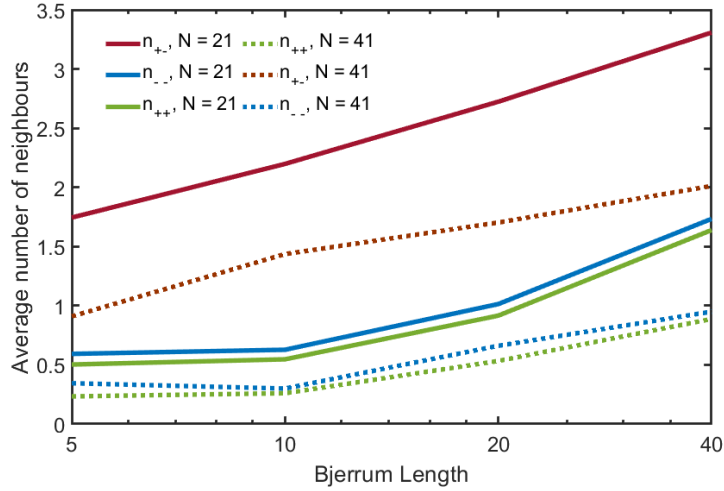
Figure 5.2: Average numbers of oppositely and likely charged neighbours per charge, n_{+-} and $n_{++,--}$ in the ionomer systems consisting of purely telechelic chains with two different chain lengths $N = 21$ (dotted lines) and 41 (dashed lines), respectively. The results are calculated using the cut-off distance $r_c = 1.5\sigma$.

also given for comparison.

Figures 5.2 presents the average numbers of neighbouring charges for the charged monomers and counterions as functions of ℓ_B in the purely telechelic chains with two different chain lengths. As the electrostatic interaction strength increases, so do the number of neighbours per charge as larger ionic clusters are formed [123, 12]. In the telechelic chain systems with $N = 41$ and $l_B = 5.0\sigma$, the average number of oppositely charged neighbours $n_{+-} \approx 1$, but those of likely charged ones $n_{++} \approx n_{--} \approx 0.2$, showing that dipole is the most prevalent association state. If all of the associated charges are in dipole format, there is no network formation. This is comparable to the case that all stickers are open [11, 29]. When the Bjerrum length is increased to $\ell_B = 20$, each ion or counterion has on average about 1.5 oppositely charged and 0.5 likely charged neighbours. This is evidence of larger multiplet formation. The values of $n_{+-,++,--}$ all grow with the decrease of chain length from $N = 41$ to 21 and also are higher in the systems of purely telechelic chains than in the mixtures owing to higher
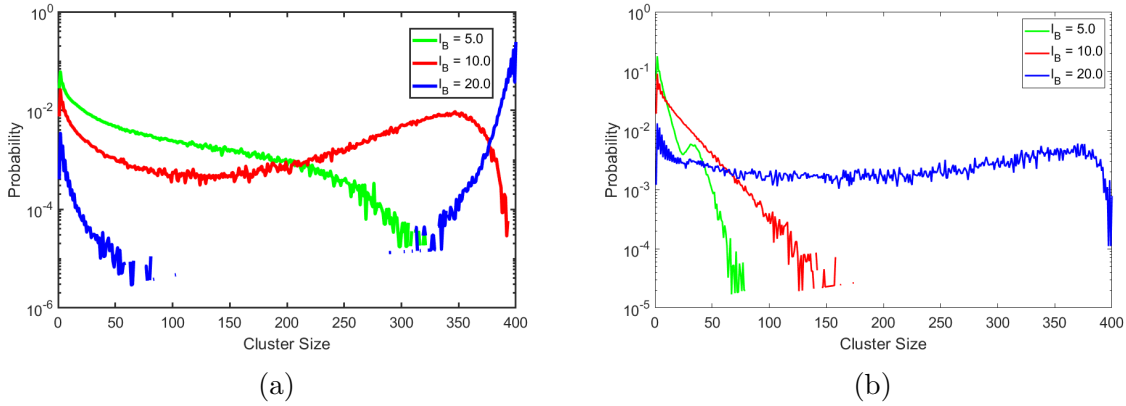
Figure 5.3: Probability density for finding a charged particle (ion or counterion) to be in an ionic aggregate of size N_c formed in the ionomer systems consist of purely telechelic chains with length $N = 21$ (a) and 41 (b) at various l_B values. There are a total $N_p = 100$ chains in each system. The results are calculated using the cut-off distance $r_c = 1.5\sigma$.

charge densities.

Distribution of Cluster Sizes

Figures 5.3a and 5.3b present the probability density for finding a charged particle (ion or counterion) to be in an ionic aggregate of size N_c formed in the ionomer systems consist of purely telechelic chains with two different lengths, respectively. The results are calculated using the cut-off distance $r_c = 1.5\sigma$. For comparison, Figures 5.4a to 5.5b present similar sets of data for both the systems consisting of purely telechelic chains and of mixtures of half telechelic and half middle-charged chains, but calculated using $r_c = 1.4\sigma$. It can be seen that the results are qualitatively insensitive to this change of r_c. In Figures 5.4a to 5.5b, simulation results on the probability density for the largest ionic cluster formed in each ionomer system to be of a certain size are also given. At each given ℓ_B the two types of probabilities show similar variation trend in the region of relatively large cluster sizes where the weight of the largest cluster dominates. Consistent with the results in Figure 5.2, the probabilities to form large

118
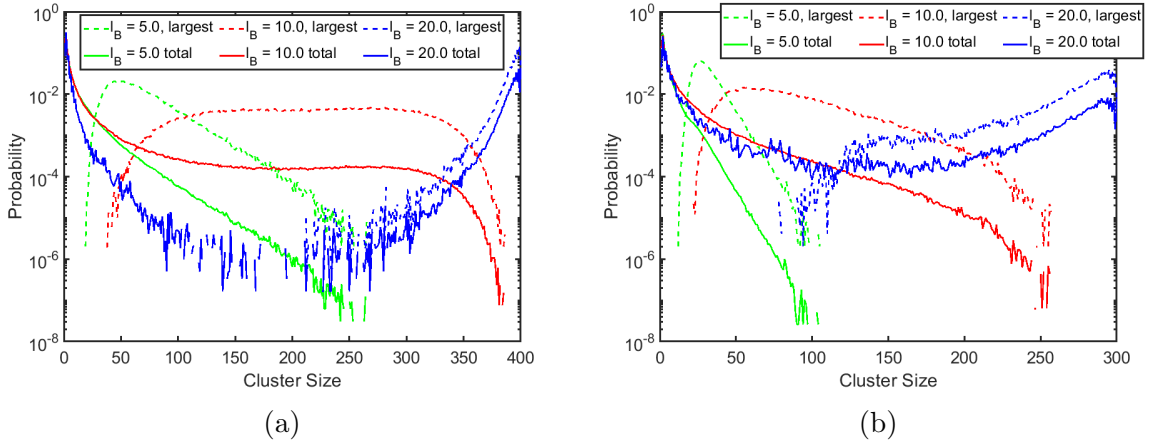
Figure 5.4: Probability densities for finding a charged particle in the largest (dashed lines) or any (solid lines) ionic cluster of size N_c. Here the ionomer systems consist of (a) purely telechelic chains and (b) half telechelic and half middle-charged chains with chain length $N = 21$ at various l_B values. There are a total $N_{\text{poly}} = 100$ chains in each system. The results are calculated using the cut-off distance $r_c = 1.4\sigma$.
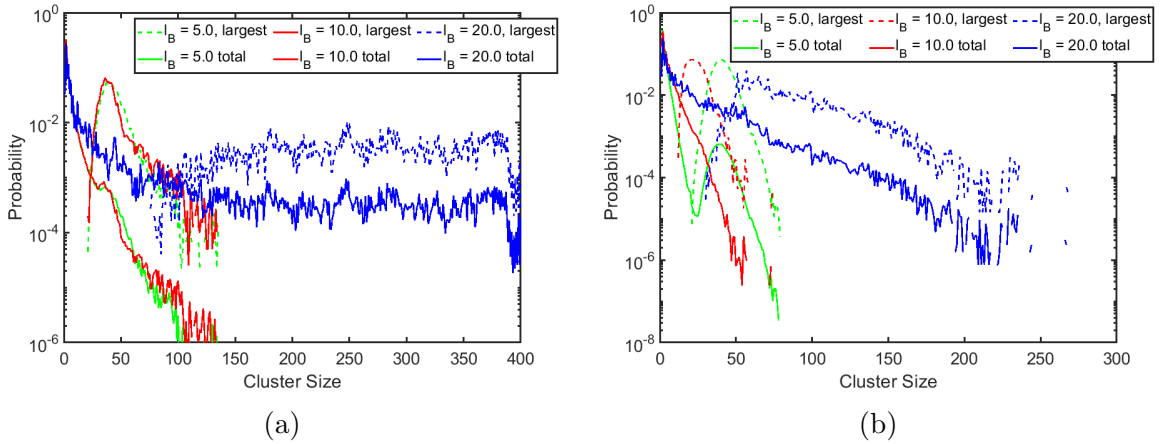
Figure 5.5: Probability densities for the largest (dashed lines) or any (solid lines) ionic cluster in the system to be of size N_c. Here the ionomer systems consist of (a) purely telechelic chains and (b) half telechelic and half middle-charged chains with chain length $N = 41$ at various l_B values. There are a total $N_{\text{poly}} = 100$ chains in each system. The results are calculated using the cut-off distance $r_c = 1.4\sigma$.

119

clusters increase with the decrease of the chain length and also is higher in the systems consisting of purely telechelic chains than in the mixture systems. The most probable size of the largest cluster in a given system also shifts to higher value with the increase of the electrostatic interaction strength. For the purely telechelic system with $N = 21$, the probability to have large clusters (> 10) at $\ell_B = 5\sigma$ is exponentially low. But at $\ell_B = 20.0\sigma$, the cumulative probability to form large ionic structure involving more than half, even all, of the charges in the system is over 50%. This supports the formation of a percolated ionic network that involves the majority of charged particles in the system and spans the entire simulation box. The wide distribution of N_c indicates the coexistence of ionic clusters of finite sizes and the percolated network, as well as the reversible feature of the ionic network with frequent association and dissociation of ions and counterions. Such a percolated structure becomes unlikely in the mixture system with chain length $N = 41$ due to the lower charge density, as shown in Figure 5.5b.

Characterising association states of charges

Here we analyze the ionic aggregates in more details. We define a *loose ion* as a charged monomer having zero charged neighbours and a *dipole* as a pair of associated ion-counterion. An *ionic strand* is a linear sequence of alternatively arranged ions and counterions. An ion or counterion belongs to an ionic chain or strand if it has two oppositely charged neighbours but no likely charged neighbour. A *loose end* is the end of a strand that does not connect to another structure. Such an end ion or counterion has only one oppositely charged neighbour, but that neighbour has two oppositely charged neighbours. Furthermore we consider an ion or counterion as part of a multiplet, which could be an ionic cluster of finite size, a junction point for the ionic strands, etc.

Figure 5.6 presents the fractions of charged particles to be in different association states for the systems consisting of purely telechelic chains with length $N = 21$ and 41,
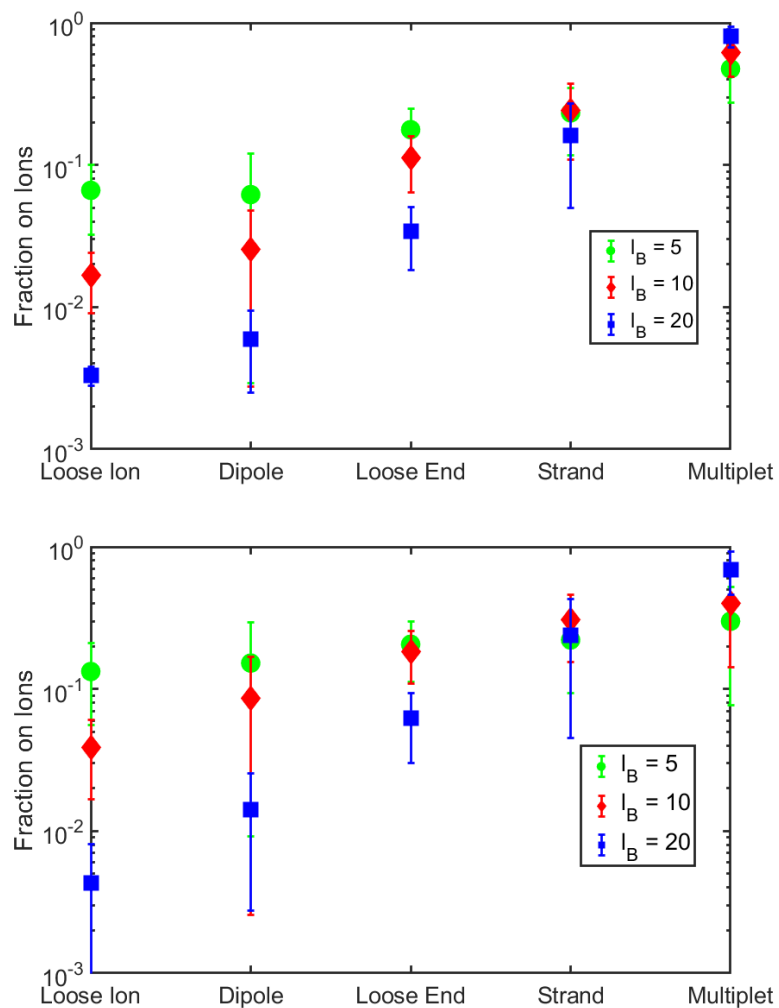
Figure 5.6: Fractions of charged particles to be in different association states for the ionomer systems consisting of purely telechelic chains with length $N = 21$ (a) and 41 (b), respectively. The results are calculated using cut-off distance $r_c = 1.5\sigma$.
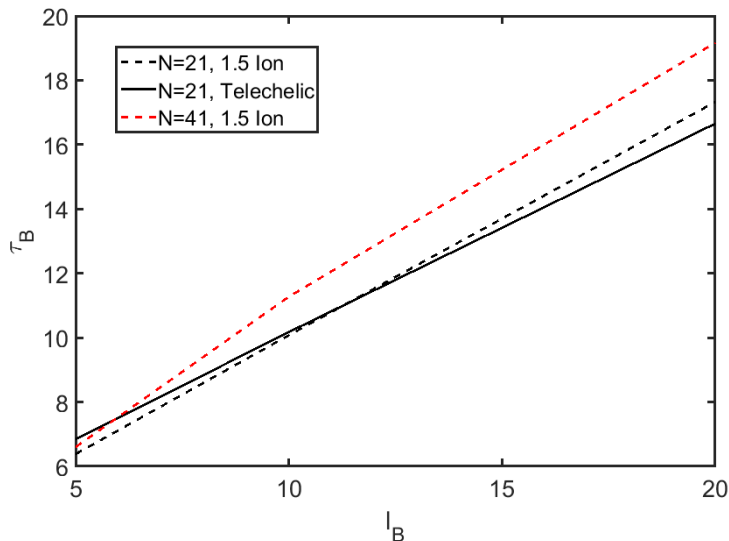
Figure 5.7: Average renormalised lifetime of the electrostatic bonds formed between charged monomers and counterions as a function of Bjerrum length.

respectively. With the increase of the Bjerrum length, the fractions of loose ions and dipoles decrease, but those in the multiplets increase, indicating larger ionic aggregates are formed at high ℓ_B. For a given ℓ_B, the fraction of charges in multiplets in the systems with shorter chains or higher charge density is larger than that in systems with longer chains or lower density. The number of loose ends is shown to decrease with increasing ℓ_B and decreasing chain length, indicating that the ionic strands have been connected to multiplets to form either large ionic clusters or a transient ionic network. Based on the understanding of the structural properties, we investigate the dynamics of the ionomer systems below.

5.3.2 Dynamic and Rheological Behaviour

Lifetime of ionic bonding

The dynamics of associative polymers strongly depends on the lifetime τ_b of the reversible sticky bonds. In systems where the sticky bonds are formed by pairwise associ-

ation of stickers, it is relatively unambiguous to define τ_b of a sticky bond according to the association/disassociation state of the two involved stickers. [11, 124, 29, 108, 125] However, the problem becomes much more difficult in the ionomer systems. In principle one can treat pairs of associated ion-counterion or dipoles as stickers and calculate the bonding lifetime between two associated dipoles as τ_b. [23] But the dipoles are not fixed, both the ions and counterions can change their associated partners. This happens with very low probability for isolated dipoles, but is more likely in the multiplets or larger ionic structures as the counterions can move easily within the ionic aggregates without incurring any energy penalty, making it impractical to track the association state of the original dipole. Therefore we choose to determine the electrostatic bond lifetime using the association states of the charged monomers. This choice is reasonable because the formation of the transient polymer network and the relaxation of the studied ionomer chains are both realised via the counterion mediated association/dissociation of the charged monomers within or from the ionic aggregates.

We first calculate the average lifetime of the electrostatic bonds formed between the charged monomers and the associated counterions. An ion-counterion bond is considered to be broken if the charged monomer moves beyond a distance of 1.4σ from the counterion. Similar to the sticky bonds studied in other associative systems, [11, 124, 29] such an electrostatic bond will also experience many breaking and reforming events before eventually leave each other. To find the renormalised bond lifetime, we determine an initial, approximate bond lifetime τ_b. This lifetime tracks just the first time two monomers are a distance 1.4σ apart, then τ_b registers a break of the bond and records a dissociation. The issue with this is that the ions may in fact still be associated, and may come back to within 1.4σ quickly enough that we should disregard this association breakage, and as such we need to adjust the lifetime accordingly. We perform an initial run and record τ_b and use this as our basis. In future analysis runs,

if two ions return to within 1.4σ in a time less than τ_b, then we consider the bond has having never broken and continue to count the bond lifetime and construct a new, more realistic renormalised average bond lifetime τ_b^*.

Figure 5.7 presents the average renormalised bond lifetime τ_b^* between the charged monomers and counterions for three ionomer systems. τ_b^* increases with the increase of ℓ_B in all three systems as expected, but the growth trend is rather linear than exponential. More interestingly, at high ℓ_B, the calculated bond lifetimes are lower in the systems with higher charge densities, i.e., those consisting of purely telechelic chains and/or with shorter chain lengths. It should be noted that these data are calculated over all charged monomers, regardless of the ionic aggregates they associate with. They are neither the average lifetime of the isolated dipoles nor the average time for a charged monomer to stay within an ionic aggregate before breaking off. The average lifetime of isolated ion-counterion pairs or dipoles would grow exponentially as $\sim \exp(\ell_B k_B T/\sigma)$. As shown in Figure 5.6 the number of charges in isolated dipoles is much smaller than those in large ionic aggregates. The probability for a single charge to break off from the ionic aggregate is also exponentially low due to the high energy barrier. It is energetically more favourable for the ion and counterion to break off in pairs.

Consider a closely-packed square-shape quadrupole formed by two positive and two negative charged beads of the same size σ and same absolute unit charge. Its total electrostatic energy is $U_{\text{coul}}^{quad} = (\sqrt{2}-4)l_B k_B T/\sigma$. The energy penalty for it to break into two dipoles each of energy $-l_B k_B T/\sigma$ is $(2-\sqrt{2})l_B k_B T/\sigma <\approx 0.59 l_B k_B T/\sigma$, which is lower than that required for one charge to break off, $(2-1/\sqrt{2})l_B k_B T/\sigma \approx 1.29 l_B k_B T/\sigma$. The electrostatic penalty for a dipole to break off a closely-packed cubic-shape octupole is $(4 + 2/\sqrt{3} - 3\sqrt{2})l_B k_B T/\sigma \approx 1.39 \ell_B k_B T/\sigma$. The results in Figure 5.7 can not be interpreted as a measure of the break-off time scales of dipoles from ionic aggregates which should also follow the exponential dependence on $\ell_B k_B T/\sigma$.

124

The weak dependence of τ_b^* on ℓ_B indicates that the change of counterion partners does not only take place by the dissociation of charged monomers from the ionic aggregates, but also by the motion of the counterions and the charged monomers themselves inside the aggregates. The latter process is more convenient in the ionic clusters of large sizes and also in the ionic networks. This explains why at a given ℓ_B the τ_b^* value decreases with the increase of charge density. The diffusion of the charged monomers and counterions in the large ionic clusters and networks thus provides a relaxation pathway for the ionomers, which is energetically more favourable than the sticker hopping process purposed for the transient networks formed by inter-linked sticker clusters [124, 29]. This relaxation mechanism is most significant in the ionomer systems composed of unentangled chains with few ionic groups per chain, such as the telechelic chain systems where large ionic structures can be formed and the chain dynamics is controlled by the motion of the charged end monomers. In systems consisting of entangled chains and/or high charge per chain, the motion of the ionic groups are restricted by topological constraints and the bonding states of neighbours ionic groups along the chain, and so can only affect the local chain segment relaxation. In the latter case, the sticky Rouse or sticky reptation model become dominant.

The partner exchange mechanisms purposed by Amin et al. [124, 29] should also play an important role in the relaxation of the ionomer systems we studied. This can be seen from the fluctuations in the ionic aggregate sizes, corresponding to frequent association and dissociation events of the ionic clusters which enables the charged monomers to exchange their partners and so facilitate the ionomer chain relaxation.

There are thus at least three possible relaxation processes in the unentangled ionomer systems with high charge density, namely charge or dipole hopping, partner exchange and charge diffusion inside large ionic clusters or networks. The latter two mechanisms are energetically more favourable. The chain relaxation dynamics is thus faster than
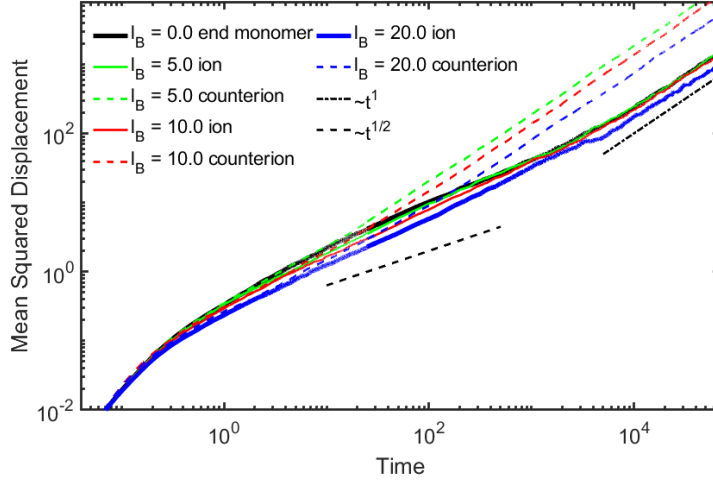
Figure 5.8: Mean squared displacements of charged end monomers and counterions in the systems consisting of purely telechelic chains with chain length $N = 21$ at different Bjerrum lengths ℓ_B.

that would be expected in the supramolecular polymer networks formed by ionomer or associative polymers cross-linked by sticker clusters of finite sizes.

Diffusion behaviour of charged monomers and counterions

Figure 5.8 presents the mean squared displacement (MSD), $g_1(t)$, for the charged end monomers and their counterions in the systems consisting of purely telechelic chains with chain length $N = 21$ and different Bjerrum lengths. At very short time scales, the monomers are not aware of the chain connectivity and ionic binding, so their MSDs follow the same universal behaviour as those of the counterions. These curves separate from each other at $t > \tau_0$. The diffusion of ions/counterions in the systems with higher l_B becomes slower due to the formation of larger ionic aggregates. In each ionomer system studied, the MSDs of the charged end monomers and counterions grow with time very closely to each other until reaching the time scale comparable to the renormalised ionic bonding lifetime τ_b^*, indicating that they are moving together in pairs

or dipoles before that. After this characteristic time, the counterions diffuse much faster and enter the free diffusion regime at earlier time. The diffusion coefficients of the counterions decrease with increasing ℓ_B as $D^*_{\text{counter}} \sim \{0.0317, 0.0230, 0.0128\}$ for $\ell_B/\sigma = \{5.0, 10.0, 20.0\}$. This can be attributed to the enhanced effective friction they experienced due to the strong electrostatic attractions from the oppositely charged monomers at larger ℓ_B. Compared with the counterion diffusion that is very sensitive to ionic binding, the diffusion of the charged end monomers is controlled by combined effects of the polymeric behaviour and the ionic binding. The MSDs of these monomers enter the free diffusion regime at time scales consistent with the terminal stress relaxation time of the ionomer chains as discussed below. Their diffusion coefficient, D^*_{end}, also decrease with increasing electrostatic interaction strength, but at a smaller relative magnitude or decaying rate, because the polymeric behaviour is still playing an important role even at the largest ℓ_B studied. For the telechelic chains with $N = 21$, our simulations find $D^*_{\text{end}} \sim \{3.7 \times 10^{-3}, 3.7 \times 10^{-3}, 3.3 \times 10^{-3}, 2.6 \times 10^{-3}\}$ for $l_B/\sigma = \{0.0, 5.0, 10.0, 20.0\}$. The D^*_{end} values obtained at $\ell_B = 5\sigma$ and 10σ are not significantly different from that of the end monomers of non-associative neutral chains, even though the MSDs of these systems are clearly distinguishable at intermediate time scales as shown in Figure 5.8.

To have a better picture about the diffusion behaviour of the charged end monomers, we compare their MSDs with certain monomers in the neutral chains of the same length in Figures 5.9a to 5.10 for the systems consisting of telechelic chains with $N = 21$ at different ℓ_B values, respectively. Please note that the results here are presented with different axis views to highlight the behaviour discussed in the following. For a complete overview, see Figure 5.8. In Figure 5.9a, the MSDs of the charged end monomers and counterions obtained at $\ell_B = 5\sigma$ are compared with those of the end monomers and the monomers right next to the end ones, termed as *end-1*, of the

neutral chains. A close inspect reveals that at intermediate time scales, the MSD of the counterions nearly coincide with that of the neutral chain end monomers, and the MSD of the charged end monomers grows closely to that of the neutral chain *end-1* monomers. This is evidence that almost all of the charges are associating into dipoles. The ionically bonded counterion effectively behaves as the end monomer of the telechelic chain, while the charged end monomer turns into the one next to the end and so experiences higher friction. This trend terminates around the renormalised lifetime τ_b^* of the ionic bonds. After that the charged end monomers enter the free diffusion regime with similar diffusion coefficient as that of the neutral chain end monomers. The results in Figure 5.9a thus indicate that at a Bjerrum length of $\ell_B = 5\sigma$ the diffusion behaviour of the charged end monomers are mainly affected by their pairwise bonding with counterions. Since the larger ionic clusters formed at this ℓ_B value are still subject to large fluctuations, allowing the charges to exchange partners both inside the clusters and with other clusters, they do not impose a significant hindrance to the diffusion of the charged monomers.

When ℓ_B is increased to 10σ, the MSD of the charged end monomers is shown in 5.9b to behave similarly to that of the middle monomers of neutral chains with $N = 41$ until time scales around $\sim \tau_b^*$. It implies that at this electrostatic interaction strength the ionic pairs or dipoles have associated into quadrupoles or higher order multiplets to connect the ionomers into longer chains, in a manner of head to tail association [115]. The diffusion of the charged end monomers is slightly slower than middle monomers of the long chains due to the additional friction of associated counterions. Even at $\ell_B = 10\sigma$ the ionic pairs and individual charges can still undergo intra- and inter-cluster partner exchanges without overcoming high energy barrier [29]. This exchange process adds an effective friction to the charged monomers and leads to a diffusion coefficient smaller than that of the neutral chain end monomers.

128
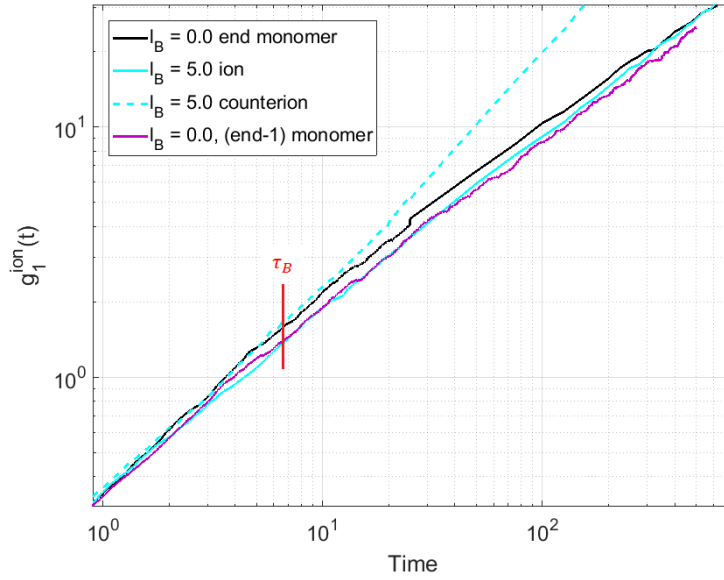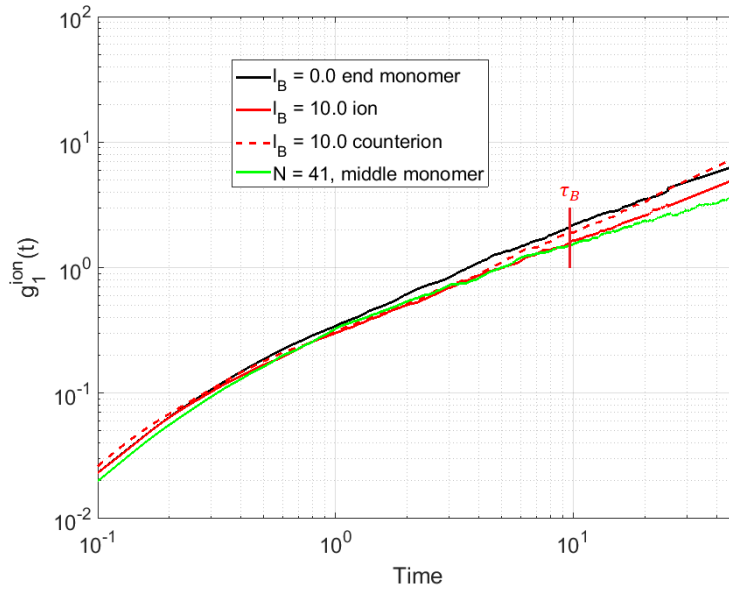
Figure 5.9: Mean squared displacements of charged end monomers and counterions in the ionomer systems consisting of purely telechelic chains with length $N = 21$ at Bjerrum lengths $\ell_B = 5\sigma$ (a) and 10σ (b), respectively. For comparison, we have also included the MSD data of the chain end monomers (in (a) and (b)) and the (*end-1*) monomers right next to the end ones (in (b)) obtained from MD simulations of the neutral chain melt with $N = 21$. Also included in (b) are the MSD of chain middle monomers obtained in the neutral chain melt with $N = 41$. Results are presented with different axis to highlight specific behaviour.

Figures 5.3a and 5.4a indicate that large ionic clusters and even percolated ionic networks are formed at $\ell_B = 20\sigma$. The strong electrostatic interaction energy leads to tight bonding of the opposite charges. The diffusion of the charged end monomers is significantly slowed down when compared with the end monomers of neutral chains of the same length in Figure 5.10. But there is no visible caging effect in the MSD curve. It means that the charged monomers and counterions inside the large ionic structures are still mobile but subject to higher effective frictions. Their diffusion behaviour at intermedia time scales can be mimicked by introducing a high friction coefficient, $\xi_{\text{end}} = 30.0\xi$, to the end monomers of neutral chains of the same length and also some single beads in the corresponding neutral chain melt, see Figure 5.10. The discrepancy happens after the average bond lifetime τ_b^*.

Our simulation results on the diffusion behaviour of the charged monomers and counterions indicate that the formation of ionic clusters and transient networks can slow down the diffusion of the charged objects, but do not lead to a strong caging effect, at least not for the Bjerrum lengths we studied. The associated charged monomers and counterions are still mobile and can diffuse long distances due to the intra- and inter-cluster partner exchange events which do not incur strong energetic penalty.

5.3.3   Relaxation correlation functions

The relaxation dynamics of the polymer chains can be characterised by the end-to-end vector correlation function $\Phi(t) = \langle \mathbf{R}_e(t) \cdot \mathbf{R}_e(0) \rangle / \mathbf{R}_e^2(0)$ where $\mathbf{R}_e$ is the end to end vector of a polymer chain, and the relaxation of whole system can be measured by using the stress relaxation function $G(t)$ (eq. 1.12) . In order to separate the polymeric and electrostatic contributions to the stress relaxation, we have calculated $G(t)$ both without and with the contributions from electrostatic interaction among charge objects.
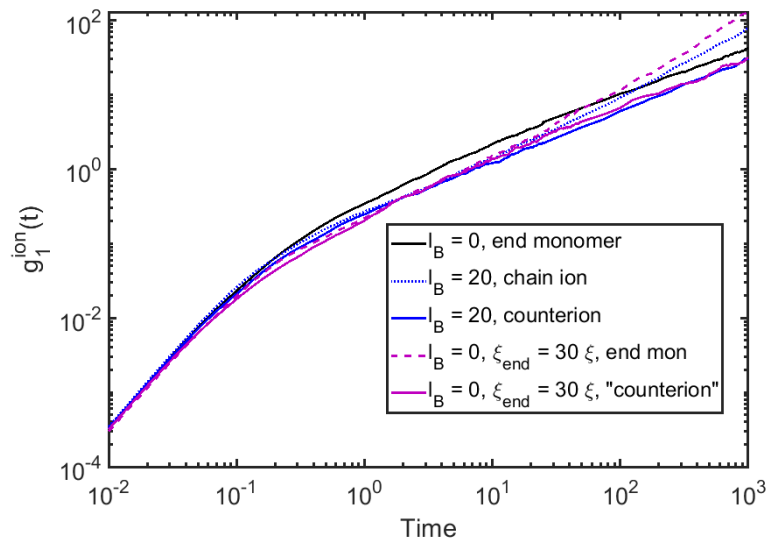
Figure 5.10: Mean squared displacements of charged end monomers and counterions in the ionomer systems consisting of purely telechelic chains with length $N = 21$ at Bjerrum lengths $\ell_B = 20\sigma$ For comparison, we have also included the MSD data of the end monomers of neutral chains of the same length and some single beads in this neutral chain melt where 30 times higher frictions are applied to the end monomers and single beads than other monomers.

For the results presented in this chapter, the electrostatic part of $G(t)$ only contains the real-space interaction contributions as calculated in the P3M method. The Fourier space contributions are discussed in future work section. Since the MD simulations themselves are performed using the full version of P3M, neglecting the Fourier space contributions only affects the quantitative but not qualitative discussions.

Figures 5.11 and 5.12 present our simulation results on $\Phi(t)$ and $G(t)$ of the ionomer systems consisting of purely telechelic chains with lengths $N = 21$ and 41, respectively. Simulation data obtained from neutral chain melts are also included for comparison. At each given chain length, both the $\Phi(t)$ and $G(t)$ data demonstrate the delayed relaxation behaviour with the increase of the electrostatic interaction strength. The delay behaviour become evident at $\ell_B \geq 10\sigma$, in consistence with the MSD data in Figure 5.8. The $\Phi(t)$ curves reflect that the terminal regime has been reached in the simulations for ℓ_B up to 20σ for both chain lengths, even though large ionic structures have been formed in these systems. This can be attributed to the fluctuation-induced intra- and inter-cluster partner exchange processes which allow the charged end monomers of the chains to move long distances, rather than being trapped. The terminal time of the chain end-to-end vector relaxation, τ_d^{ee}, is larger than the terminal stress relaxation time τ_d^{stress} for each system studied. This relation is expected for polymeric materials, e.g., $\tau_d^{ee} = 2\tau_d^{stress}$ for Rouse chains.

The $G(t)$ data with and without electrostatic interactions show that at smaller ℓ_B the polymeric contribution dominates, while at larger ℓ_B the electrostatic contributions become more essential. When $\ell_B \geq 20\sigma$, $G(t)$ with electrostatic contributions shows more viscous behaviour, owing to strong electrostatic interactions inside the large ionic structures. There seems to be no clear plateau region in the simulated $G(t)$, which is somewhat different from the experimental results on mono disperse unentangled telechelic ionomers [121]. At least in our simulation systems, the fluctuation-induced

partner exchange processes inside and between the ionic clusters play an important role in facilitating the chain and stress relaxations. This can be seen partly by comparing the $\Phi(t)$ and $G(t)$ data obtained at the two different chain lengths. At small ℓ_B, the polymeric contributions lead to slower relaxation of the system with longer chains as expected. But at larger ℓ_B, even though larger ionic clusters and also ionic networks are formed in the shorter chain systems due to higher charge density. The $N = 41$ systems also present large clusters, although smaller than the $N = 21$ systems. A plot of $G(t)$ against t/N^2 is presented in Figure B.2. There are no large separations between the ionic clusters in either system to reduce the probability for the clusters to meet each other and exchange partners, it is fairly easy for them to do so. The ionic clusters are much closer to each other in the shorter chain systems. They may even be connected into percolated networks. The charged monomers can thus diffuse along the continuous pathways of the network without encountering high energy barriers.

The stress relaxation results of the mixture systems presented Figures 5.13 show qualitatively similar behaviour to those of the pure telechelic chain systems. The quantitative differences arise from the different compositions of the ionomers which lead to different microstructure formation under electrostatic iterations

5.4   Conclusions

Molecular dynamics simulations have been performed to study the static and dynamic properties of unentangled ionomer systems consisting of either purely telechelic chains with charged end monomers or mixtures of half telechelic and half middle-charged chains. Two different chain lengths $N = 21$ and 41 have been studied, both are well below the entanglement length. The effect of electrostatic interactions is examined by varying the Bjerrum length ℓ_B over a wide range from 0 to 40σ.
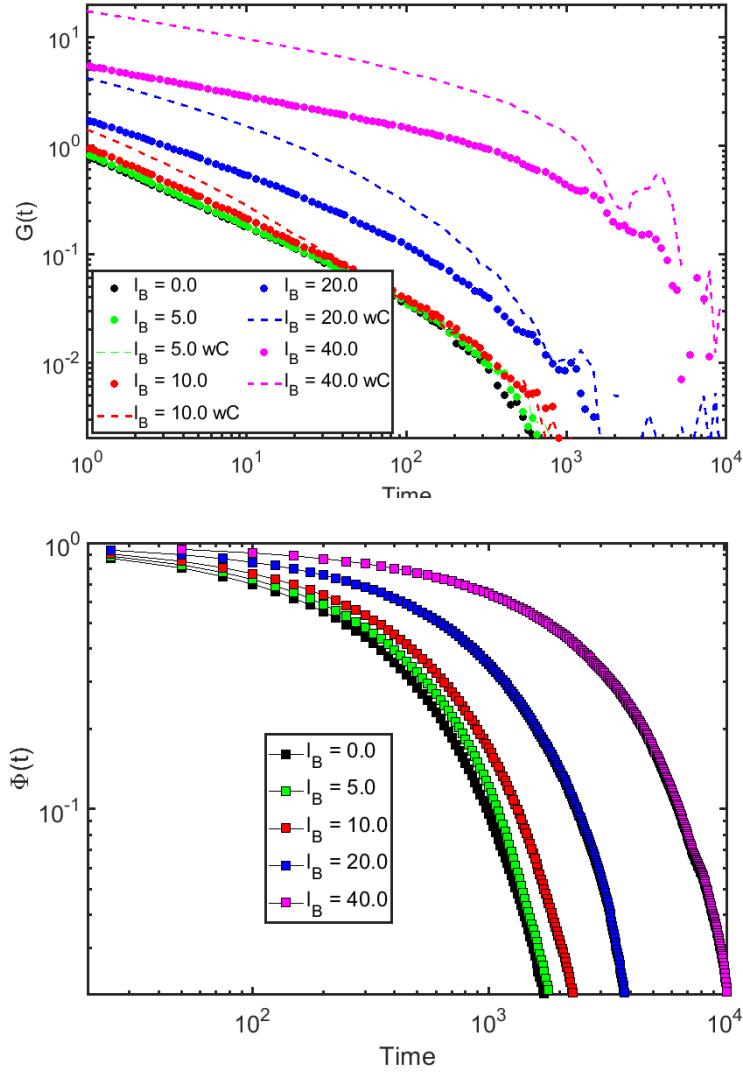
Figure 5.11: (a) Stress Relaxation function $G(t)$ for the systems consisting of purely telechelic chains with length $N = 21$. The $G(t)$ data are presented both without (thick circles) and with (dashed lines) electrostatic contributions; (b) End-to-end vector correlation functions of the telechelic chains in the systems of purely telechelic chains with length $N = 21$ at different Bjerrum lengths.
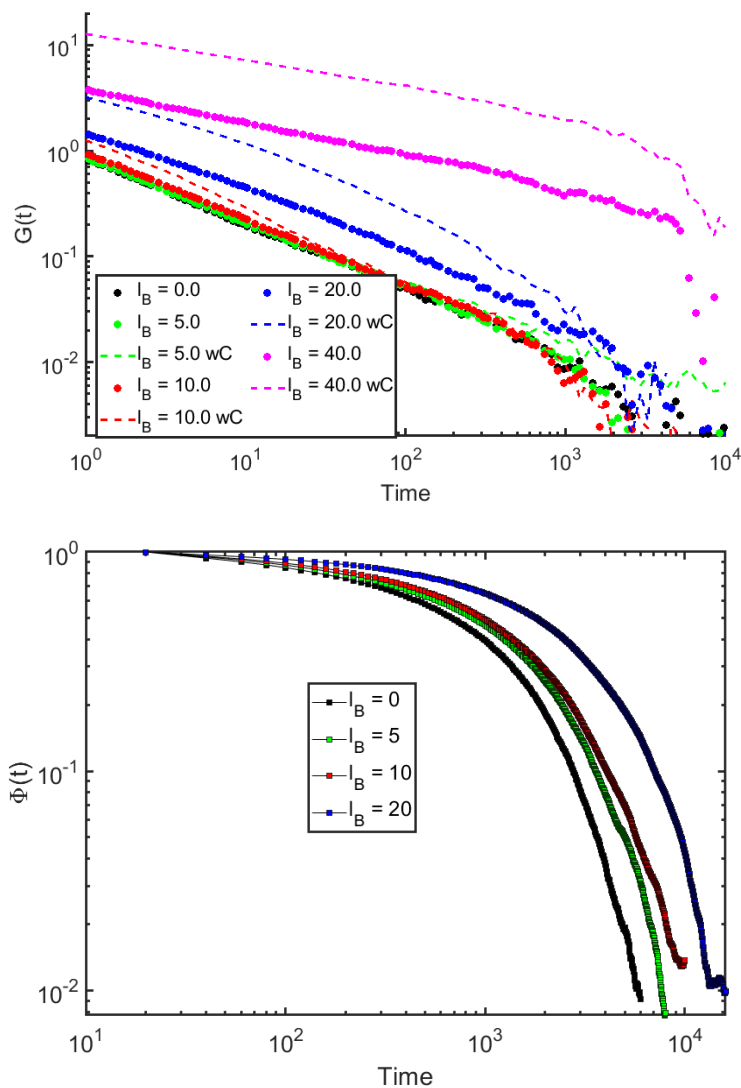
Figure 5.12: (a) Stress Relaxation function $G(t)$ for the systems consisting of purely telechelic chains with length $N = 41$. The $G(t)$ data are presented both without (thick circles) and with (dashed lines) electrostatic contributions; (b) End-to-end vector correlation functions of the telechelic chains in the systems of purely telechelic chains with length $N = 41$ at different Bjerrum lengths

135
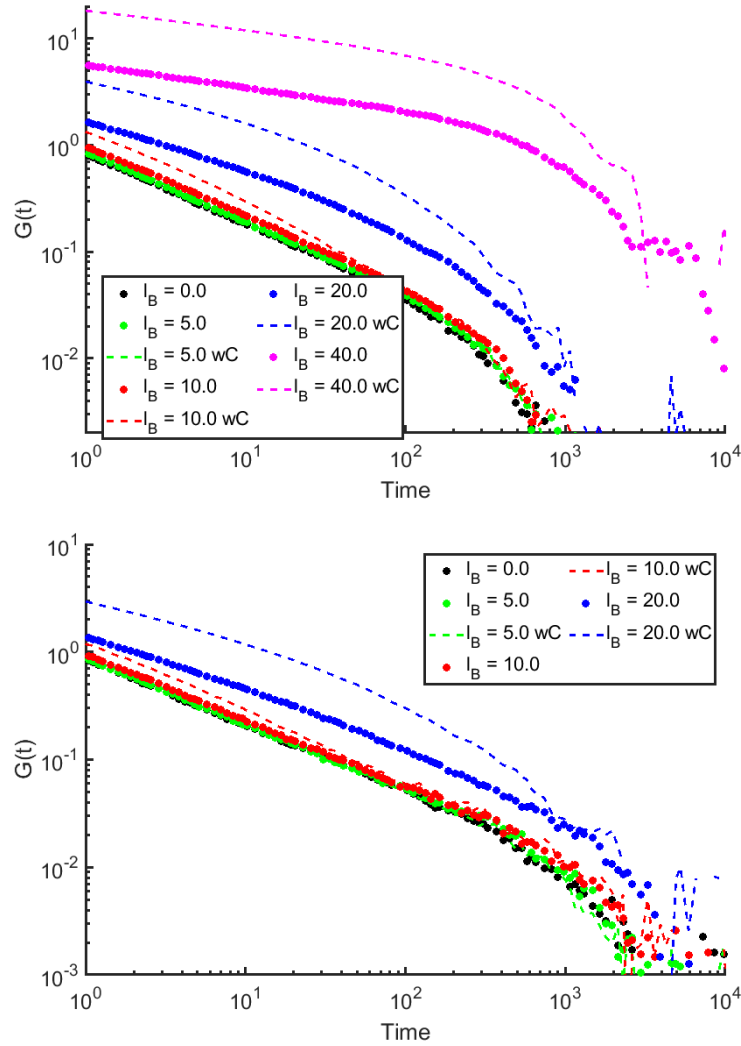
Figure 5.13: Stress Relaxation function $G(t)$ for the systems consisting of half telechelic and half middle-charged chains with lengths $N = 21$ (a) and 41 (b). The $G(t)$ data are presented both without (thick circles) and with (dashed lines) electrostatic contributions.

With the increase of the electrostatic interaction strength, the charged monomers and counterions start to associate due to electrostatic attraction. A transition from ionic pairs or dipoles, to multiplets and linear chains of alternatively arranged ions and counterions, large ionic clusters and even percolated ionic networks is found with increasing ℓ_B. In the last case, there is a supramolecular double network structure constructed by the ionic network skeleton which cross links the polymer chains into percolated polymer network.

The dynamic and rheological behaviour of the ionomer systems, as measured by the mean squared displacements of charged monomers, the chain end-to-end vector and the stress relaxation functions, are retarded in comparison with their neutral counterparts with the increase of the electrostatic interaction strength. We show that the fluctuation-induced partner exchange processes both inside and between the ionic clusters facilitate the chain relaxation. Therefore even at high Bjerrum length ℓ_B (up to 40σ) when the large ionic aggregates including percolated networks are formed, the system can still relax to reach their terminal regime within reasonable simulation times.

Chapter 6

Conclusion and Future Work

6.1   Conclusions

We have shown that for single chain asymmetric in charge densities, but overall charge neutral, exhibit a plethora of behaviour for various electrostatic interaction strengths. In the absence of charge, the diblock chains with $N_- f_- = N_+ f_+$ would behave as neutral polymers of length $N = N_+ + N_-$. As the electrostatic interaction strength is increased, the chain conformation transition from folding to coil, then to weakly and finally strongly associating state [12]. An asymmetric increase in neutral chain segment lengths on the negatively charged block yields a swelling in the positively charged block at increasing electrostatic interaction strengths. It requires higher attraction energy to fold the negatively charged ions. As the electrostatic interaction strength increases above the entropic barrier, more negatively charged monomers are able to bind with the oppositely charged block. For small asymmetries this yields a folding of the two individual blocks into a globule, however chains with longer neutral segments on the negatively charged block cause a further extension of the positively charged block and looping of the neutral segments of the other block due to ionic binding, such that they

take a bottle brush conformation.

We study asymmetric diblock polyampholytes with $f_- = f_+$ but with a longer N_- We show that with increasing charge asymmetry the globule starts to elongate into cigar-like shapes. If the electrostatic interaction strength is high it can extend into into a helix/PE core structure with the longer block wrapping around the shorter one. Although infrequent, low symmetric chains at low ℓ_B are able to adopt the helical structure, see figure 3.42. The two oppositely charged blocks scramble together until the whole chain is about $N_{\mathrm{excess}} \approx 0.5$. A further increase in charge asymmetry leads to a PE tail sticking out carrying part of the excess charges. The chain conformation thus turns into a tadpole-like shape consisting of a net-charged cigar-like head and a polyelectrolyte tail. This conformational transition is qualitatively consistent with the theoretical predictions of Shusharina et al [13], however the theory didn't consider the elongation of the head the theory is developed for θ solvent and our results are relevant to a good solvent, and this difference needs to be taken into consideration when discussing the theory. Further theoretical work is still needed for describing our simulation results.

Bringing two asymmetric chains with a net valence together yields a general repulsion behaviour across multiple parameters. Using umbrella sampling we were able to show that symmetric chains are obviously favourable for the centre of masses to be close, however even slightly asymmetric chains presented a long range repulsion, albeit with an attractive core. This implies that asymmetric diblock polyampholytes do not want to aggregate into stable micelles. This is further evidenced in our analysis of multiple chains. Chains show an overall dislike for sending out polyelectrolyte arms from the head and favour instead helix/PE core. It is more favourable to form a helix/PE

139

core with ones own chain, and as such the chains eventually dissociate into effective net-charged polyelectrolytes. However, we observed surprisingly stable formations with the addition of just a single PE stabiliser, and three regimes were identified, a dense core, a helix/PE core layer, and polyelectrolyte arms. Although there are charge density fluctuation induced attraction, there is more charge density induced repulsion.

Molecular dynamics simulations have been performed to study the static and dynamic properties of unentangled ionomer systems consisting of either purely telechelic chains with charged end monomers or mixtures of half telechelic and half middle-charged chains. Two different chain lengths $N = 21$ and 41 have been studied, both are well below the entanglement length. The effect of electrostatic interactions is examined by varying the Bjerrum length ℓ_B over a wide range from 0 to 40σ.

With the increase of the electrostatic interaction strength, the charged monomers and counterions start to associate due to electrostatic attraction. A transition from ionic pairs or dipoles, to multiplets and linear chains of alternatively arranged ions and counterions, large ionic clusters and even percolated ionic networks is found with increasing ℓ_B. In the last case, there is a supramolecular double network structure constructed by the ionic network skeleton which cross links the polymer chains into percolated polymer network.

The dynamic and rheological behaviour of the ionomer systems, as measured by the mean squared displacements of charged monomers, the chain end-to-end vector and the stress relaxation functions, are retarded in comparison with their neutral counterparts with the increase of the electrostatic interaction strength. We show that the fluctuation-induced partner exchange processes both inside and between the ionic clusters facilitate the chain relaxation. Therefore even at high Bjerrum length ℓ_B (up to 40σ) when the large ionic aggregates including percolated networks are formed, the system can still

relax to reach their terminal regime within reasonable simulation times.

6.2 Future Work

6.2.1 Single Chain

Zero net charge

To study these chains in greater detail, one could lower the valence of the higher density block so that the positively and negatively charged electrostatic blobs are of the same size, to see if this would allow the chains to behave more symmetrically, and universally collapse into a globule.

Net charge

One could run chains of length $N = 800$, $N = 1600$ and $N = 3200$, and have the negatively charged block length $N_- = 1.5N_+$, thus $N_{\text{excess}} \approx 0.5$. The difficulty is whether these chain lengths are feasible computationally. Setting the number of monomers in a blob $g_e = 32$, and charge fraction $f_- = 1/8$, and $\ell_B = 1.0$, would yield an electrostatic blob containing approximately 4 charges. Thus, the self repulsion should be less effective on the behaviour of the electrostatic blob, and the behaviour in a blob more likely to be unperturbed. This would yield a total of 25, 50 and 100 total electrostatic blobs for the respective systems, and these blobs will be sparsely charged. This behaviour may yield behaviour predicted in the literature, in which case diblock polyampholytes with a high density of charges with have a tendency for helical behaviour whereas chains with significant distance between charges will behave as predicted. On the contrary, the results of the longer chain agree with these results, then it is likely that diblock polyampholytes globally favour helices for a wide range of parameters, and attention

should be taken when attempting to construct diblock polyampholyte micelles. One could also like to run MD simulations of polyelectrolytes in poor solvents and see how they compare. Also, I'd like to simulate an alternating charged head, with additional charges sent out in the form of a polyelectrolyte tail. I'd be interested to see if the non tethering of the lower number of charges would allow for increased globular behaviour, perhaps even tadpole. There is no need for the alternating block to snake along the longer block, and helix/PE core behaviour is unlikely due to the similar charges. I believe these chains will collapse into tadpoles, and perhaps be more likely to form stable micelles. I believe it is the nature of diblock polyampholytes to form helices due to the self repulsion.

With some fine tuning of the Umbrella sampling code, one could change the reaction coordinate to bending angle and study bending the positive block. The results should yield it is favourable in the symmetric case to bend the block, but for increasing asymmetries and higher electrostatic interaction strengths a favouring for stretching.

6.2.2 Multiple Chains

2 Chain

The next step would be to get the broad spectrum of behaviour using umbrella sampling across the parameter space. We would then be able to identify the transition from fully attractive, to closely attractive with long range repulsion, to fully repulsive. I'd also like to perform umbrella sampling simulations of the chains with the PE stabiliser, to identify the transition asymmetry that will cause the polyelectrolyte to associate with a single chain.

142

I would also like to apply the analysis to two asymmetric chains with zero net charge. I expect the net neutral systems to transition from sedimentation in the low asymmetric and low ℓ_B case, to soluble in the high electrostatic interaction strength, high asymmetry systems due to the bottle brushing.

Multiple Chains

One could study much longer chains, with longer neutral segments, to understand if the charge density is effecting the conformational behaviour.

In a dense box $\rho = 10^{-2}$ the highly asymmetric, multi-chain simulation, the chains appeared to form a potential percolated network, containing large, very strong bonds connected by less dense polyelectrolyte strands, see figure 6.1. Here, the monomers are colour coded by chain. Several chains can be observed leaving the simulation box and re-entering the aggregate from the relevant opposite side. This is likely to be a very strong, stable, sparse network. However, further study is required to comment on the behaviour more accurately.

6.2.3 Ionomer

We would study an additional system in which half the telechelic chains are positively charged whilst the others are negatively charged. This implies that a single chain is unable to associate with itself without the presence of additional attractive ions. Furthermore, each associative bond counts as an additional part of the network. Finally, the increased friction due to chain tethering should help stabilise the clustering more. I fully expect this to form a much more stable network, but without further discussion I am uncertain of the reality of these systems.
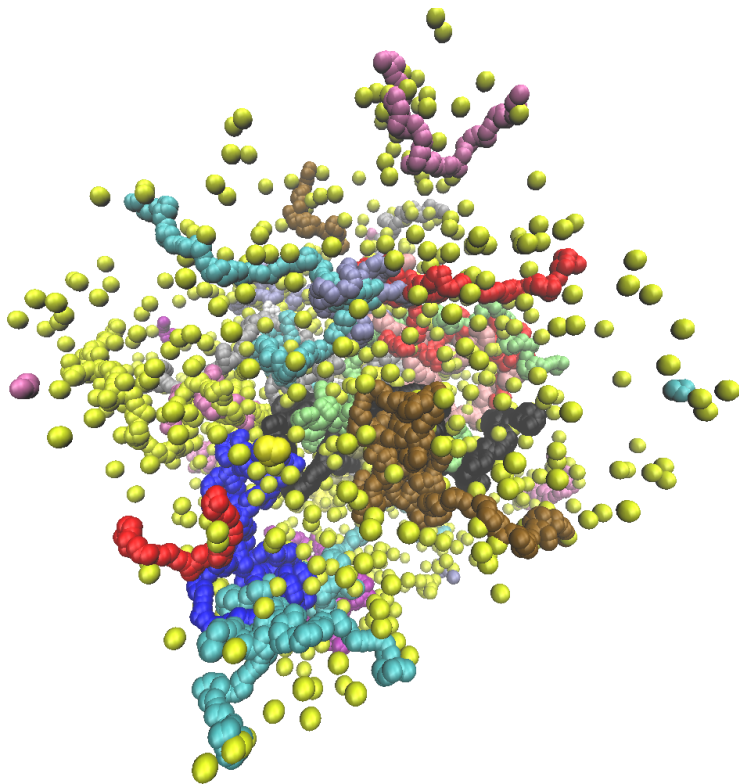
Figure 6.1: Pearl Network

I'd like to study entangled chains, as the distance between charges should be sufficient that cluster analysis is a lot more straightforward, as the ions should aggregate into smaller groups with greater distance. This will also yield a much more informative lifetime and cluster distribution profile.

To more accurately understand the behaviour, one would need to understand the cluster lifetime. How do the ions diffuse with the highest frequency? How often do large clusters break away and how long for? Is this the main way that bonds are changed? What is the life expectancy of the ion network? Does it exist solely as added friction for the end monomers but in reality provides no stability to the chain network?

Appendices

Appendix A

REMD with Bjerrum Length Replica Swaps

A.1 Implementation

The following is the replica exchange code. Special thanks goes to Pawel Stasiak.

```
//#ifdef MPI


/*
we attempt a swap between two non interacting replica simulations
Ecou is the Bjerrum Length independant Coulomb energy
th is all particle information
N is number of particles * size of a particle (position, velocity, acceleration,
number of bonds ...)
lA is the array of charge strengths (criteria for swap acceptance)
istep is iteration step
*/
```

```
int temperingSweep (double E, double *th, int N, double *lA, int istep)
{
static double *thbuf;
static int direction = -1;
const static int dM = 1;
static int rank = -1;
static int numtasks;
static double l;
if (rank == -1)
{
MPI_Comm_rank (MPI_COMM_WORLD, &rank);
MPI_Comm_size (MPI_COMM_WORLD, &numtasks);
thbuf = new double[ N + 2];
l = lA[rank]; // lA[rank] is replica specific charge strength
}
static MPI_Status status;

direction *= -1;
//if (direction > 0)
// we only want to swap with nearest neighbour
// (closest replica charge strength either side)
// but it is possible to swap with other replicas
//   dM = (dM) % 2 + 1;
int partner = ...
... ((rank / dM) % 2) ? (rank + dM * direction) : (rank - dM * direction);
```

```cpp
MPI_Barrier(MPI_COMM_WORLD);


// Should one need check if the replicas are swapping as expected
//std::cout<<"PT "<<rank<<" "<<direction<<" "<<dM<<" "<<partner<<std::endl;


if (partner >= 0 && partner <= numtasks - 1 )
{
const double r1 = sprng (); //random number
th[N] = E;
th[N + 1] = r1;
const int l = N + 2;
const int ID1 = partner;
const int ID2 = rank;


MPI_Sendrecv (th, l, MPI_DOUBLE, partner, ID1, thbuf, l, MPI_DOUBLE,
partner, ID2, MPI_COMM_WORLD, &status);


const double Epartner = thbuf[N];
const double r2 = thbuf[N + 1];


// Swap criteria
const double bE = -(l - lA[partner]) * (E - Epartner);
  // Probability that a swap will be accepted.
const double P = (bE > 0) ? exp (-bE) : 1.0;
const double r = (rank > partner) ? r1 : r2;
```

```cpp
if (r < P)

{

for (int ic = 0; ic < N; ic++)

th[ic] = thbuf[ic]; // swap the replicas

//global variable for tracking direction of swap.

if (direction == -1) acceptedTemperingCounter[0]++;

if (direction == 1) acceptedTemperingCounter[1]++;

overallAcceptance++; // increase if swap is accepted


swapFlag=1;

}

//global variable for tracking direction of attempted swap

if (direction == -1) allTemperingCounter[0]++;

if (direction == 1) allTemperingCounter[1]++;


overallAttempt++;

std::cout << " istep: " << istep << " accept: " << overallAcceptance << ...

... " out of " << overallAttempt << " on rank " << rank << ...

... " with BM length: " << Bjerrum << std::endl;

return 1;

}

return 0;

}

//#endif
```

The replica simulations are run in parallel, via mpicc. The array of charge strengths is a global variable. It is computationally expensive to swap the configurations, and as such we choose to attempt a swap every 1000 time steps, although this is arbitrary. As we are interested in the behaviour across multiple charge strengths, and to further save on computational time, we create replicas at integer Bjerrum lengths, and treat each replica as a system of interest. However, this is not necessary for the method to work, should the user be only interested in one temperature. We implement the following after positions and velocities have been updated in the md loop.

```
//-------------------------------------
//  ---------  Replica Sweep --------
//-------------------------------------
if (istep%iswap == 0)
{


E_cou = (energy.Coulomb_r + energy.Coulomb_k)/(Bjerrum*Temp);


temperingSweep(E_cou, (double*) part,...
... N_Particle*sizeof(Particle)/sizeof(double), TA,istep);
}
```

where *istep* is the current time step and *iswap* is the desired swapping frequency. *part* is all particle information.

A.2   Testing the REMD method

In addition to the information provided in section 2.2.3, most of the testing for the replica exchange method revolved around replicating the results of Wang and Rubin-

stein [12], see Figures A.1 (a) and 3.4. To perform this test, many simulations in parallel were used over a wide range of electrostatic interaction strengths. Results show good agreement with the literature. Figure A.1 (b) tracks the journey of a configuration over each replica charge strength it experiences. This is to highlight that in this short time frame, for this test system, the configuration explored each charge state.

Figure A.2 highlights the Coulomb energy jump associated with the configuration swap. This is not an issue when studying average behaviour, such as the Coulomb energy or the average end to end distances, as the new configuration is legitimate. One should note that if dynamical behaviour is to be analysed, this should only be performed between swaps.
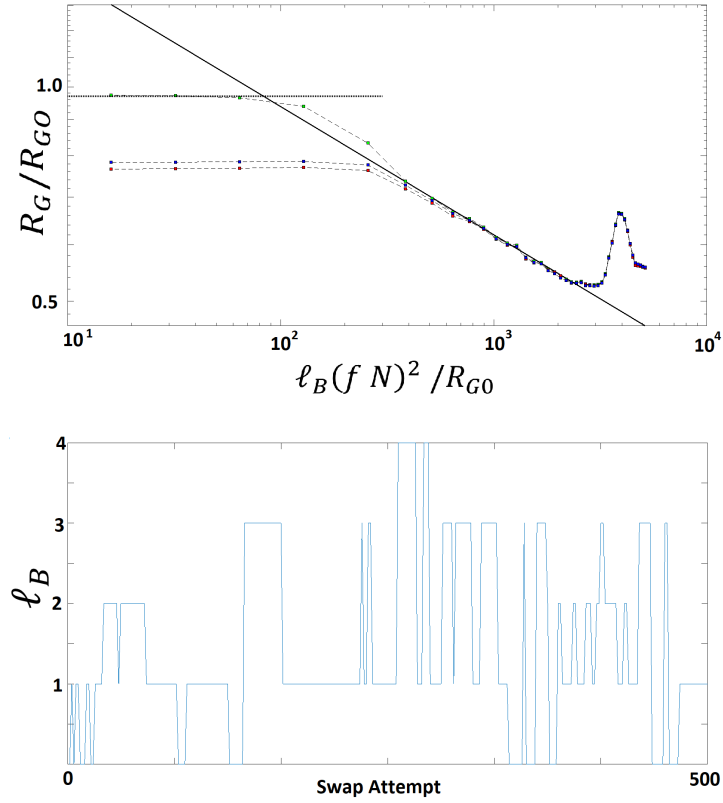
Figure A.1: (a) Testing the REMD method by comparing the results obtained by Wang and Rubinstein [12] (b) a set of 5 replicas of symmetric diblock polyampholyte chains with $N = 128$, $f = 1/2$, for $\ell_B/\sigma = \{0, 1, 2, 3, 4\}$, to track a single configuration's journey.
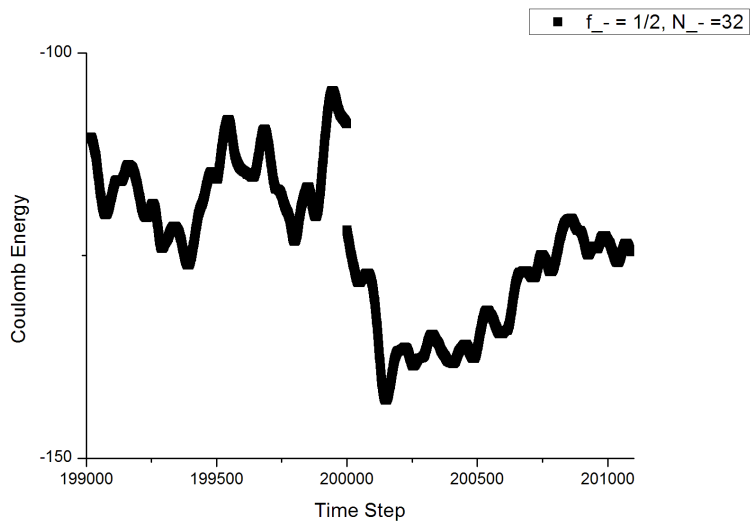
Figure A.2: System Coulomb energy for $\ell_B = 8\sigma$, $f_+ = f_- = 1/2$, $N_- = N_+$, $N = 32$, highlighting a swap.

Appendix B

Ionomers

B.1 Finite Size Effects

Simulations are underway to quantify the finite size effects of the Ionomer systems, and comparison can be made once the data is more substantial. We present the initial results here, but further simulation and analysis is required to make any concrete statements. Figure B.1 presents the stress relaxation function $G(t)$ and the end-to-end vector correlation functions for telechelic $N = 21$, $\ell_B = 20.0$, for number of chains $N_{\text{poly}} = 100$ and $N_{\text{poly}} = 200$, and in the former case, $N_{\text{poly}} = 400$. These many chain systems are incredibly computationally expensive; once more data is obtained further discussions can be made.
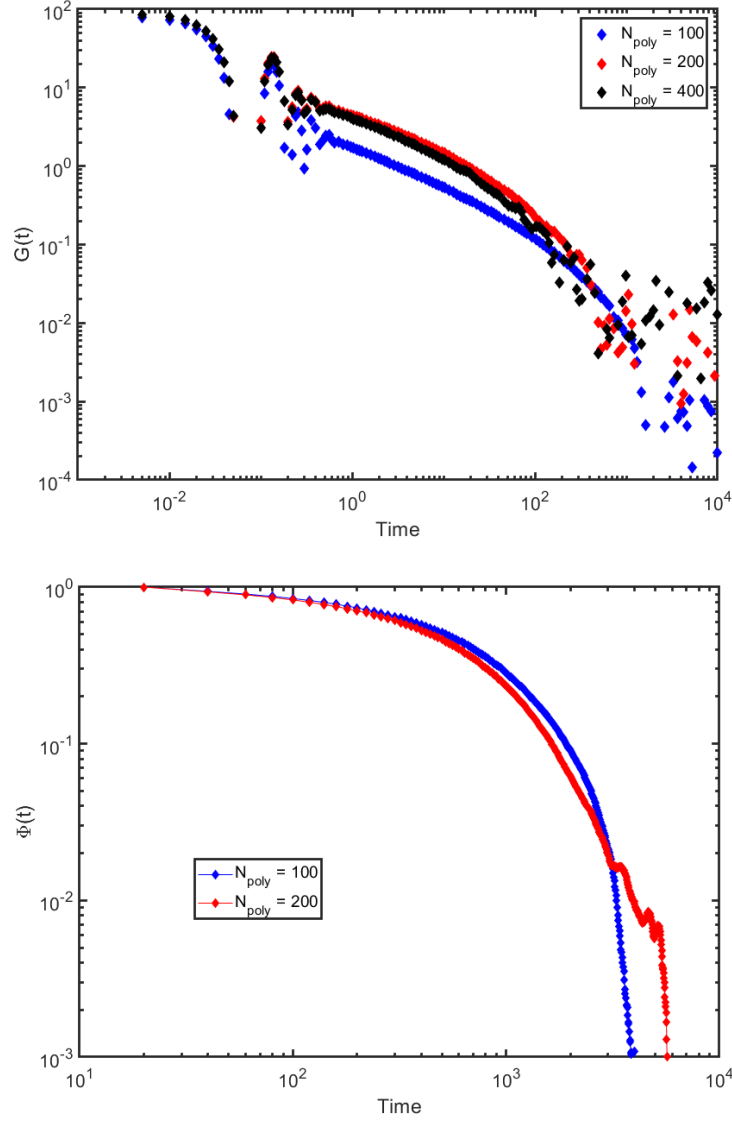
Figure B.1: (a) Stress Relaxation function $G(t)$ consisting of telechelic chains of length $N = 21$, Bjerrum length $\ell_B = 20.0$. (b) End-to-end vector correlation functions of the telechelic chains in the systems of purely telechelic chains with length $N = 21$, Bjerrum length $\ell_B = 20.0\sigma$. Data points are presented discretely to highlight the noise.
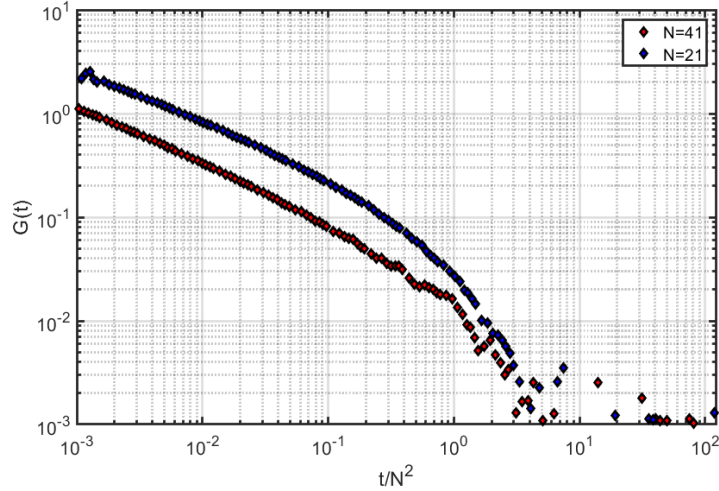
Figure B.2: $G(t)$ against t/N^2 plotted for both $N = 21$ and $N = 41$, $\ell_B = 20.0\sigma$. The higher effective viscosity is more prevalent in the $N = 21$ system, however comparing the two shows no considerable slow down in either.

B.2 Long Range Contributions to the Stress Tensor

Following the method described by the Espresso project [126], the long ranged, or k-space contributions to the stress tensor are given by

$$\sigma^{\text{rec}}_{(k,l)} = \frac{1}{4\pi\epsilon_0\epsilon_r}\frac{1}{2\pi V^2}\sum_{\mathbf{k}\neq\,\mathbf{0}}\frac{\exp\left(-pi^2\mathbf{k}^2/\beta^2\right)}{\mathbf{k}^2}\,|S(\mathbf{k})|^2\cdot\left(\delta_{k,l}-2\frac{1+\pi^2\mathbf{k}^2/\beta^2}{\mathbf{k}^2}\mathbf{k}_k\mathbf{k}_l\right)\ \ (\text{B.1})$$

here $S(\mathbf{k})$ is the Fourier transformed charge density. One would need to program this into their code, taking care to note the comments in [126].

B.3 Renormalised time

Figure B.2 presents $G(t)$ plotted against t/N^2. There appears to be no noticeable long term slow down in the long time relaxation, although a notable slow down for intermediate time.

Bibliography

[1] Jiahui Li, James A. Viveros, Michelle H. Wrue, and Mitchell Anthamatten. Shape-Memory Effects In Polymer Networks Containing Reversibly Associating Side-Groups. *Advanced Materials*, 19(19):2851+, Oct 5 2007.

[2] Stefano Burattini, Barnaby W. Greenland, Daniel Hermida Merino, Wengui Weng, Jonathan Seppala, Howard M. Colquhoun, Wayne Hayes, Michael E. Mackay, Ian W. Hamley, and Stuart J. Rowan. A Healable Supramolecular Polymer Blend Based On Aromatic Pi-Pi Stacking And Hydrogen-Bonding Interactions. *Journal Of The American Chemical Society*, 132(34):12051–12058, Sep 1 2010.

[3] Stefano Burattini, Barnaby W. Greenland, Wayne Hayes, Michael E. Mackay, Stuart J. Rowan, and Howard M. Colquhoun. A Supramolecular Polymer Based On Tweezer-Type Pi-Pi Stacking Interactions: Molecular Design For Healability And Enhanced Toughness. *Chemistry Of Materials*, 23(1):6–8, Jan 11 2011.

[4] Philippe Cordier, Francois Tournilhac, Corinne Soulie-Ziakovic, and Ludwik Leibler. Self-Healing And Thermoreversible Rubber From Supramolecular Assembly. *Nature*, 451(7181):977–980, Feb 21 2008.

[5] Yasufumi Umena, Keisuke Kawakami, Jian-Ren Shen, and Nobuo Kamiya. Crystal Structure Of Oxygen-Evolving Photosystem Ii At A Resolution Of 1.9 Angstrom. *Nature*, 473(7345):55–U65, May 5 2011.

[6] S Kitagawa, R Kitaura, and S Noro. Functional Porous Coordination Polymers. *Angewandte Chemie-International Edition*, 43(18):2334–2375, 2004.

[7] Rp Sijbesma, Fh Beijer, L Brunsveld, Bjb Folmer, Jhkk Hirschberg, Rfm Lange, Jkl Lowe, and Ew Meijer. Reversible Polymers Formed From Self-Complementary Monomers Using Quadruple Hydrogen Bonding. *Science*, 278(5343):1601–1604, Nov 28 1997.

[8] Wc Yount, Dm Loveless, and Sl Craig. Strong Means Slow: Dynamic Contributions To The Bulk Mechanical Properties Of Supramolecular Networks. *Angewandte Chemie-International Edition*, 44(18):2746–2748, 2005.

[9] Marc-Oliver M. Piepenbrock, Gareth O. Lloyd, Nigel Clarke, and Jonathan W. Steed. Metal- And Anion-Binding Supramolecular Gels. *Chemical Reviews*, 110(4):1960–2004, Apr 2010.

[10] Woongmo Sung, Sona Krem, and Doseok Kim. Binding Of Trivalent Ions On Fatty Acid Langmuir Monolayer: Fe3+ Versus La3+. *Journal Of Chemical Physics*, 149(16), Oct 28 2018.

[11] M Rubinstein and An Semenov. Dynamics Of Entangled Solutions Of Associating Polymers. *Macromolecules*, 34(4):1058–1068, Feb 13 2001.

[12] Zuowei Wang and Michael Rubinstein. Regimes Of Conformational Transitions Of A Diblock Polyampholyte. *Macromolecules*, 39(17):5897–5912, Aug 22 2006.

159

[13] Np Shusharina, Eb Zhulina, Av Dobrynin, and M Rubinstein. Scaling Theory Of Diblock Polyampholyte Solutions. *Macromolecules*, 38(21):8870–8881, Oct 18 2005.

[14] Av Dobrynin and M Rubinstein. Flory Theory Of A Polyampholyte Chain. *Journal De Physique Ii*, 5(5):677–695, May 1995.

[15] Av Dobrynin, Rh Colby, and M Rubinstein. Polyampholytes. *Journal Of Polymer Science Part B-Polymer Physics*, 42(19):3513–3538, Oct 1 2004.

[16] Ar Khokhlov and Pg Khalatur. Solution Properties Of Charged Hydrophobic/Hydrophilic Copolymers. *Current Opinion In Colloid & Interface Science*, 10(1-2):22–29, Aug 2005.

[17] Av Dobrynin, Rh Colby, and M Rubinstein. Scaling Theory Of Polyelectrolyte Solutions. *Macromolecules*, 28(6):1859–1871, Mar 13 1995.

[18] Av Dobrynin and M Rubinstein. Counterion Condensation And Phase Separation In Solutions Of Hydrophobic Polyelectrolytes. *Macromolecules*, 34(6):1964–1972, Mar 13 2001.

[19] Kevin M. Zurick and Matthew Bernards. Recent Biomedical Advances With Polyampholyte Polymers. *Journal Of Applied Polymer Science*, 131(6), Mar 15 2014.

[20] Jan-Michael Y. Carrillo and Andrey V. Dobrynin. Polyelectrolytes In Salt Solutions: Molecular Dynamics Simulations. *Macromolecules*, 44(14):5798–5816, Jul 26 2011.

[21] Quan Chen, Gregory J. Tudryn, and Ralph H. Colby. Ionomer Dynamics And The Sticky Rouse Model. *Journal Of Rheology*, 57(5):1441–1462, Sep 2013.

[22] R. A. Weiss and Wei-Ching Yu. Viscoelastic Behavior Of Very Lightly Sulfonated Polystyrene Ionomers. *Macromolecules*, 40(10):3640–3643, May 15 2007.

[23] Rh Colby, X Zheng, Mh Rafailovich, J Sokolov, Dg Peiffer, Sa Schwarz, Y Strzhemechny, and D Nguyen. Dynamics Of Lightly Sulfonated Polystyrene Ionomers. *Physical Review Letters*, 81(18):3876–3879, Nov 2 1998.

[24] Nk Tierney and Ra Register. Ion Hopping In Ethylene-Methacrylic Acid Ionomer Melts As Probed By Rheometry And Cation Diffusion Measurements. *Macromolecules*, 35(6):2358–2364, Mar 12 2002.

[25] Ma Winnik and A Yekta. Associative Polymers In Aqueous Solution. *Current Opinion In Colloid & Interface Science*, 2(4):424–436, Aug 1997.

[26] Nicholas W. Deluca and Yossef A. Elabd. Polymer Electrolyte Membranes For The Direct Methanol Fuel Cell: A Review. *Journal Of Polymer Science Part B-Polymer Physics*, 44(16):2201–2225, Aug 15 2006.

[27] R Langer. Drug Delivery And Targeting. *Nature*, 392(6679, S):5–10, Apr 30 1998.

[28] Uttam Kedar, Prasanna Phutane, Supriya Shidhaye, and Vilasrao Kadam. Advances In Polymeric Micelles For Drug Delivery And Tumor Targeting. *Nanomedicine-Nanotechnology Biology And Medicine*, 6(6):714–729, Dec 2010.

[29] Dipesh Amin, Alexei E. Likhtman, and Zuowei Wang. Dynamics In Supramolecular Polymer Networks Formed By Associating Telechelic Chains. *Macromolecules*, 49(19):7510–7524, Oct 11 2016.

[30] Ralph H. Colby. Structure And Linear Viscoelasticity Of Flexible Polymer Solutions: Comparison Of Polyelectrolyte And Neutral Polymer Solutions. *Rheologica*

Acta, 49(5, Si):425–442, May 2010. Gennes Discussion Conference On From Reputation To Glossy Materials - Gennes Pioneering Work In Rheology And Recent Developments, Chamonix, France, Feb 01-05, 2009.

[31] L Leibler, M Rubinstein, and Rh Colby. Dynamics Of Reversible Networks. *Macromolecules*, 24(16):4701–4707, Aug 5 1991.

[32] J Wittmer, A Johner, and Jf Joanny. Random And Alternating Polyampholytes. *Europhysics Letters*, 24(4):263–268, Nov 1 1993.

[33] Quan Chen, Zhijie Zhang, and Ralph H. Colby. Viscoelasticity Of Entangled Random Polystyrene Ionomers. *Journal Of Rheology*, 60(6):1031–1040, Nov-Dec 2016.

[34] Robert Brown. A Breif Account Of Microscopical Observations Made In The Months Of June, July And August 1827, On The Particles Contained In The Pollen Of Plants; And On The General Existence Of Active Molecules In Organic And Inorganic Bodies. 1828.

[35] M. Doi and S. F. Edwards. *The Theory Of Polymer Dynamics*. Oxford University Press, Usa, November 1986.

[36] M.P. Allen and D.J. Tildesley. Computer Simulation Of Liquids. Oxford: Clarendon Pr, 1987.

[37] Pg Degennes, P Pincus, Rm Velasco, and F Brochard. Remarks On Polyelectrolyte Conformation. *Journal De Physique*, 37(12):1461–1473, 1976.

[38] Michael Rubinstein and Ralph Colby. *Polymer Physics*. Oxford University Press, 2003.

[39] L. G. D. Hawke, M. Ahmadi, H. Goldansaz, and E. Van Ruymbeke. Viscoelastic Properties Of Linear Associating Poly(N-Butyl Acrylate) Chains. *Journal Of Rheology*, 60(2):297–310, Mar-Apr 2016.

[40] Alexei E. Likhtman, Sathish K. Sukumaran, and Jorge Ramirez. Linear Viscoelasticity From Molecular Dynamics Simulation Of Entangled Polymers. *Macromolecules*, 40(18):6748–6757, Sep 4 2007.

[41] Vy Borue and Iy Erukhimovich. A Statistical-Theory Of Globular Polyelectrolyte Complexes. *Macromolecules*, 23(15):3625–3632, Jul 23 1990.

[42] R Everaers, A Johner, and Jf Joanny. Polyampholytes: From Single Chains To Solutions. *Macromolecules*, 30(26):8478–8498, Dec 29 1997.

[43] Y Kantor and M Kardar. Excess Charge In Polyampholytes. *Europhysics Letters*, 27(9):643–648, Sep 20 1994.

[44] Jl Barrat and Jf Joanny. Theory Of Polyelectrolyte Solutions. In *Advances In Chemical Physics, Vol Xciv*, volume 94 of *Advances In Chemical Physics*, pages 1–66. John Wiley & Sons Inc, 605 3rd Ave, New York, Ny 10016, 1996.

[45] T Odijk. Possible Scaling Relations For Semidilute Polyelectrolyte Solutions. *Macromolecules*, 12(4):688–693, 1979.

[46] J Skolnick and M Fixman. Electrostatic Persistence Length Of A Wormlike Polyelectrolyte. *Macromolecules*, 10(5):944–948, 1977.

[47] M Castelnovo and Jf Joanny. Phase Diagram Of Diblock Polyampholyte Solutions. *Macromolecules*, 35(11):4531–4538, May 21 2002.

[48] Jb Imbert, Jm Victor, N Tsunekawa, and Y Hiwatari. Conformational Transitions Of A Diblock Polyampholyte In 2 And 3 Dimensions. *Physics Letters A*, 258(2-3):92–98, Jul 19 1999.

[49] M Rubinstein, Rh Colby, and Av Dobrynin. Dynamics Of Semidilute Polyelectrolyte Solutions. *Physical Review Letters*, 73(20):2776–2779, Nov 14 1994.

[50] Av Dobrynin, A Deshkovski, and M Rubinstein. Adsorption Of Polyelectrolytes At Oppositely Charged Surfaces. *Macromolecules*, 34(10):3421–3436, May 8 2001.

[51] Andrey V. Dobrynin. Theory And Simulations Of Charged Polymers: From Solution Properties To Polymeric Nanomaterials. *Current Opinion In Colloid & Interface Science*, 13(6):376–388, Dec 2008.

[52] Av Dobrynin and M Rubinstein. Theory Of Polyelectrolytes In Solutions And At Surfaces. *Progress In Polymer Science*, 30(11):1049–1118, Nov 2005.

[53] Y Kantor, H Li, and M Kardar. Conformations Of Polyampholytes. *Physical Review Letters*, 69(1):61–64, Jul 6 1992.

[54] Gs Manning. Molecular Theory Of Polyelectrolyte Solutions With Applications To Electrostatic Properties Of Polynucleotides. *Quarterly Reviews Of Biophysics*, 11(2):179–246, 1978.

[55] Andrey V. Dobrynin. Effect Of Counterion Condensation On Rigidity Of Semi-flexible Polyelectrolytes. *Macromolecules*, 39(26):9519–9527, Dec 26 2006.

[56] M Deserno, C Holm, and S May. Fraction Of Condensed Counterions Around A Charged Rod: Comparison Of Poisson-Boltzmann Theory And Computer Simulations. *Macromolecules*, 33(1):199–206, Jan 11 2000.

[57] A Katchalsky. Polyelectrolytes. *Pure And Applied Chemistry*, 26(3):327–374, 1971.

[58] R Fuoss, A Katchalsky, and S Lifson. The Potential Of An Infinite Rod-Like Molecule And The Distribution Of The Counterions. *Chemistry*, 37( ):579–589 , Sep 1951.

[59] Gs Manning and J Ray. Counterion Condensation Revisited. *Journal Of Biomolecular Structure & Dynamics*, 16(2):461–476, Oct 1998.

[60] L Belloni, M Drifford, and P Turq. Counterion Diffusion In Poly-Electrolyte Solutions. *Chemical Physics*, 83(1-2):147–154, 1984.

[61] Lei Liu and Changbong Hyeon. From Octopus To Dendrite-Semiflexible Polyelectrolyte Brush Condensates In Trivalent Counterion Solution. *Journal Of Chemical Physics*, 149(16), Oct 28 2018.

[62] Julian Michalowsky, Johannes Zeman, Christian Holm, and Jens Smiatek. A Polarizable Martini Model For Monovalent Ions In Aqueous Solution. *Journal Of Chemical Physics*, 149(16), Oct 28 2018.

[63] Sj Marrink, Ah De Vries, and Ae Mark. Coarse Grained Model For Semiquantitative Lipid Simulations. *Journal Of Physical Chemistry B*, 108(2):750–760, Jan 15 2004.

[64] Siewert J. Marrink, H. Jelger Risselada, Serge Yefimov, D. Peter Tieleman, and Alex H. De Vries. The Martini Force Field: Coarse Grained Model For Biomolecular Simulations. *Journal Of Physical Chemistry B*, 111(27):7812–7824, Jul 12 2007.

[65] Katie A. Black, Dimitrios Priftis, Sarah L. Perry, Jeremy Yip, William Y. Byun, and Matthew Tirrell. Protein Encapsulation Via Polypeptide Complex Coacervation. *Acs Macro Letters*, 3(10):1088–1091, Oct 2014.

[66] G Decher. Fuzzy Nanoassemblies: Toward Layered Polymeric Multicomposites. *Science*, 277(5330):1232–1237, Aug 29 1997.

[67] Pengfei Zhang, Nayef M. Alsaifi, Jianzhong Wu, and Zhen-Gang Wang. Polyelectrolyte Complex Coacervation: Effects Of Concentration Asymmetry. *Journal Of Chemical Physics*, 149(16), Oct 28 2018.

[68] Jasper Van Der Gucht, Evan Spruijt, Marc Lemmers, and Martien A. Cohen Stuart. Polyelectrolyte Complexes: Bulk Phases And Colloidal Systems. *Journal Of Colloid And Interface Science*, 361(2):407–422, Sep 15 2011.

[69] Lu Li, Samanvaya Srivastava, Marat Andreev, Amanda B. Marciel, Juan J. De Pablo, and Matthew V. Tirrell. Phase Behavior And Salt Partitioning In Polyelectrolyte Complex Coacervates. *Macromolecules*, 51(8):2988–2995, Apr 24 2018.

[70] K Kremer and Gs Grest. Dynamics Of Entangled Linear Polymer Melts - A Molecular-Dynamics Simulation. *Journal Of Chemical Physics*, 92(8):5057–5086, Apr 15 1990.

[71] Y Sugita and Y Okamoto. Replica-Exchange Molecular Dynamics Method For Protein Folding. *Chemical Physics Letters*, 314(1-2):141–151, Nov 26 1999.

[72] G Stolovitzky and Bj Berne. Catalytic Tempering: A Method For Sampling Rough Energy Landscapes By Monte Carlo. *Proceedings Of The National*

Academy Of Sciences Of The United States Of America, 97(21):11164–11169, Oct 10 2000.

[73] E Marinari and G Parisi. Simulated Tempering - A New Monte-Carlo Scheme. *Europhysics Letters*, 19(6):451–458, Jul 15 1992.

[74] Ba Berg and T Neuhaus. Multicanonical Algorithms For 1st Order Phase-Transitions. *Physics Letters B*, 267(2):249–253, Sep 12 1991.

[75] Y Sugita and Y Okamoto. Replica-Exchange Multicanonical Algorithm And Multicanonical Replica-Exchange Method For Simulating Systems With Rough Energy Landscape. *Chemical Physics Letters*, 329(3-4):261–270, Oct 20 2000.

[76] G Besold, J Risbo, and Og Mouritsen. Efficient Monte Carlo Sampling By Direct Flattening Of Free Energy Barriers. *Computational Materials Science*, 15(3):311–340, Aug 1999.

[77] Dj Earl and Mw Deem. Parallel Tempering: Theory, Applications, And New Perspectives. *Physical Chemistry Chemical Physics*, 7(23):3910–3916, 2005.

[78] Rh Swendsen and Js Wang. Replica Monte-Carlo Simulation Of Spin-Glasses. *Physical Review Letters*, 57(21):2607–2609, Nov 24 1986.

[79] CJ Geyer. Markov-Chain Monte-Carlo Maximum-Likelihood. In Keramidas, EM, editor, *Computing Science and Statistics*, pages 156–163. Interface Foundation North America, 1991.

[80] Uhe Hansmann. Parallel Tempering Algorithm For Conformational Studies Of Biological Molecules. *Chemical Physics Letters*, 281(1-3):140–150, Dec 19 1997.

[81] H Fukunishi, O Watanabe, and S Takada. On The Hamiltonian Replica Exchange Method For Efficient Sampling Of Biomolecular Systems: Application To Protein

Structure Prediction. *Journal Of Chemical Physics*, 116(20):9058–9067, May 22 2002.

[82] Hugh Nymeyer. How Efficient Is Replica Exchange Molecular Dynamics? An Analytic Approach. *Journal Of Chemical Theory And Computation*, 4(4):626–636, Apr 2008.

[83] Da Kofke. On The Acceptance Probability Of Replica-Exchange Monte Carlo Trials (Vol 117, Pg 6911, 2002). *Journal Of Chemical Physics*, 120(22):10852, Jun 8 2004.

[84] N Rathore, M Chopra, and Jj De Pablo. Optimal Allocation Of Replicas In Parallel Tempering Simulations. *Journal Of Chemical Physics*, 122(2), Jan 8 2005.

[85] Motoshi Kamiya and Yuji Sugita. Flexible Selection Of The Solute Region In Replica Exchange With Solute Tempering: Application To Protein-Folding Simulations. *Journal Of Chemical Physics*, 149(7), Aug 21 2018.

[86] Lingle Wang and B. J. Berne. Efficient Sampling Of Puckering States Of Monosaccharides Through Replica Exchange With Solute Tempering And Bond Softening. *Journal Of Chemical Physics*, 149(7), Aug 21 2018.

[87] Alan Hicks and Huan-Xiang Zhou. Temperature-Induced Collapse Of A Disordered Peptide Observed By Three Sampling Methods In Molecular Dynamics Simulations. *Journal Of Chemical Physics*, 149(7), Aug 21 2018.

[88] P Liu, B Kim, Ra Friesner, and Bj Berne. Replica Exchange With Solute Tempering: A Method For Sampling Biological Systems In Explicit Water. *Proceed-*

ings Of The National Academy Of Sciences Of The United States Of America, 102(39):13749–13754, Sep 27 2005.

[89] Lingle Wang, Richard A. Friesner, and B. J. Berne. Replica Exchange With Solute Scaling: A More Efficient Version Of Replica Exchange With Solute Tempering (Rest2). *Journal Of Physical Chemistry B*, 115(30):9431–9438, Aug 4 2011.

[90] M Deserno and C Holm. How To Mesh Up Ewald Sums. I. A Theoretical And Numerical Comparison Of Various Particle Mesh Routines. *Journal Of Chemical Physics*, 109(18):7678–7693, Nov 8 1998.

[91] T Darden, D York, and L Pedersen. Particle Mesh Ewald - An N.Log(N) Method For Ewald Sums In Large Systems. *Journal Of Chemical Physics*, 98(12):10089–10092, Jun 15 1993.

[92] U Essmann, L Perera, Ml Berkowitz, T Darden, H Lee, and Lg Pedersen. A Smooth Particle Mesh Ewald Method. *Journal Of Chemical Physics*, 103(19):8577–8593, Nov 15 1995.

[93] R. W. Hockney and J. W. Eastwood. *Computer Simulation Using Particles*. 1988.

[94] Johannes Kaestner. Umbrella Sampling. *Wiley Interdisciplinary Reviews-Computational Molecular Science*, 1(6):932–942, Nov-Dec 2011.

[95] Gm Torrie and Jp Valleau. Non-Physical Sampling Distributions In Monte-Carlo Free-Energy Estimation - Umbrella Sampling. *Journal Of Computational Physics*, 23(2):187–199, 1977.

[96] Im Withers, Av Dobrynin, Ml Berkowitz, and M Rubinstein. Monte Carlo Simulation Of Homopolymer Chains. I. Second Virial Coefficient. *Journal Of Chemical Physics*, 118(10):4721–4732, Mar 8 2003.

[97] S Kumar, D Bouzida, Rh Swendsen, Pa Kollman, and Jm Rosenberg. The Weighted Histogram Analysis Method For Free-Energy Calculations On Biomolecules .1. The Method. *Journal Of Computational Chemistry*, 13(8):1011–1021, Oct 1992.

[98] Handan Arkin and Wolfhard Janke. Gyration Tensor Based Analysis Of The Shapes Of Polymer Chains In An Attractive Spherical Cage. *Journal Of Chemical Physics*, 138(5), Feb 7 2013.

[99] Jiri Vymetal and Jiri Vondrasek. Gyration- And Inertia-Tensor-Based Collective Coordinates For Metadynamics. Application On The Conformational Behavior Of Polyalanine Peptides And Trp-Cage Foldinge. *Journal Of Physical Chemistry A*, 115(41):11455–11465, Oct 20 2011.

[100] Frenkel D. and B. Smit. Undersanding Molecular Simulation. Academic Press, Inc., 2001.

[101] Jorge Ramirez, Sathish K. Sukumaran, Bart Vorselaars, and Alexei E. Likhtman. Efficient On The Fly Calculation Of Time Correlation Functions In Computer Simulations. *Journal Of Chemical Physics*, 133(15), Oct 21 2010.

[102] Ken Morishima, Xiang Li, Kazuyuki Oshima, Yoshiro Mitsukami, and Mitsuhiro Shibayama. Small-Angle Scattering Study Of Tetra-Poly(Acrylic Acid) Gels. *Journal Of Chemical Physics*, 149(16), Oct 28 2018.

[103] Ferenc Horkay, Peter J. Basser, Anne-Marie Hecht, and Erik Geissler. Ionic Effects In Semi-Dilute Biopolymer Solutions: A Small Angle Scattering Study. *Journal Of Chemical Physics*, 149(16), Oct 28 2018.

[104] Nir Kampf, Ellen J. Wachtel, Anton Zilman, Noah Ben-Shalom, and Jacob Klein. Anomalous Viscosity-Time Behavior Of Polysaccharide Dispersions. *Journal Of Chemical Physics*, 149(16), Oct 28 2018.

[105] T Goloub, A De Keizer, and Ma Cohen-Stuart. Association Behavior Of Ampholitic Diblock Copolymers (Vol 32, Pg 8441, 1999). *Macromolecules*, 33(20):7672, Oct 3 2000.

[106] Jf Gohy, S Creutz, M Garcia, B Mahltig, M Stamm, and R Jerome. Aggregates Formed By Amphoteric Diblock Copolymers In Water. *Macromolecules*, 33(17):6378–6387, Aug 22 2000.

[107] Shingo Ito, Ying Wang, Yuko Okamoto, and Stephan Irle. Quantum Chemical Replica-Exchange Umbrella Sampling Molecular Dynamics Simulation Reveal The Formation Mechanism Of Iron Phthalocyanine Iron And Phthalonitrile. *Journal Of Chemical Physics*, 149(7), Aug 21 2018.

[108] Evgeny B. Stukalin, Li-Heng Cai, N. Arun Kumar, Ludwik Leibler, and Michael Rubinstein. Self-healing of unentangled polymer networks with reversible bonds. *Macromolecules*, 46(18):7525–7541, 2013.

[109] R. L. Ameri David, Ming-Hsin Wei, David Liu, Brett F. Bathel, Jan P. Plog, Albert Ratner, and Julia A. Kornfield. Effects Of Pairwise, Self-Associating Functional Side Groups On Polymer Solubility, Solution Viscosity, And Mist Control. *Macromolecules*, 42(4):1380–1391, Feb 24 2009.

[110] Lld Freitas and R Stadler. Thermoplastic Elastomers By Hydrogen-Bonding .3. Interrelations Between Molecular-Parameters And Rheological Properties. *Macromolecules*, 20(10):2478–2485, Oct 1987.

[111] K Yamauchi, Jr Lizotte, and Te Long. Thermoreversible Poly(Alkyl Acrylates) Consisting Of Self-Complementary Multiple Hydrogen Bonding. *Macromolecules*, 36(4):1083–1088, Feb 25 2003.

[112] A Eisenberg, B Hird, and Rb Moore. A New Multiplet-Cluster Model For The Morphology Of Random Ionomers. *Macromolecules*, 23(18):4098–4107, Sep 3 1990.

[113] M Muller, A Dardin, U Seidel, V Balsamo, B Ivan, Hw Spiess, and R Stadler. Junction Dynamics In Telechelic Hydrogen Bonded Polyisobutylene Networks. *Macromolecules*, 29(7):2577–2583, Mar 25 1996.

[114] Mark Burnworth, Liming Tang, Justin R. Kumpfer, Andrew J. Duncan, Frederick L. Beyer, Gina L. Fiore, Stuart J. Rowan, and Christoph Weder. Optically Healable Supramolecular Polymers. *Nature*, 472(7343):334–U230, Apr 21 2011.

[115] Hiroshi Watanabe, Yumi Matsumiya, Yuichi Masubuchi, Osamu Urakawa, and Tadashi Inoue. Viscoelastic Relaxation of Rouse Chains undergoing Head-to-Head Association and Dissociation: Motional Coupling through Chemical Equilibrium. *Macromolecules*, 48(9):3014–3030, May 12 2015.

[116] Yumi Matsumiya, Hiroshi Watanabe, Osamu Urakawa, and Tadashi Inoue. Experimental Test For Viscoelastic Relaxation Of Polyisoprene Undergoing Monofunctional Head-To-Head Association And Dissociation. *Macromolecules*, 49(18):7088–7095, Sep 27 2016.

[117] Lg Baxandall and Sf Edwards. Deformation-Dependent Properties Of Polymer Networks Constructed By Addition Of Cross-Links Under Strain. *Macromolecules*, 21(6):1763–1772, Jun 1988.

172

[118] Lg Baxandall. Dynamics Of Reversibly Cross-Linked Chains. *Macromolecules*, 22(4):1982–1988, Apr 1989.

[119] Ms Green and Tobolsky Av. A New Approach To The Theory Of Relaxing Polymeric Media. *Macromolecules*, 14(2):80–92, Oct 13 1946.

[120] M Rubinstein and An Semenov. Thermoreversible Gelation In Solutions Of Associating Polymers. 2. Linear Dynamics. *Macromolecules*, 31(4):1386–1397, Feb 24 1998.

[121] Shilong Wu, Shuang Liu, Zhijie Zhang, and Quan Chen. Dynamics of telechelic ionomers with distribution of number of ionic stickers at chain ends. *Macromolecules*, 52(6):2265–2276, 2019.

[122] Zuowei Wang, Alexei E. Likhtman, and Ronald G. Larson. Segmental Dynamics In Entangled Linear Polymer Melts. *Macromolecules*, 45(8):3557–3570, Apr 24 2012.

[123] Quan Chen, Hanqing Masser, Huai-Suen Shiau, Siwei Liang, James Runt, Paul C. Painter, and Ralph H. Colby. Linear Viscoelasticity And Fourier Transform Infrared Spectroscopy Of Polyether-Ester-Sulfonate Copolymer Ionomers. *Macromolecules*, 47(11):3635–3644, Jun 10 2014.

[124] An Semenov and M Rubinstein. Dynamics Of Entangled Associating Polymers With Large Aggregates. *Macromolecules*, 35(12):4821–4837, Jun 4 2002.

[125] B. J. Gold, C. H. Hvelmann, N. Lhmann, N. K. Szkely, W. Pyckhout-Hintzen, A. Wischnewski, and D. Richter. Importance of compact random walks for the rheology of transient networks. *Acs Macro Letters*, 6(2):73–77, 2017.

[126] The ESPResSo project. http://espressomd.org/html/doc/analysis.html. 2019.